Pion Absorption on ^{3}He

by

Kevin Earl Wilson

B.S. in Physics
California Institute of Technology
June 1986

Submitted to the Department of Physics
in partial fulfillment of the requirements for the degree of

Doctor of Philosophy

at the

MASSACHUSETTS INSTITUTE OF TECHNOLOGY

February 1995

Signature of Author ....
Department of Physics
September 15, 1994

Certified by ....
Professor Robert P. Redwine
Thesis Supervisor

Accepted by ....
Professor George F. Koster
Chairman of the Graduate Committee

Pion Absorption on ^{3}He

by

Kevin Earl Wilson

Submitted to the Department of Physics
on September 15, 1994, in partial fulfillment of the
requirements for the degree of
Doctor of Philosophy

Abstract

Measurements of π^+ absorption on ^{3}He in the region of the $\Delta(1232)$ resonance have been made using the Large Acceptance Detector System (LADS) at the Paul Scherrer Institute in Villigen, Switzerland. The nearly 4π steradian solid angle coverage of this detector minimizes uncertainties associated with extrapolations over unmeasured regions of phase space. The total absorption cross section was measured to be 27.3 ± 0.8, 24.7 ± 0.7, and 10.0 ± 0.4 mb at $T_\pi = 118, 162$, and 239 MeV, respectively. This total is also divided into components in which only two or all three nucleons play a significant role in the process, with two-nucleon absorption contributing 21.3 ± 1.0, 17.4 ± 0.8, and 7.0 ± 0.6 mb and three-nucleon absorption contributing 6.0 ± 0.6, 7.2 ± 0.7, and 3.0 ± 0.5 mb to the total absorption cross section at $T_\pi = 118, 162$, and 239 MeV, respectively. These are the first direct measurements of the total and three-nucleon absorption cross sections. The differential distributions of the three-nucleon absorption cross sections are examined and significant deviations from isotropic three-nucleon phase space are observed. In particular, it is shown that at these energies three-nucleon absorption is enhanced over phase space by 25-35% in the region where the incident pion momentum lies close to the plane formed by the three outgoing protons in the center-of-mass system. In addition, the differential three-nucleon absorption distributions have some features similar to distributions produced by a classical two-step model in which the incident pion has an initial state interaction before undergoing two-nucleon absorption. The differential distributions are not similar to the distributions produced by a classical model consisting of two-nucleon absorption followed by a final state interaction.

Thesis Supervisor: Professor Robert P. Redwine
Title: Professor of Physics

Acknowledgements

The collaboration of scientists necessary to perform this experiment was large because of the experiment's ambitious scope, complexity, and expense. Many scientists were needed to design, build, and test the detector (LADS) and its associated software, and to set up the experiment and monitor the data acquisition. Therefore, the success of this experiment depended many people. Nor did the collaboration end after the data was collected, but continued as analysis tools, methods, and results were discussed and shared among the group.

Therefore, I will first thank the entire LADS collaboration, since they have labored for many years on this experiment on ^{3}He and others like it on other nuclei. Everyone in the collaboration (especially the numerous graduate students along with Quentin, Heinz, and Danek) spent many years working toward the goal of a clearer understanding of pion absorption, and a lot of difficult problems have been overcome through the hard work of many individuals. After a protracted struggle, I am confident that we have reached the "beginning of the end" and that the results the collaboration produces over the next few years will greatly increase the understanding of multi-nucleon pion absorption.

I would like specifically to thank the members of the LADS collaboration which are here at MIT: my advisor, Bob Redwine, as he has provided guidance and insight throughout my thesis project; Art and Nik, who helped out in many ways (checking results, writing code, producing figures, proofreading and more); Neven, who constantly challenged the "easy" interpretation of the data and was proven right more than a few times; and of course David, who did all of the above and who has sacrificed time from his own thesis project to speed the completion of mine.

I also owe much to my many friends who have made my years as a graduate student more enjoyable. Particularly my fellow physics graduate students, Jeff, Adam, Hojoon, Wilson, Marla, Kevin, and Sam, who understood my trials. Todd, friend, roommate, and co-conspirator, edited my thesis. He took on even the rough drafts, where verb and subject agreement could not be taken for granted. My wife and fellow physics graduate student Cathy, was my toughest editor, did my geometry for me (you will find her help documented in some of the code), and sometimes helped with various computer and physics problems I encountered. I am blessed to have a wife who can understand my work.

I want to thank my dad, mom, and sister, who always encouraged me, and gave me the confidence I needed to try things at which I might fail. While my graduation from MIT was sometimes in doubt, I was confident that they would continue to be proud of me.

Finally, I want to thank God, for "Blessed is he whose help is the God of Jacob, whose hope is in the Lord his God, the Maker of heaven and earth, the sea, and everything in them — the Lord, who remains faithful forever" [Psalm 146:5,6 (NIV)].

Contents

Chapter 1

Introduction

Since the advent of the meson facilities, pion-induced nuclear reactions have been the focus of much study. Steady progress has been made in our understanding of pion-nucleus reactions at energies around the Δ-resonance. However, some fundamental issues remain, particularly in our understanding of pion absorption on nuclei. Even some very general questions remain unanswered, including: how many nucleons are typically involved in pion absorption? and how are they involved? These simple questions have generated a substantial amount of interest and research for almost two decades. The answer to the former question has not been determined with any real quantitative precision, but a number of experiments suggest that between 20% to 50% of the cross section involves more than two nucleons. Any mechanism explaining how more than two nucleons are involved in pion absorption must also explain its size in comparison to two-nucleon absorption. The possibility that "multi-nucleon" absorption accounts for a large fraction of the absorption cross section has led to speculation about the need for "exotic" processes. Indeed, the idea that novel processes might be found via pion-nucleus interactions is an old motivation for the study of these reactions. This possibility was suggested by the nature of the pion probe; a pion is a boson which is intimately connected to the strong force, as explained in the next section, and these properties make it considerably different than the other common probes of the nucleus, *i.e.* electrons, protons, and γ's.

A number of universities and institutes decided to collaborate to search for answers to the two questions above with the hope of that their answers would determine whether "exotic processes" are needed to explain multi-nucleon pion absorption. They constructed the Large Acceptance Detector System (LADS) specifically to study multi-nucleon pion absorption in the Δ-resonance region [1]. This detector is uniquely able to study this reaction since it can measure multi-nucleon absorption without large extrapolations over unmeasured regions. These large, model-dependent extrapolations have been a problem with past experiments and have confused their interpretation.

This thesis uses the LADS detector to study π^+ absorption in ^{3}He, at incident pion energies of $T_\pi = 118$, 162, and 239 MeV. ^{3}He is the simplest nucleus in which absorption on more than two-nucleons can occur, and has the theoretical advantage that its ground state wavefunction is very well modeled. The emphasis of this work is not a search for novel processes, but is on precise, quantitative results that have little model dependence. The total absorption cross section in ^{3}He is measured more precisely than before and, for the first time, in an essentially model-independent manner. The percentage of two- and three- nucleon absorption is also measured more precisely and with much less model dependence than in any previous measurement. Finally, the mechanism responsible for the three-nucleon component of the cross section will be examined using kinematic variables that were inaccessible to other experiments because of the limitations of the experimental apparatus. This provides a basis for comparison to future calculations and allows us to determine whether the models used in the previous experiments to determine the size of the three-nucleon absorption cross sections in ^{3}He were justified. It is hoped that by comparison of these results to calculations of known and "exotic" processes, the nature of the three-nucleon absorption mechanism in ^{3}He can be determined.

1.1 General Background

The pion, together with its interaction with nucleons, has been the subject of study ever since Yukawa first postulated its existence [2]. Yukawa's great insight was that the force that held the nucleons together in the nucleus could be described by the exchange between the nucleons of a particle with a mass of approximately 130 MeV. After some initial confusion, which resulted from the unexpected discovery of another particle of approximately the same mass*, the existence of the pion was indeed confirmed [3]. Over the years much has been learned about the pion; some of this information is summarized in Table 1.1, while a more detailed list is given in reference [4].

Even with the discovery of a veritable zoo of other mesons, as the lightest meson the pion still plays a special role. While it is not possible, as Yukawa had hoped, to describe the nucleon-nucleon interaction completely in terms of the exchange of pions, in the modern models of the

---

*The muon, which has a mass of 105.67 MeV was initially mistaken as Yukawa's postulated particle.

Pion Properties					
Charge	J^p	T	Mass	Mean Life	Decay Mode
$\pi^{\pm}$	0^-	1	139.567 MeV	2.6×10^{-8}s	$\mu\nu_\mu$ 99.9%
π^0	0^-	1	134.974 MeV	8.4×10^{-17}s	2γ 98.8%

Table 1.1: Important particle properties of the pion.

potential available today (Bonn, Paris) [5, 6] the long-range part of the potential is described as the exchange of one pion, and the medium-range part as multi-pion exchange. Only for the short-range part has it been found to be necessary to include the exchange of other mesons or to incorporate quark/gluon degrees of freedom in order to describe the observed nuclear properties adequately. Even for a single nucleon, chiral bag models [7] describe the nucleon as a quark core surrounded by a cloud of virtual pions which are constantly being emitted and absorbed. In this model it is the pion cloud which gives the nucleon its large size.

We see that the emission and absorption of virtual pions is essential to our understanding of nucleons and the nucleus and it is therefore natural to study the absorption of real pions too.

The process of pion absorption has several unique features which make it an interesting reaction and different from reactions produced using other nuclear probes. First, since the mass of the pion is converted into energy, pion absorption deposits a very large amount of energy in the system without a correspondingly large momentum transfer. This feature opens up a kinematic region that is difficult to access in other ways. Second, the pion is a probe having isospin $T = 1$ which allows the study of isospin degrees of freedom. Third, absorption of real pions involves at least two nucleons (absorption on a single nucleon in the nucleus is strongly suppressed by energy and momentum conservation), so nucleon correlations within the nucleus are likely to play a role.

1.2 Pion Reactions in the Δ-Resonance Region

Pion absorption's dominant feature for energies below $T_\pi = 1$ GeV is the strong resonance of the cross section near the Δ mass. The Δ is an excited state of the nucleon with $J = \frac{3}{2}$, $T = \frac{3}{2}$ and a mass of 1232 MeV; it has a very short lifetime of 0.59×10^{-23} s, which is equivalent to a FWHM $\approx$ 120 MeV. Its preferred mode of decay outside of the nuclear medium is $\Delta \rightarrow \pi N$

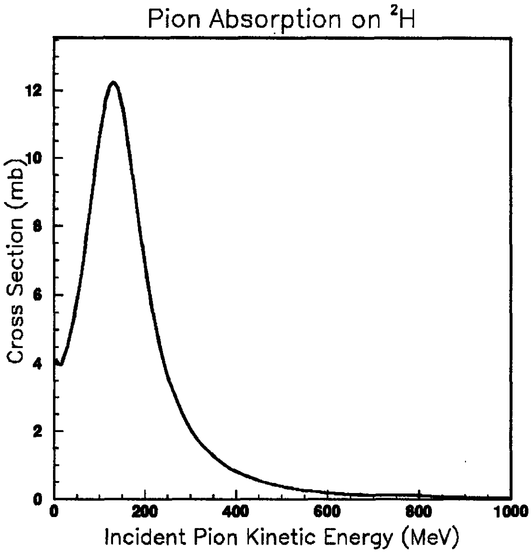

Figure 1-1: The curve is the parameterization of the world's data for the reaction ^{2}H(π^+, pp) from reference [8]. The strong coupling of the πN to the Δ at T_π = 130 MeV produces the resonance behavior in the absorption cross section.

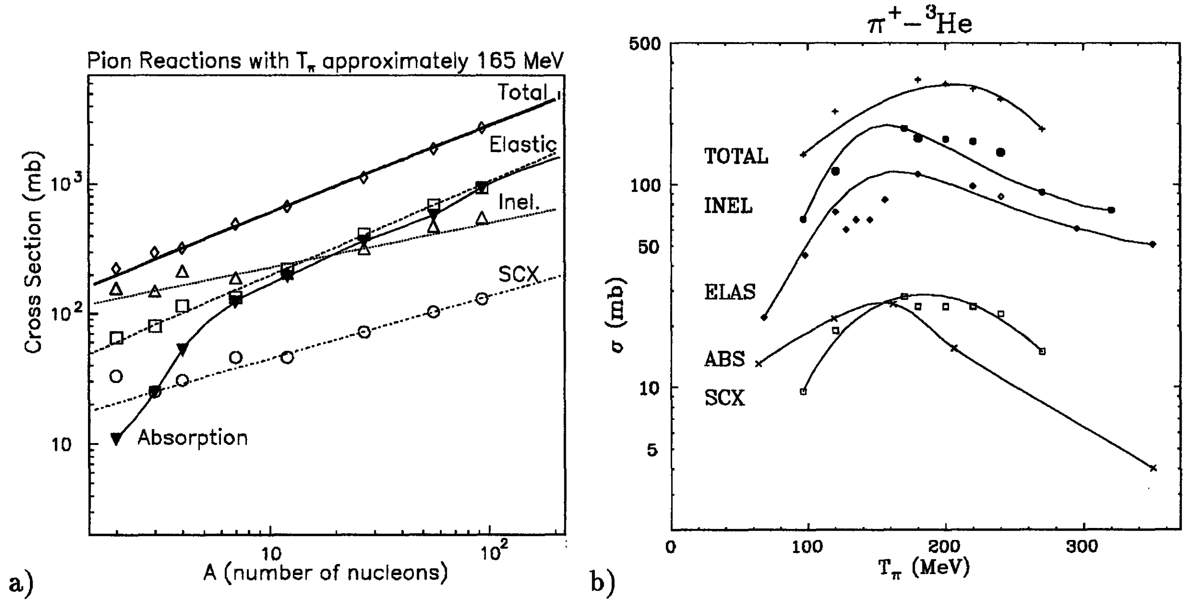

Figure 1-2: For both plots, error bars have been omitted and lines are only to guide the eye. Figure a) shows the π^+ cross sections as a function of A at the Δ-resonance. The data is from references [8, 9, 10, 11, 12, 13, 14]. Figure b) shows the π^+ cross sections on ^{3}He as a function of energy. Adapted from reference [13].

(99.5% branching ratio). Within the nuclear medium, de-excitation of the Δ is possible and often occurs through the interaction of the Δ with a nucleon. The πN couples strongly to the Δ, causing a large increase in the pion cross section in the region of resonance.

While this thesis will concentrate exclusively on pion absorption, it is important to keep in mind that it is only one of many possible reactions. In the energies around the Δ-resonance it is possible for a pion interacting with a nucleus not only to be absorbed, but also to do any of the following:

1) Scatter elastically. In this reaction, the pion scatters elastically from the nucleus as a whole.
2) Scatter quasi-elastically. In this reaction, the pion scatters elastically from one or more nucleons in the nucleus. It is characterized by a final state consisting of a pion, one or more nucleons, and a residual nucleus.
3) Undergo charge exchange. In this reaction, the pion interacts with a nucleon and the charge of the nucleon and pion are changed. The final state is characterized by a pion with a different charge than that of the incident pion. This process is typically smaller than either elastic or quasi-elastic scattering.

Figure 1-2 a) shows the relative sizes of these cross sections compared to the absorption cross section as a function of A for $T_\pi \approx 165$ MeV. All of these reactions are interesting in themselves and have in the past enriched our understanding of nuclear physics, and while theoretically they are closely linked to each other, the final states are different enough to demand different experimental detectors, setups, and techniques.

1.3 Pion Absorption on Two- and Three-Nucleons

As pion absorption on a free nucleon is forbidden by energy and momentum conservation, a composite nucleus is needed for its study. The simplest nucleus is deuterium, which has quantum numbers $J = 1$ and $T = 0$. Much effort has gone into the study of pion absorption on deuterium, and indeed much has been learned about two-nucleon absorption from this reaction. By now the cross section is so well measured that it is commonly used for the normalization of experiments on other nuclei. Ritchie [8] has parameterized the $^2\mathrm{H}(\pi^+, pp)$ cross section below 1 GeV and produced a best fit to the world's data which greatly facilitates this normalization procedure. The present experimental endeavor uses it both as a check of our absolute normalization and as a model for $T = 0$ two-nucleon absorption.

A model for absorption on deuteron-like pairs of nucleons is of particular importance since absorption on pairs with these quantum numbers is especially favored in nuclei. Several experiments [15, 16] have demonstrated that absorption on $T = 1$ pairs in the nucleus is a factor of about 20 less likely than absorption on $T = 0$ pairs in the Δ-resonance region. Ohta, Thies, and Lee have calculated [17] the probability of absorption in the nucleus on *pn* pairs with different ground state configurations. They confirm the privileged role that deuteron-like $^3S_1(T = 0)$ pairs play in pion absorption and provide a theoretical foundation for the use of the quasi-deuteron model. The quasi-deuteron model is the basis for a phenomenological model that experimentalists often use to describe two-nucleon absorption (2NA) in nuclei with $A \geq 3$. Pion absorption on *pn* pairs has the distinct kinematic signature of two highly energetic protons which are emitted back-to-back in the π-d center of mass frame. In nuclei heavier than deuterium, this signature remains relatively distinct, although it is broadened somewhat by the Fermi momenta of the nucleons. In the quasi-deuteron model (QDM) 2NA is treated as absorption on a deuteron which has a Fermi momentum within the nucleus. After correction for the Fermi momenta, $d\sigma_{2NA}/d\Omega$ for heavy nuclei has the same approximate shape as for deuterium.

Quasi-deuteron absorption, with minor corrections for other processes, was expected by many to explain pion absorption on heavy nuclei. However, early work by McKeown *et al.* [18] raised the possibility that three, four, or even five nucleons might often be involved in the pion absorption process. Though there has been significant progress in the last two decades, this question is quantitatively still unanswered and remains a source of controversy. For example, later experiments on heavy nuclei [19, 20, 21] found a significant amount of strength in the absorption cross section that does not seem to be explainable by two-nucleon absorption, even after attempts to correct the 2NA cross section by the expected contributions from other known processes. Burger *et al.* found that in ^{58}Ni at $T_\pi = 160$ MeV, less than 50% of the absorption cross section seems to be due to a 2NA mechanism [19]. Similarly, Hyman *et al.* found in ^{16}O at $T_\pi = 165$ MeV that only 50% of the absorption cross section was explainable by a 2NA mechanism [21]. Thus, there has been much speculation about the need for a "multi-nucleon absorption mechanism" to explain the origin of the rest of the absorption cross section.

In pion absorption, because of the importance of two-nucleon absorption, "multi-nucleon" has come to mean three or more nucleons. However, there is no standard definition of "multi-nucleon absorption mechanism" in the field. Some investigators reserve this term for coherent

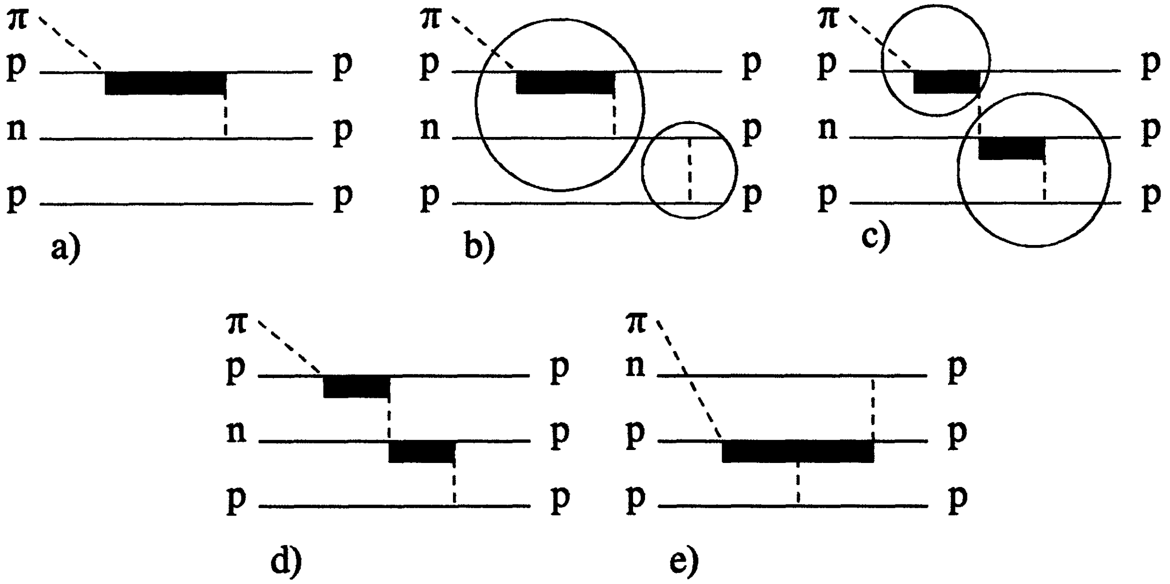

Figure 1-3: Diagrams of various pion absorption mechanisms. The dashed lines indicate pions, thin solid lines nucleons, and wide solid lines represent nucleons in excited states. A 2NA mechanism is drawn in a). Diagram b) is FSI, and the circles indicate that the process is incoherent. Diagram c) is ISI, again with the circles indicating incoherence. Diagrams d) and e) are "true," or coherent, three-nucleon absorption where the sums of the amplitudes are squared.

absorption processes which cannot be separated into sequential steps involving 2NA and other known processes. In this thesis we will follow a simpler convention and define multi-nucleon mechanisms as absorption processes in which more than two nucleons are involved. Thus "three-nucleon absorption" (3NA), will refer to a process in which three nucleons had some active role and none of the three was only a "spectator."

In Figure 1-3 a), 2NA is shown in ^{3}He. The third nucleon acts simply as a spectator, and its final state momentum is expected to be the same as its momentum in the initial state. Throughout Figure 1-3, the presence or absence of other spectator nucleons does not affect the qualitative description of the processes, which can therefore be easily generalized to $A > 3$. For example, in Figure 1-3 a) the spectator proton could be replaced by $A - 2$ nucleons.

Figure 1-3 b) shows a 3NA process that is closely related to the 2NA process. It is commonly referred to as a final-state interaction (FSI) process. After two of the nucleons absorb the pion, one of the nucleons scatters off a spectator nucleon. The process is often further categorized by whether there was a significant momentum transfer between the nucleons – small momentum transfers are referred to as "soft" FSI, while large momentum transfers are called "hard" FSI.

Figures 1-3 c) and d) are identical except for the circles in c). These circles are there to convey the idea that the process can be calculated incoherently. In c), the idea is that 3NA can be described by the pion initially scattering quasi-elastically off of one of the protons, and then being absorbed by the remaining *pn* pair in a normal 2NA process. This type of 3NA mechanism is named for the initial scattering of the pion and is referred to as an initial-state interaction (ISI) process.

Figures 1-3 d) and e) are the most widely cited examples of what would constitute a "true" 3NA mechanism, one in which it is not possible to break the process into two steps which could be added incoherently.

The separation of FSI and ISI from "true" 3NA mechanisms is very artificial, especially in light nuclei where the distance scales between the interacting particles are necessarily small and there is a high probability that the intermediate particles are not on their mass shells [22]. One should not expect a distinct transition, but rather a smooth continuum. Nevertheless, calculationally the processes are different because ISI and FSI mechanisms can be modeled reasonably well classically, since the two steps involved have analogous free cross sections and by definition they can be added incoherently. This is not possible for the so called "true" 3NA mechanisms. While a quantum mechanical calculation of "true" 3NA in ^{3}He could be performed using the existing ^{3}He Faddeev wavefunctions [23] and the methodology of the Δ-hole formulation of the interaction [24, 25], it is a long and difficult calculation which has not yet been done. Thus experimentalists are left to compare their data to FSI and ISI models and to attribute that which is left over to "true" 3NA mechanisms. This differentiation is of course contradictory to the smooth transition one would expect from a "true" 3NA model (like Figure 1-3 d)) to a classical model (Figure 1-3 c)). More likely for light nuclei, if FSI or ISI signals were seen by experimentalists, they would be partial signatures of "true" 3NA mechanisms, but accessing that part of the mechanism where the intermediate particles are close to their mass shells. Of course, one cannot rule out the possibility that some "true" 3NA mechanisms may have signatures quite different than ISI or FSI.

For $A > 3$ nuclei, it is possible to speculate on mechanisms involving more than three nucleons, such as absorption on alpha clusters and "double-Δ" mechanisms, but since our focus will be on ^{3}He we will exclude these processes from consideration.

1.4 Rationale for Studying Absorption on ^{3}He

The ^{3}He nucleus is the simplest nucleus where 3NA could occur, and the study of π^+ absorption on this nucleus is appealing for a number of reasons. Experimentally, it is attractive because there are only protons in the final state. This fact eliminates the often difficult tasks of neutron detection and discrimination between protons, deuterons, and other heavy charged fragments. Five variables† are needed to specify the final state completely. Therefore, if the energy and angles of only two of the final state protons are measured, the final state is over-specified by one variable. This attribute is very useful, for a proton which was simply a spectator in the reaction may have little energy and thus be difficult to detect, yet its momentum vector can still be reconstructed from the other two higher-energy protons. Pion absorption on ^{3}He possesses the further advantages that there is neither a residual nucleus which may be left in various excited states, nor heavy nuclear fragments with unknown recoil momenta. Thus it is relatively easy to do kinematically complete experiments with this system.

Finally, absorption on ^{3}He is experimentally advantageous because the single final state available simplifies the analysis of the data. All cross sections can be expressed in terms of Fermi's Golden rule, which states that:

$$d\sigma = \frac{|M_{fi}|^2}{4E_\pi E_{target}|\vec{v}_\pi - \vec{v}_{target}|}\mathcal{D} \tag{1.1}$$

$$\mathcal{D} = (2\pi)^4\delta^{(4)}(\mathrm{p}_1 + \ldots + \mathrm{p}_\mathrm{n} - \mathrm{p}_\mathrm{total}) \prod_{n=1}^{N} \frac{d^3\vec{p}_n}{(2\pi)^3 2E_n}\,. \tag{1.2}$$

As a result, cross sections can be divided into a matrix element squared ($|M_{fi}|^2$) times a phase space factor ($\mathcal{D}$) for a particular final state. $|M_{fi}|^2$ contains information about the mechanism, while $\mathcal{D}$ is just the density of states. In absorption on ^{3}He where there is only one final state which consists of three protons, deviations from three-body phase space necessarily give information about the mechanism, $|M_{fi}|^2$.

Theoretically, ^{3}He is attractive in that realistic wavefunctions exist for the ground state nucleus [23, 26], it has a higher density than ^{2}H making it closer to the density of heavy nuclei, and the possible mechanisms are limited by the few nucleons that are involved. While it is not

---

†Three protons, each with three degrees of freedom in the final state, need nine variables. However, since the initial energy and momentum are fixed by the energy and directions of the incident pion, energy and momentum conservation reduce the number of necessary variables to five.

possible *a priori* to know whether the large multi-nucleon effects seen in heavy nuclei are 3NA, 4NA, or "n"-nucleon absorption, it seems reasonable to begin with a study of 3NA.

1.5 Previous Pion Absorption Experiments on ^{3}He

A number of experiments have previously studied π^+ absorption on ^{3}He in the Δ-resonance region. We review briefly only those experiments which have been performed since the advent of the meson facilities and which have also had the advantage of kinematical completeness.

At the energies just below the Δ-resonance, the 2NA and 3NA absorption cross sections were measured at $T_\pi = 62.5$ and 82.8 MeV by Aniol *et al.* [27]. Their experimental apparatus consisted of three NaI(Tl) telescopes and a plastic scintillator array.

The detectors were set up so that the detected protons and the incident pion beam formed (or nearly formed) a plane. This particular geometry will be referred to throughout this work as "in-plane," denoting the fact that the reaction plane contains or nearly contains the incident pion beam.

The 2NA cross section was measured by extrapolating $d\sigma_{2NA}/d\Omega$ over its unmeasured angular region using zeroth- and second-order Legendre polynomial terms. The angular coverage and statistics were not sufficient to determine whether higher order Legendre terms were necessary.

The coverage of three-body phase space by the experimental apparatus is difficult to determine from their paper. In addition, a correction to their 3NA cross section by a factor of nearly two was published without explanation [28], making it impossible to gauge the accuracy of the quoted results. However, from the general setup described the acceptance of the experiment for three-body phase space is almost certainly less than 1%. The corrected results of the experiment show evidence of 3NA at the 15-30% level of the total cross section. They claim that the energies of the final state protons in 3NA are distributed roughly like three-body phase space, but that there were possible deviations from three-body phase space in the angular distributions. However, because of the lack of statistics, they conclude that the angular deviations from isotropic three-body phase space may not be significant. The 3NA cross section was obtained by assuming that the unmeasured regions looked like isotropic three-body phase space and extrapolating over the unmeasured phase space.

The total absorption cross section was calculated by adding the 2NA and 3NA cross sections, and therefore it depends on the suitability of the extrapolations used in determining these cross sections.

In the Δ-resonance region, the measurements of Weber *et al.* [29, 30] cover the greatest number of different incident T_π energies of all the experimental groups. This group measured π^+ absorption at T_π = 64, 119, 162, and 206 MeV by using an experimental set up consisting of two banks of plastic scintillator set up in-plane.

An important result from this set of experiments was that at the low momentum part of the $d\sigma/dp$ distribution, the momentum of the least energetic proton was similar to the expected Fermi momentum. This fact was confirmed by the other experiments described here and is justification that "undisturbed" 2NA does exist and can be described as absorption on a *pn* pair with a spectator proton whose initial and final state momenta are equal. To measure the magnitude of the 2NA cross section, this experiment also used a zeroth- and second-order Legendre polynomial to extrapolate $d\sigma_{2NA}/d\Omega$ over the unmeasured angular region. Again, the angular coverage and statistics, while significantly better than that of Aniol *et al.*, were unable to rule out contributions from higher order Legendre terms which might have a significant impact on the procedure for determining the size of the 2NA cross section.

The 3NA cross section was most extensively examined at T_π = 119 MeV, where seven different angular regions were measured for a total coverage of three-body phase space of about 1%. The $d\sigma/dp$ distribution of the least energetic proton matched at high momentum that expected from three-body phase space. No statistically significant deviations from three-body phase space were seen in the 3NA cross section at this energy for the seven angular regions measured. At T_π = 64, 162, and 206 MeV, three, two, and one different angular regions were measured, respectively. These are too few angles for significant conclusions about the angular distributions.

The total π^+ absorption cross section was obtained by adding the 2NA and 3NA cross sections. The total absorption cross section measured by this experiment seemed to peak at a higher T_π than the total absorption cross sections measured in ^{2}H or ^{4}He, which is puzzling. The 3NA process, using the above assumptions, was about 15-25% of the total cross section, and this ratio showed little energy dependence.

In this experiment, they looked for but did not see a signature for a classical ISI or "hard" FSI mechanism. Therefore, they concluded that these mechanisms cannot contribute significantly to the 3NA cross section.

The other measurement directly in the Δ-resonance region was done at $T_\pi = 165$ MeV by Mukhopadhyay *et al.* They used a spectrometer for one of the arms and a large scintillator array for the second arm. The setup was primarily in-plane, with the angular coverage out-of-plane by the scintillator array being $\pm 15°$.

This group had a larger angular range for 2NA than the above two experiments. With this coverage, they found that the fit to their $d\sigma_{2NA}/d\Omega$ was substantially improved by the addition of a fourth-order term to the Legendre polynomial fit used by the above experiments. Their reported 2NA cross section changed by 15% if the fourth-order term was included. However, they were not able to establish firmly that a fourth-order term was necessary, since its need was based almost exclusively on their most forward data point. When $d\sigma_{2NA}/d\Omega$ is fit using only the zeroth- and second-order terms of the Legendre polynomial, the 2NA cross section measured is roughly in agreement with that of Weber *et al.*

With respect to the 3NA cross section, this group also found that the high momentum part of the distribution of $d\sigma/d\Omega$ for the least energetic proton had significant strength. This portion of the distribution was well fit using a three-body phase space model. However, they reported deviations from isotropic three-body phase space in the angular distributions of the 3NA cross section of about ±25%. They conclude that this systematic error prevents the 3NA cross section from being measured to better than ±25% by any experiment that uses a three-body phase space distribution to make large extrapolations over unmeasured regions.

This group also looked for classical two-step mechanisms. They found a lack of evidence for an FSI mechanism, but the situation with respect to ISI was not as clear. Some evidence for an ISI mechanism was perhaps indicated in one of the kinematic variables (the pseudo-invariant mass), but the results were not conclusive and seemed to be contradicted by the distributions observed in a different kinematic variable (the p-p angular correlations).

The total absorption cross section, derived from adding together the 2NA and 3NA cross sections, was about the same as that found by Weber *et al.* The contribution of the 3NA cross section to the total pion absorption cross section was measured by Mukhopadhyay *et al.* to be about 35%, but the measurement had large error bars.

The last measurements which may be relevant are two measurements by Smith *et al.* [31] at $T_\pi = 350$ and 500 MeV. While these two measurements are above the Δ-resonance region, the measurements may indicate the general trend of the cross sections that must be matched outside of the region.

The experimental setup employed by Smith *et al.* was similar to that used by Mukhopadhyay *et al.* In order to measure the 2NA cross section, Smith and his collaborators fit $d\sigma_{2NA}/d\Omega$ by scaling the ^{2}H $d\sigma/d\Omega$ distribution. This method does not give information about the underlying Legendre polynomial fit.

While the energy distribution of the the 3NA cross section was reasonably fit by three-body phase space, $d\sigma_{3NA}/d\Omega$ had large deviations from three-body phase space. Therefore they fit the polar angle of one of the protons in the laboratory frame to an arbitrary fifth order Legendre polynomial (they had measurements at seven different angles). This fit was used to extrapolate over the unmeasured regions of three-body phase space. To be comparable to previous experiments as well as to make what they call a lower estimate, they also reported the 3NA cross section assuming an isotropic three-body phase space distribution. At 350 and 500 MeV, these two measurements differed by 17% and 25%, respectively. The 3NA cross section measured using the Legendre polynomial fits were 45% and 47% of the total cross section at $T_\pi = 350$ and 500 MeV, respectively.

1.6 Summary of Known Facts and Unresolved Issues

A number of important things have been learned in the above experiments, but several key issues remain. Before discussing these issues, the facts that seem well established may be summarized:

1) A major fraction of the pion absorption cross section in ^{3}He can be described as absorption on a quasi-deuteron pair with a spectator proton. This is seen both in the angular distribution of the protons and in the low momentum region of $d\sigma/dp$ distribution for the least energetic proton. This mechanism seems sufficient to explain the 2NA cross section in the Δ-resonance region, since absorption through other mechanisms has been shown to be on the order of about 20 times smaller.

2) There is an indication that 3NA accounts for some non-negligible fraction of the absorption cross section in ^{3}He.

3) All of the experiments on ^{3}He so far have found that the high momentum region of the $d\sigma/dp$ distribution of the least energetic proton is distributed roughly according to three-body phase space.

4) No signs indicative of a “hard” FSI type mechanism have been found.

The issues which either were not addressed by the above experiments, or about which there are conflicting results are as follows:

1) None of the experiments were significantly out-of-plane; moreover the measurements required large (factors of 100 or more) extrapolations over the out-of-plane regions. These extrapolations make it difficult to assess the true size of the 3NA cross sections and thus their significance.
2) There are conflicting claims about the angular distribution of the 3NA mechanism in-plane. Deviations, if present, have not been measured with substantial angular coverage.
3) The 2NA cross sections which have been reported have a significant dependence on whether a fourth-order term is necessary to fit $d\sigma_{2NA}/d\Omega$ over the entire angular range; the size of this term may be non-negligible for the extraction of the 2NA cross section.
4) The total absorption cross section has not been measured in a model-independent manner, and it may contain large systematic uncertainties. Furthermore, the peaking of the total cross section in ^{3}He at larger T_π than in ^{2}H and ^{4}He needs confirmation.
5) Because both the total and three-nucleon absorption cross sections are based on such large extrapolations, the fraction of the cross section attributable to 3NA has large and unquantified systematic uncertainties.
6) There is a controversy as to whether or not ISI has a role in 3NA.
7) The mechanism(s) responsible for 3NA is unknown. Whether or not 3NA can be explained by some combinations of the diagrams in Figure 1-3 b)-e) or whether other more exotic processes are needed has not been determined. Moreover, there are few experimental differential quantities which can illuminate the nature of the mechanism involved or serve as a basis for comparison for the various rival processes which have been proposed.

These outstanding controversies and issues motivated this study of pion absorption on ^{3}He in the Δ-resonance region. The experiment was designed to provide quantitative, model-independent answers to as many of the above points as was feasible. It is hoped that this experiment will lead to a more comprehensive understanding of multi-nucleon pion absorption in this energy region and that the information gained will illuminate the mechanism responsible for multi-nucleon pion absorption, at least with respect to 3NA.

This review of the prior experimental situation which motivated the present experiment has been necessarily brief and narrow in focus; for a broader review of pion physics at these energies, there are several articles that are particularly worthy of mention. C. H. Q. Ingram gives a brief overview of the field of pion-nucleus interactions which is very lucid and continues to be relevant in the years since its publication [32]. For a more comprehensive overview focusing exclusively on issues related to pion absorption in light nuclei, the review by H.J. Weyer [33] is of merit. Both of the above reviews greatly aided the preparation of this chapter. Other reviews that deserve mention are those by Ashery and Schiffer [34], Redwine [35], and more recently by Ingram [36].

Chapter 2

The Experimental Apparatus

2.1 Primary Design Goals for the Detector

The LADS detector was designed specifically for the study of multi-nucleon absorption of pions. Its construction was motivated by a desire to answer those issues discussed at the end of the last chapter, along with similar issues for heavier nuclei. To this end, LADS was designed to measure multi-particle final states with high statistics, good energy and angular resolution, and as much phase space coverage as possible.

To meet these design goals, the detector needed to have the following characteristics:

1) To minimize the extrapolations over unmeasured regions, the detector needed an angular acceptance as close to 4π steradians as possible.

2) For the same reason, it also needed a low threshold so that low energy particles would not escape detection.

3) If the individual components of the detector could only detect one particle per event, then the number of components needed to be large with each covering only a small portion of phase space. Otherwise, because multi-particle final states were to be studied, large extrapolations would be necessary to correct for those events where two particles enter the same component.

4) To study these multi-particle final states, the energy resolution of the detector needed to be "sufficient." It was decided early on that energy resolution was not as important as phase space coverage, but that a resolution of 3-5% for the summed energy of the event was probably sufficient and achievable.

5) The maximum energy the detector needed to be able to measure was dictated by the probable energies of the final state protons in pion absorption, subject to cost constraints. The stopping power of a material grows roughly linearly with its thickness, but the detector volume (which is closely related to the detector cost) for a 4π detector grows as the thickness cubed. The compromise that was settled upon was the ability to measure a maximum proton energy of at least 200 MeV, but with a higher maximum energy (≈ 250 MeV) in the forward direction.

6) The angular resolution of the detector, in the same manner as its energy resolution, needed to be good but not necessarily excellent. The detector needed to be able to detect angular variations in the cross section, which implied an angular resolution of only a couple of degrees for charged particles. However, the minimum acceptable angular resolution was set by the need to reconstruct the positions of the reactions along the z-axis. This ability was needed so that the large background from the target entrance and exit windows could be removed during data analysis. A z-resolution of approximately two millimeters at the beam axis was required, given the size and shape of the target cell. This z-resolution necessitated an angular resolution of better than 10 mr for charged particles.

7) Since the detector was to study many different nuclei, the identification of final state particles was particularly important. The final state particles between which the detector needed to discriminate included charged pions, protons, neutrons, deuterons, γ's, and possibly tritons.

8) The measurement of the energy of the neutrons and the desire to have large phase space coverage are largely incompatible goals*. However, the detection of neutrons along with the measurement of their direction is possible and can provide valuable information, especially with regard to the number of nucleons participating in the absorption reaction. Therefore, the detection and measurement of the direction of the neutrons was given a relatively high priority.

---

*The energy measurement of neutrons at energies of 20–200 MeV can only be done using a time-of-flight method requiring flight paths of a couple meters or more. When combined with the requirement of 4π steradians acceptance, the detector becomes huge and its price exorbitant.

9) The detector was designed to be used in the πM1 area at the Paul Scherrer Institute in Villigen, Switzerland. One wanted to be able to utilize fully the relatively high beam rates available from the πM1 channel so that high statistics could be collected.

10) Finally, the linearity of detector response was considered to be very important, so as to simplify the analysis of the data.

A detector that met the above goals would have a number of advantages over previous experimental apparatuses. In particular, it would not be an in-plane detector, and large extrapolations over unmeasured regions of phase space would not be needed. This would allow both the total and the two-, three-, and four- or more nucleon absorption cross sections to be measured without large, model-dependent, extrapolations. The planned neutron detection and large acceptance would allow the question about the number of nucleons participating in multi-nucleon pion absorption to be addressed. With the planned energy and angular resolution and the ability to collect high statistics quickly, deviations from phase space would be readily apparent and could be investigated through the use of multiply differential cross sections. These investigations seemed like the best opportunity the nuclear physics community would have to come to an understanding of the mechanism responsible for multi-nucleon absorption.

2.2 Rationale for the Design of LADS

The collaboration decided that the best way to achieve the above design goals was with a detector of cylindrical geometry whose main components were plastic scintillators and multiwire proportional chambers (MWPC's). The plastic scintillator would measure the energy of the charged particles and also detect and measure the direction of neutral particles, while the MWPC's would provide accurate angular resolution and vertex reconstruction of the charge particles. This combination has several important advantages over a detector whose main component is a magnetic spectrometer or an inorganic crystalline scintillator.

A detector based on a large magnet was considered briefly, but its cost would have been considerably more than the other alternatives. The advantages of a magnetic spectrometer, better energy and angular resolution along with the ability to measure the charge of the final state particle, seemed unlikely to be essential for an understanding of multi-nucleon pion absorption. Most important was large multi-nucleon phase space coverage. It is more difficult to achieve nearly full acceptance with a magnetic spectrometer than with a detector whose main component is scintillator. In any event, to detect neutrons a magnetic spectrometer would need to be supplemented with plastic scintillator. Thus the greater cost (which at a minimum was estimated to be several times the total cost of LADS) did not seem justified for the advantages which were of uncertain merit for pion absorption experiments envisioned. However, since a magnetic field is needed to determine of the sign of the charge of pions in the final state, and since this could be important for future experiments that do not focus on absorption, the possible later addition of a magnet was a factor in the initial design of LADS. To facilitate the possible addition of a magnet, a significant amount of magnetic shielding was provided for the photomultiplier tubes (PMT's) used in the detector, as their performance is inhibited by magnetic fields.

A detector based on an inorganic crystalline scintillator like NaI(Tl) or BGO was also considered. The advantages obtained from using inorganic scintillator materials are a better energy resolution ($\approx 1\%$) and a higher gamma detection efficiency. The disadvantages of this material are its inability to detect neutrons efficiently and the slowness of the response, which would not allow full utilization of the beam rates available at the accelerator. Inorganic scintillator material is also considerably more expensive than plastic scintillator. The disadvantages of using inorganic scintillator were judged by the collaboration to outweigh its advantages.

The cylindrical design of the detector was chosen over a spherical design for a number of reasons. One reason is that it is difficult to construct a spherical detector that is layered and yet has no dead regions; the problem being how to get the light produced in the inner scintillator layers out to the photomultiplier tubes. Further, it is possible to make very low mass cylindrical wire chambers; the technology for low mass spherical wire chambers, without significant dead regions within the active volume, does not exist. Finally, the construction of the detector is much simpler for a cylindrical design.

2.3 A Brief Description of LADS

LADS is shown in Figure 2-1 and its capabilities are summarized in Table 2.1. LADS has a cylindrical shape, with the axis of the cylinder aligned with the incoming pion beam. It uses plastic scintillator bars to measure the energy of charged particles and to detect neutrons. It has two cylindrical multi-wire proportional chambers that provide position information for charged

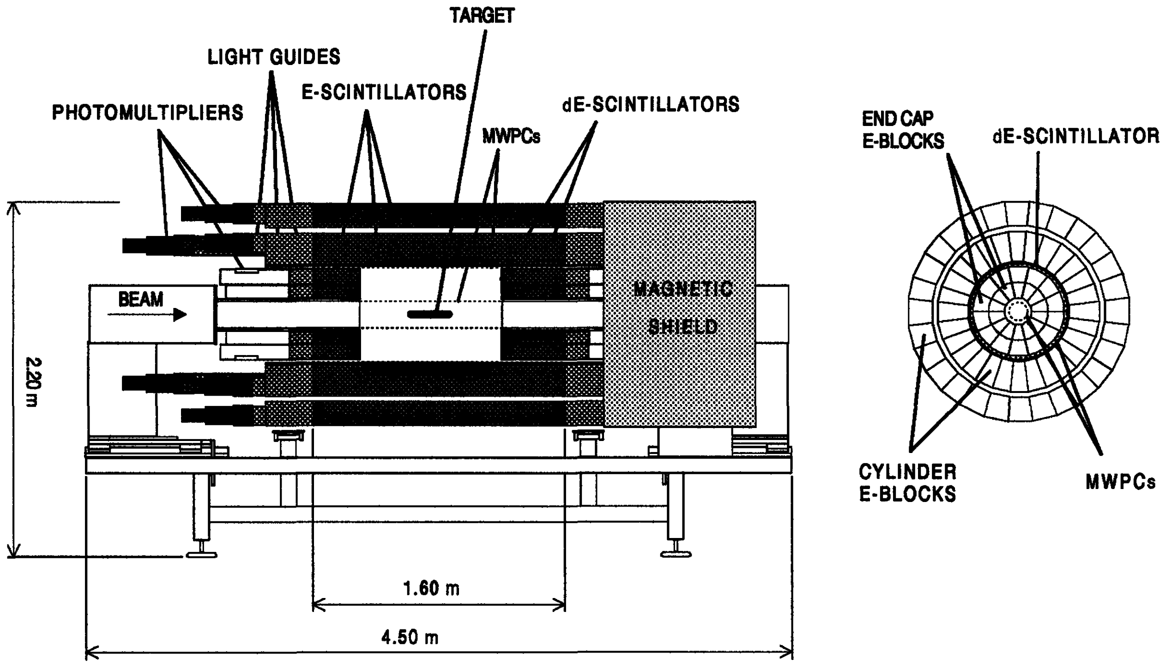

Figure 2-1: A scale drawing of the LADS detector, adapted from reference [37].

LADS's Performance

Solid angle acceptance	98.5% of 4π sr
Energy threshold for protons	< 20 MeV
Maximum proton energy that can be measured	> 200 MeV
Energy resolution for an absorption event	3-5% (FWHM)
Energy resolution for 100 MeV protons	3 MeV (FWHM)
Ability to separate charged particles	$\pi's$, p's and d's
Vertex resolution from two tracks	1 mm (FWHM)
Angular resolution	$< 1^\circ$
Angular resolution for neutrons	$\approx 10^\circ$
Detection efficiency for neutrons	$\approx 35\%$
Ability to separate neutral particles	n's and γ's

Table 2.1: Summary of LADS's performance capabilities.

particles. Each end of the cylindrical detector is closed with an "endcap," which is also made of plastic scintillator.

There are 28 plastic scintillator sectors in the cylindrical part of LADS, with each sector consisting of three bars of plastic scintillator, 1.6 m long and aligned parallel with the beam axis. Each of the three bars has a trapezoidal cross section so that the counters fit together with minimal gaps and dead regions. The scintillator bars are read out by two PMT's, one at each end of the bar. The bar nearest the beam is called the cylinder ΔE (CD) and is 4.5 mm thick and at a radius from the beam axis of 29.8 cm. The middle bar is called the cylinder inner E-block (CI) and is 20 cm thick and located approximately 2 mm behind the CD counter. The bar farthest from the beam axis is denoted as the cylinder outer E-block (CO). Each CO is 15 cm thick and there is a 3 cm air gap between the CO and CI counters. This ΔE-E-E arrangement is capable of stopping normally incident protons with 200 MeV of kinetic energy. At angles that are not perpendicular to the beam axis, higher-energy protons are stopped.

Each endcap has 14 sectors, but the ΔE counters (ED's) are offset from the E-counters by one-half a sector width. This arrangement approximates the 28-sector segmentation of the cylinder for particles that penetrate an ED and one of the endcap E-blocks. The two endcap E-blocks are also named inner and outer E-blocks, with the one closest to the beam axis called the endcap inner E-block (EI) and the one furthest from the beam axis called the endcap outer E-block (EO). The edge of the EI closest to the beam axis is cylindrically shaped, as is the edge of the EO furthest from the beam axis. The EI's and the EO's are aligned concentrically with each other and meet at a 14-sided polygonal surface. The upstream EO's and EI's are 30 cm long, while the downstream EO's and EI's are 40 cm long. Both the upstream and downstream EO's and EI's have a PMT which is attached to each E-block on the end furthest from the center of the detector. The front face of both the EI and EO are covered by the ED, which is 4.5 mm thick. Each ED is also read out by a single PMT which is connected via a light guide to the edge of the ED which is furthest from the beam axis.

The two MWPC's are cylindrical, with the inner MWPC at a radius of 6.4 cm and the outer MWPC at a radius of 28 cm. Each MWPC measures the azimuthal angle (ϕ) and the distance along the beam axis (z) of the charged particle's intersection with the MWPC.

2.4 Target Container

The early LADS experiments have focussed on ^{2}H, ^{3}He, and ^{4}He. All of these atoms are gaseous at standard temperature and pressure, though they can be liquified at very low temperatures. The container for the target nuclei needed to be able to hold the target material at a high density, so that adequate luminosities could be obtained. To obtain the necessary density, the choices were limited to cryogenic liquid targets or high pressure gas targets. In considering these two choices, a novel high pressure gas target proposed by our University of Basel collaborators proved to be most suitable for LADS.

There were several reasons why the proposed high pressure gas target was more desirable for LADS than a cryogenic target. A significant problem with a cryogenic target is the space necessary around the target region for the equipment which is used to keep the target cold. With the desire to have nearly 4π steradians acceptance, there was no space for the necessary connections, reservoirs, etc., that would go along with a cryogenic target. The proposed gas target needed only one thin, flexible metal tube for filling the target. The other advantage of the gas target was that its density was easy to calculate accurately and, since it was relatively long, the percentage error in the thickness was very small. The accurate determination of the density and thickness of the target was necessary to measure the absorption cross sections accurately.

The target cell was a cylindrically shaped vessel 25.7 cm long with an inner diameter of 4 cm and had a rounded cap at each end of the cylinder. It was manufactured by Dornier Ltd. [38] and was made out of three layers of carbon fiber and epoxy. The inner layer of the target was 10 μm of Ag followed by 20 μm of Cu. This inner coating ensured that the target gas could not diffuse out or react with the carbon fiber or epoxy. The target walls were very thin (see Table 2.3) and yet could safely hold over 100 bars of pressure. The thin walls were important because LADS's design called for a low threshold for the detection of protons, and the target walls and MWPC's dominated the material between the interaction point and the detector, as shown in Table 2.3. The ends of the target were of the same construction as the walls. Their thinness helped increase the ratio of events from the target gas to events coming from the target container, and thus increased the useful fraction of the events that LADS detected.

At the very end of the cylinder where the transition was made from the cylindrical part to the rounded ends, the target was reinforced with extra layers of carbon fiber and epoxy. This reinforcement on the downstream end was 3.3 cm long and on the upstream end it was 3.6 cm long. Because only the center 20 cm of the target was used, few events used in the

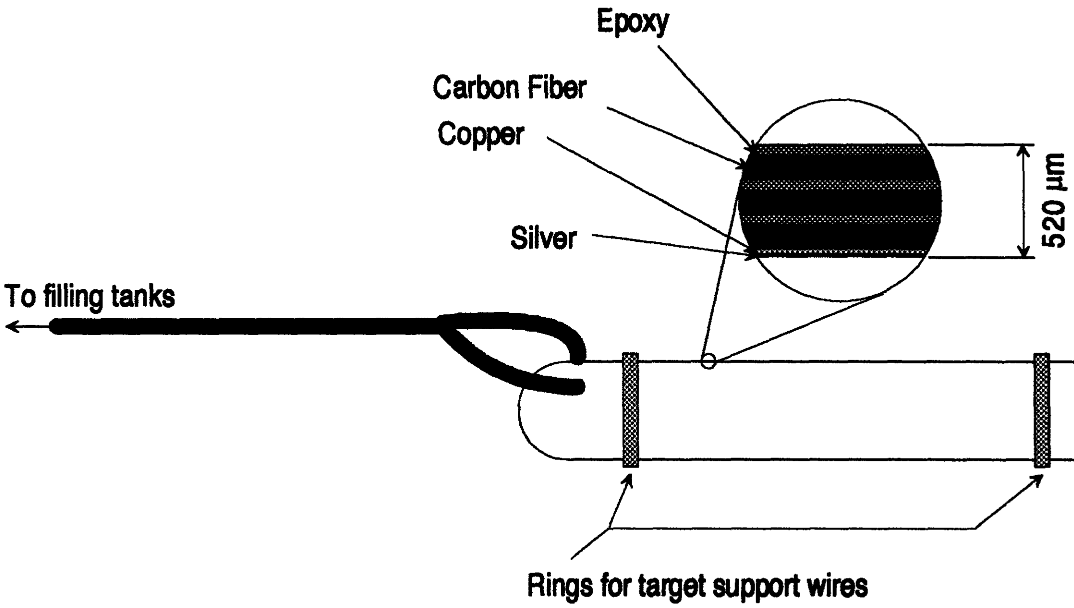

Figure 2-2: A schematic drawing of the target cell used in LADS [39].

analysis had scattered particles which passed through these regions. The total weight of the target container, excluding the filling pipes, was about 51 g.

The target was suspended in place by three wires which were connected to two support rings attached to each end of the target.

The pressure used for the ^{3}He data runs was 95 bars at 32° C. ^{3}He is expensive, and the amount needed to fill the target was large, so the full recovery of the gas was important. These requirements meant that the filling and emptying of the target was a slow and painstaking process. Therefore, to reduce the risk of losing the ^{3}He gas and make efficient use of the beam availability, the target was filled with ^{3}He only once during the 1991 experimental run.

For the other gases, which were cheap and available in high pressure containers, a target change could be done in a couple of hours. For the ^{2}H runs, which were primarily for calibration of the detector, several different pressures were used. The target was filled and emptied several times so that ^{4}He could be run at the same energy and chronologically close to a ^{2}H calibration run. The pressures for the ^{2}H runs were 98.7, 94.8, and 74.4 bars for T_π = 118, 162, and 239 MeV, respectively.

The target cell used for the 1989 and 1991 experimental runs developed a leak a couple of days before the end of the 1991 run and has been replaced by a target cell of similar design but with slightly different specifications.

2.5 Multi-Wire Proportional Chambers

The MWPC's are very low mass, cylindrically shaped position detectors capable of handling the high beam rates to which they are exposed ($\approx 1 \times 10^6$ hits/sec). There are two of these MWPC's, both of essentially the same design and concentric around the beam axis. The MWPC closest to the beam axis is called the inner chamber, while the one with the larger radius is called the outer chamber. The inner chamber is 90 cm long with a radius of 6.4 cm. The outer chamber is 160 cm long with a radius of 28.0 cm.

Each MWPC has one anode plane with two cathode planes, one on each side of the anode plane. The anode plane of each MWPC consists of gold-plated tungsten-rhenium wires, 20 μm in diameter, which are strung along the length of the chamber. The inner MWPC has 192 wires evenly spaced around the circumference; the outer chamber has 832 wires.

The cathode planes of the MWPC chambers consist of Kapton foil covered with a 50 μm layer of Al. On the side that faces the anode wires, the aluminium was scratched with an air powered dentist's drill mounted on a large computer controlled Hewlett Packard plotter to remove strips .6 mm wide, the entire length of the foil. The strips are spaced 3.3 mm apart on the inner chamber, and 4.4 mm apart on the outer chamber. The gaps between the cathode planes and the anode plane are 3 mm and 4 mm on the inner and outer chamber, respectively. The cathode planes were glued to Rohacell cylinders, in such a manner that the Al strips spiral around the beam axis. The inner and outer planes on each chamber spiral in opposite directions.

The gap between the cathodes was filled with a gas mixture of 49.8% C_2H_6, 0.2% Freon, and 50% Ar, which was flushed through the chambers at a rate of 20-30 cm^3/min. During operation, voltages of +2350 V and +2800 V were applied to the anode wires on the inner and outer chambers, respectively.

The MWPC's were designed to have very low mass. This low mass is necessary to provide a low detection threshold for charged particles and to reduce the multiple scattering of the

MWPC Specifications	Inner MWPC	Outer MWPC
Radius	6.4 cm	28.0 cm
Number of wires	192	832
Wire spacing	2.094 mm	2.114 mm
Number of cathode strips	384	560
Cathode strip width	2.7 mm	3.8 mm
Cathode spacing	0.6 mm	0.6 mm
Strip angles (inner, outer plane)	34.25°, 41.19°	45.86°, 44.21°
Anode-cathode gap	3 mm	4 mm
Anode HV	$\approx +2350$	$\approx +2800$

Table 2.2: Summary of the MWPC parameters.

particles, since a large amount of multiple scattering would limit the measurement of the particle trajectories.

The MWPC's were constructed primarily out of aluminized Kapton and Rohacell. The layers on the inner chamber were arranged as follows: a layer of aluminized Kapton 25 μm thick was glued to the inside of a 2-mm-thick Rohacell cylinder; on the other side of the Rohacell cylinder the cathode plane was glued; then there was the gap filled with MWPC gas and the anode wires. This construction was repeated on the other side of the anode wires; thus the entire inner MWPC was: grounding plane, rohacell, cathode plane, anode plane, cathode plane, rohacell, grounding plane. For the outer MWPC, the construction was essentially the same as for the inner MWPC, except that the grounding plane was 50-μm-thick aluminized Kapton and the Rohacell cylinders were 3 mm thick. Also, since the length of the outer MWPC was greater, the wires were supported in the middle of the chamber by a Rohacell strip, which was about 3 mm wide by 4 mm deep. This support prevented the wires from sagging, but in the region of this Rohacell strip the chamber was inactive.

When charged particles passed through the chamber, the MWPC gas between the two cathodes is ionized. The electrons that are freed migrate toward the positively charged anode wires. Near the wires, where the electric field is large, the electrons pick up enough energy between collisions with the MWPC gas to knock out other electrons. This effect amplifies the signal in the region of the anode wires. The collection of the primary and secondary electrons on the anode wires takes less than a nanosecond. The signal that is detected on the anode is not from the collection of the electrons, which occurs too quickly for the electronics to react to, but is instead from the induced mirror charge produced on the wire from the charged ions left behind. As the ions disperse toward the cathodes, this mirror charge lessens and is detected by the electronics on the anode wires. The signal on the cathodes comes from the collection of the ions on the cathode strips.

In this experiment, the signals from both the cathodes and anodes were read out. The anode signal triggered charge discriminators, while the charge collected by the cathodes was read out via analog-to-digital converters (ADC's). While only one or two anodes fire when a charge particle passes through the chamber, the typical cluster width of the cathodes is four strips. The central cathode strip records more charge than the ones farther from the intersection. The distribution of the charge on the cathode strips for a single crossing is roughly Gaussian in shape. The mean of this Gaussian, and thus the centroid of the charge cascade caused by the primary and secondary electrons, could be determined to slightly better than 1 mm. However, the cascade is centered on the anode since most of the ionization comes from the secondary electrons, so the resolution of the chamber in the ϕ direction is limited to about 1 mm. The inner and outer strips of the cathode planes of each chamber spiral in opposite directions, so the two cathode planes can be used by themselves to determine the place of intersection of a charged particle with the MWPC.

The pitch of the cathode strips is such that cathode strips on the inner and outer cathode planes of a chamber usually cross twice. Thus there is an ambiguity in determining where a charged particle crossed if only the cathode planes are used. This ambiguity is usually resolved by comparing the ϕ's of the two possible crossings determined from the cathode planes to the ϕ determined from the anode wires.

Since the inner chamber has a much smaller radius, the angle of the cathode strips would have to be very shallow if the number of cathode crossings was to be kept to only two over the length of the chamber. This limitation was undesirable because the resolution in the direction of the beam axis is proportional to $1/\sin\theta$, where θ is the cathode strip angle measured from the beam axis. To reduce the number of crossings without reducing the angle of the cathode strips, a method was devised to reduce the "effective length" of the inner MWPC by one-half. Each of the inner MWPC cathode planes had a scratch about 2 mm wide perpendicular to the beam axis in the middle of the chamber. This scratch electrically isolates the upstream and downstream ends of a cathode plane. Both the upstream and downstream ends of the inner MWPC cathode planes were read out, so that there were effectively two separate MWPC's, each one-half the length of the inner MWPC but with a common anode plane.

The cathode strips were connected to LeCroy TRA1000 current sensitive preamplifiers followed by PSI-built postamplifiers. The postamplifiers were connected to CAMAC LeCroy

2282B ADC's, which were combined with LeCroy 2280 pedestal subtracting and data compacting modules. The anode wires were read out using the LeCroy PCOS III system.

2.6 Plastic Scintillator

2.6.1 Cylinder ΔE's

The purpose of the ΔE's is to provide information for particle identification and for the energy determination for particles that do not penetrate to the E-blocks. The ΔE's separate charged particles from neutral particles because the light is produced in the scintillator only by ionizing radiation. Therefore charged particles leave signals in the ΔE's, while neutral particles, because of the thinness of the ΔE's, have only a 0.5% chance of producing a signal via a nuclear reaction in the scintillator that produces ionizing particles. Charged particles are further separated into pions, protons and deuterons by using the energy and timing information provided by the ΔE's. When dE/dx for penetrating particles is graphed versus energy (see Figure 4-3 a)), the particles lie in bands according to their masses. For slow particles that do not penetrate into the E-blocks, the quantity $1/\beta$ can be calculated from the timing information and the flight path length as determined by the MWPC's; when $1/\beta$ is graphed versus energy, bands of particle types are also seen (Figure 4-3 b)).

The design of the ΔE's focused on the optimization of their energy and timing resolution since these were needed to provide the best possible particle type separation. Energy and timing resolution are both proportional to $a/\sqrt{n}$, where a is a constant explained below and n equals the number of photo-electrons produced at the photocathode of the PMT. For a minimum-ionizing particle intersecting the ΔE at the center of the counter, approximately 25 photoelectrons are collected in a PMT attached to one end. Having a PMT on each end of the scintillator increases the amount of light collected and improves the energy and timing resolution by roughly $1/\sqrt{2}$. It also makes the analysis much simpler since the energy and timing resolution can then be made largely position-independent.

The energy E deposited in the scintillator is linearly proportional to the light produced, L_0. However, what is measured is the light collected by the upstream and downstream PMT's, L_u and L_d respectively, which is attenuated exponentially as it travels through the scintillator.

The energy is measured independently of position by using the geometric mean of the light collected in each PMT. These quantities may be described as:

$$E = b_0 L_0 = b_1 \sqrt{L_d L_u}\ ; \tag{2.1}$$

$$L_d = L_0 \exp{(l - x)/\lambda}\ ; \tag{2.2}$$

$$L_u = L_0 \exp{(x - l)/\lambda}\ , \tag{2.3}$$

where x is the position the particle hit measured from the upstream PMT photocathode and l is the distance between the upstream and downstream PMT's.

The particle's time of flight (TOF) to the scintillator is also measured using a method that is independent of where the particle hit the scintillator. Specifically, the TOF is obtained by using the arithmetic mean of the up and downstream time-to-digital converter (TDC) data:

$$\mathrm{TDC}_u = \mathrm{TOF} + (l + x)c_{scint}; \tag{2.4}$$

$$\mathrm{TDC}_d = \mathrm{TOF} + (l - x)c_{scint}; \tag{2.5}$$

$$\mathrm{TOF} = (\mathrm{TDC}_u + \mathrm{TDC}_d)/2 - \text{constant}, \tag{2.6}$$

$$\tag{2.7}$$

where c_{scint} is the speed of light in the scintillator. The use of constant fraction discriminators on all PMT's made the timing measurements independent of pulse height.

The timing resolution was found to vary with the type of PMT; *i.e.* the constant a in the equation $a/\sqrt{n}$ mentioned above was a characteristic of the PMT. Various 1″ and 1 1/8″ linear stage PMT tubes were tested, and the Hamamatsu R1355 was found to have the best timing characteristics. A timing resolution of 0.7 ns (FWHM) was measured with these tubes for minimum-ionizing particles penetrating the middle of the ΔE's. The PMT's were purchased as a custom hybrid photodetector which included the PMT and a custom resistive base all potted together in a μ-metal housing for magnetic shielding. This shielding extended 15 mm past the front face of the photocathode.

The scintillator has a trapezoidal cross section which is 4.5 mm thick with the inner edge 6.63 cm and the sides 6.4° from normal; the purpose of the beveled edges is to keep the gaps between the ΔE's as small as possible. The scintillator is 1.6 m long and consists of BC-408 [40], while the light guides are made with four strips of ultra-violet transmitting plastic. These strips were heated and twisted so that at one end they match the scintillator and at the other end

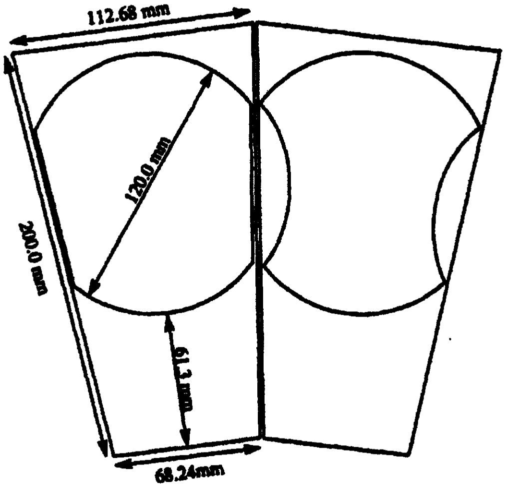

Figure 2-3: A scale drawing of the cross section of the light guides for the cylinder inner E-blocks [41].

they fit within the area covered by the photocathode. This adiabatic-twisted-strips design was compared with light guides made with bundles of plastic optical fiber as well as with light guides made from a solid piece of ultra-violet transmitting plastic which was machined to go smoothly from a cross section matching that of the scintillator to a cylindrical cross section the size of the PMT's photocathode. This latter design resembled a "fish tail." When tested, the adiabatic-twisted-strips design proved to collected approximately 20% more light than the fish-tail designs, and about 100% more light than the light guides made with optical fiber.

2.6.2 Cylinder Inner and Outer E-blocks

The cylinder E-blocks are made from plastic scintillator, BC-408 [40], and are 1.6 m long with a trapezoidal cross section. The front and back faces are parallel, but the sides are inclined at an angle 6.4° from the normal to the front face. This shape allows the scintillator bars to fit closely together, forming a barrel which has the cross section of a regular 28-sided polygon. The inner E-blocks are 20 cm thick and the outer E-blocks are 15 cm thick.

Each end of the E-blocks is read out with a Hamamatsu R1250 $5''$ PMT [42], which is connected to the scintillator via Lucite light guides. The cross section of the light guide is the same as the scintillator for the first 30 cm. After that, there is another section of light guide that couples to the PMT which is no bigger than the diameter of photocathode of the PMT. This is done so that a magnetic μ-metal shielding can extend over the last $\approx$ 10 cm of the light guide and shield the photocathode from magnetic fields. On the CI's, two different cross sections were needed for this part of the light guide, as shown in Figure 2-3. Because there is not enough space on the inner E-blocks for the PMT's to fit next to each other, the tubes on alternate CI's need longer light guides. These light guides, with concave sides, are longer and extend past the PMT's of the adjacent CI's. On the CO's, where there is more space, the light guides that couple to the PMT are cylindrical and only a few centimeters long. The overall design of the light guide was done with computer simulations and scale models to maximize the light collected and the linearity of response versus position of the incident particles.

The advantage of the cylinder E-blocks having a PMT on each end is substantial. The energy and TOF measurement can be made position independent, as described in the previous section. Also, instrumentation of both ends allows the determination of the position of neutral particles that convert in the E-block. This is done by using the timing difference of the light detected by the upstream and downstream PMT's, which provides z-position information. Combined with the sectorization of the scintillator in ϕ, and with the vertex which can be determined from the charged particles in the event, it is possible to have an angular resolution for neutral particles of about 10°. This information is of particular importance for nuclei heavier than ^{4}He, where kinematic completeness is lost and in which there may be multiple neutrons in the final state.

The threshold for an E-block is 2.5 MeV electron equivalent light, deposited anywhere in the E-block. The largest pulse a PMT needs to handle without saturating is a proton depositing $\approx$ 400 MeV equivalent of light close to the photocathode. The attenuation of light from one end of the E-block to the other is about a factor of two. Thus the dynamic range of signals the PMT's need to amplify linearly is a factor of 400. Also, the rate of pulses could be as high as 10^5 per second. To deal with these requirements, a passive PMT base was designed with the signal being taken from the 11^{th} dynode. The base is more fully described in reference [43].

An energy resolution of 2.5% FWHM was achieved under controlled test conditions consisting of a 100 MeV proton beam in a CI counter. A timing resolution of 300 ps FWHM was also achieved for these 100 MeV protons. These facts attest to the excellence of the light collection achieved by these long bars and of the intrinsic timing characteristics of the R1250 PMT's when used with the bases designed by the collaboration.

2.6.3 Endcap ΔE

Each endcap has 14 ΔE counters consisting of 5 mm thick plastic scintillator oriented perpendicularly to the beam axis. The set of 14 forms an annulus, completely covering the front faces of the EI's and EO's. The edge of each ED closest to the beam axis is an arc, $1/14^{th}$ of a circle centered on the beam axis with a radius 8.8 cm. The outer edge of each ED is also an arc, $1/14^{th}$ of a concentric circle with a radius of 25.8 cm. The other two edges are straight and located at constant ϕ with respect to the beam axis.

The annulus formed by the ED's is rotated azimuthally around the beam axis with respect to the EI's and EO's by one-half a sector width. This is done so that the combined information from the ΔE and E can be used to improve the angular resolution.

The light from the ED's is obtained using 5mm thick light guides attached to the edge farthest from the beam axis. They run along the outer edge of the endcap until each light guide is coupled via a "fish tail" to a PMT. These PMT's are identical in every respect to the ones used for the CD's. The 5 mm light guide caused a layer of dead material between the endcap and the main cylinder; however, the affected phase space is small and occurs only for particles that have been detected. When the particle penetrates through the ED light guide and into the cylinder, the energy loss program corrects for the dead region caused by the light guide.

When the ED's were tested with a ^{137}Cs source, the size of the PMT signal varied greatly with the position of the source. Surprisingly, when the source was closest to the beam axis larger signals were produced than when the source was closer to the light guide. This position dependence was largely eliminated by painting the edge closest to the beam axis black.

2.6.4 Endcap Inner E-Block

Each endcap has 14 inner E-blocks, also made out of plastic scintillator. The E-blocks on the downstream endcap are 40 cm long, and on the upstream endcap they are 30 cm long. When assembled, the edge of the E-blocks closest to the beam axis form a cylinder with a radius of 8.8 cm, while the opposite sides have the cross section of a regular 28-sided polygon.

The light is collected via light guides connected to the face of the scintillator furthest from the target. These light guides are then connected to Philips XP2262B 2″ PMT's. The areal matching between the scintillator and the tubes is about 40%. The design of the light guides was done both with computer simulations and by testing prototypes using cosmic rays. The best light collection efficiency and response uniformity was obtained by a light guide 20 cm long and with the same cross section as the inner E-block, followed by a short 7 cm cylindrical piece that coupled to the PMT and provided space for the magnetic shielding to protrude past the photocathode.

2.6.5 Endcap Outer E-Block

The 14 outer E-blocks of the endcap are aligned with the EI's, and of the same length as the EI's on each endcap. When assembled, the EO's outer edge forms a cylinder with a radius 25.8 cm. Their edge closest to the beam axis is a regular 28 sided polygon and fits flush with the EI's. The light guides of these scintillators are similar to the ones on the EI's and the PMT's are 3″ Philips XP2312B.

2.6.6 Endcap Veto

Along the inner radius of the endcap there are 14 "veto" counters that are 1 mm thick and form a ring of scintillator the entire length of the EI's. These are coupled via lucite light guides to 1/2″ Philips XP1911 PMT's. These were included to detect contamination of events from background due to the beam halo, but have so far been little used during the analysis.

2.7 Construction of the Detector

The inner and outer cylinder E-blocks are each wrapped in one sheet of Aluminum foil. In addition, between each pair of adjacent counters is one sheet of 25 μm thick two-sided aluminized mylar. On the CI's, the mylar extends past the inner edge of the counters, and is used, as described later, to support the cylinder ΔE scintillators and light guides.

The E-blocks are held in place like a barrel, with two steel bands drawn tightly around the cylinders at the light guides. The light guides were very slightly wider than the scintillator, so that they bear most of the compression from the steel bands.

The PMT's were glued in place horizontally, using Dow Corning Silgard [44] an silicone based optical epoxy. After mixing according to the directions, placing it in a partial vacuum to remove bubbles, and letting it set up for 5-10 minutes, a small amount of the silicone epoxy was poured onto the upturned face of the PMT. This was allowed to set up for an additional 15-30 minutes, and was within minutes of losing its ability to flow. At this critical juncture, the PMT was pressed onto the light guide, which had been previously prepared with three 1 mm clear plastic spacers attached with the same silicone adhesive. Pressure was continuously applied from behind with springs for the next hour or so. If all went well, a good optical connection with few, if any, air bubbles was the result. This connection has excellent mechanical strength, yet the PMT can be removed easily if the seal between the photocathode and lucite is pierced with a sharp object, such as an Exacto knife. The remaining silicon adhesive peels off easily, leaving both PMT and light guide like new. Consistent success with this method can be achieved after some practice; the critical step is learning when the consistency of the silicone adhesive is just right for the application of the PMT to the light guide[†]. Too early and all the silicone runs out, too late and the air bubbles will not flow out from between the photocathode and the Lucite when pressure is applied.

After gluing, the extension to the light guide was wrapped, and a magnetic shield was slipped over the PMT's extending several inches past the photocathode.

The ΔE's were also wrapped with a single layer of aluminum foil. They were inserted after the E-blocks had been constructed, and were held in place using the mylar that went between the inner E-blocks. The weight of the ΔE PMT's, bases, and additional magnetic shielding is born at each end by a metal cylinder which is attached mechanically to the clamps that went around the E-block light guides.

The Outer MWPC was then inserted into the cylinder, and slides in and out of the detector on two thin teflon tubes. Final alignment of the chamber was done using shims made from rohacell.

The endcaps were wrapped similarly to the cylinders, but an additional layer of aluminized mylar was needed for light tightness on the faces of all the counters. The endcaps are tightly packed around a central tube and held in place with two layers of strapping tape. The entire assembly rolls into the LADS detector on rails.

[†] Claudia Wigger, who is the most skilled in this process, describes the appropriate consistency as that of honey.

The inner MWPC, along with all of its cables is inserted into the middle of the detector when the rest of the detector is in place. Because of the great weight of the cables, the very small space the MWPC must fit into, and the fragility of the inner MWPC, its insertion and removal is extremely difficult. Though fraught with possible catastrophic risks to both MWPC's, it has been successfully done over a half dozen times, and incremental improvements in the procedure continue to reduce the risks.

2.8 Material Between the π-Nucleus Interaction Point and the Scintillator

To calculate the threshold for the detection of charged particles, and to determine the energy loss for the detected charged particles, it is important to know the amount and composition of the material between the interaction point and the scintillator. This is shown in Table 2.3.

2.9 LED monitoring system

Attached to every light guide of the entire detector was one or more temperature stabilized LED's. These were used extensively during the set up of the detector, as a check of the PMT's and the associated electronics. During the run, they were continuously pulsed at a low rate for monitoring purposes.

2.10 Electronics for the Readout of the Scintillator

All of the 280 PMT's used in the LADS detector itself have passive bases. These bases were designed to draw a maximum of 2.5 mA and were supplied by a Lecroy Multi-Channel High Voltage System 1440. Typical operating voltages vary by tube, but were typically in the range of 1300 to 1800 V. The voltages to each tube were computer controlled, set remotely, and monitored continuously during the experiment to ensure stability.

Material in LADS

Description	Composition (Density g/cm^3)	Thickness mg/cm^2	Notes
Target Gas	^{3}He, 95.0 bar at 32.0° C (10.83)	21.65	Thickness varies with vertex
Target			
Lining	Ag 10 μm	10.5	
Lining	Cu 20 μm	17.9	
Walls	C fiber, 3 layers, (1.784)	64.2	Total, for all 3 layers
Walls	epoxy, 3 layers, (1.5)	19.4	Total, for all 3 layers
Reinforced Regions	C fiber ≈ 0.7 mm thick	125	Most particles
Reinforced Regions	Epoxy ≈ 0.3 mm thick	45	not affected
			see Section 2.4
Air elevation 360 m	≈ 1017.5 hPa, 30.5° C (.00113)	28.4	Total air for cylinder particles
Inner MWPC			
Two grounding foils	Kapton, 25 μm (1.42)	7.1	
Two support cylinders	Rohacell $C_9O_2NH_{13}$ (.050)	20	Each 2 mm thick
Two cathode foils	Kapton ≈ 45 μm (1.42)	12.8	50 μm before scratching
Al Coating on Kapton	8 layers Al, 700 Å each	1.5	
Epoxy	Araldit, 4 layers	5	
MWPC Gas	Ar and C_2H_6	1	
Two epoxy beads	Araldit, ≈ 2 mm×2 mm (1.5)		Most particles not affected
ED Wrapping			
Al foil	Al 12 μm thick (2.7)	3.24	
Al Mylar	Mylar 25 μm thick	3.5	Ignore Al coating
Outer MWPC			
Two grounding foils	Kapton, 50 μm (1.42)	14.2	
Two support cylinders	Rohacell $C_9O_2NH_{13}$ (.050)	30	Each 3 mm thick
Two cathode foils	Kapton ≈ 45 μm (1.42)	12.8	50 μm before scratching
Al Coating on Kapton	8 layers Al, 700 A each	1.5	
Epoxy	Araldit, 4 layers	5	
MWPC Gas	Ar and C_2H_6	1.6	
Four epoxy beads	Araldit, ≈ 3 mm×3 mm (1.5)		Most particles not affected
CD Wrapping			
Al foil	Al 12 μm thick (2.7)	3.24	
Mylar support	Al Mylar, 20μm	.9	Only about 30% of CD covered.

Table 2.3: All thicknesses are given for a trajectory normal to the beam line.

The signals from the PMT's were processed almost identically. The signals from all the tubes were carried from the experimental area to the electronics shack via 100 ns cables of RG-52. For the 5″ PMT's, since the signal came from a dynode instead of an anode, it was converted from a positive pulse to a negative pulse with an inverting transformer. The pulses for all the classes of counters, except the CD's, ED's, and EV's, were then fed into ×10 fast amplifiers designed by PSI. This allowed the current drawn by a pulse in the PMT base to be a factor of 10 smaller. This improves the linearity of the PMT's for an environment of large dynamic ranges and high pulse rates.

All of the signals from the PMT's (via the fast amplifiers and inverting transformers where noted above) were then fed into fast constant fraction discriminators (PSI module FDMT 100's [45]). These Fastbus modules were built at PSI, and have special noise rejection circuitry to reject noise with frequencies ≤ 1 kHZ [46]. Each module is two slots wide, has 32-channels, and is operated with a threshold of ≈ 15 mV. At the input of the FDMT 100's, the signal is split. Part of the signal is sent to the constant fraction discriminator circuitry, and part is sent to an analog amplifier. The signal sent to the amplifier is given an amplification of ×0.3 or ×0.4, depending on the class of counters, and is split again so that there are two identical analog signals at the output of the FDMT. One of these analog signals was sent to the Lecroy Fera ADC's, the other was used for diagnostics.

The logic signal from the constant fraction discriminator is also duplicated, so that three logic signals are available at the output of the FDMT for later stages. One logic signal was sent to both a Phillips Scientific Fastbus TDC's Model 10C6 and also a Phillips Scientific Fastbus Latches Model 10C8. A second logic signal was sent to a programmable logic array built at PSI in the Fastbus standard. This programmable logic array was used to form the "physics" trigger and is described further in Section 2.4. A few channels of the logic signals from the third output went to scalers and other monitoring devices.

2.11 The πM1 Channel at PSI

The experiment was done at the πM1 Channel at PSI. This channel is shown in Figure 2-4 and further documentation can be found in references [47] and [48]. The channel design is point-to-point focusing. It uses two matched dipoles and nine quadrupole magnets. There is a 2 m long electrostatic separator at the entrance to the channel to remove protons, positrons, and muons. The pion beam momentum can be chosen by the experimenter at any value within the range of 150-450 MeV/c, and the momentum acceptance of the channel is 2.9%. Between the two dipoles, at the momentum focus, there is a 64 element scintillator hodoscope which measures the pion momentum. The channel is capable of producing relatively pure pion beams of $\approx 2 \times 10^7 \pi^+/s$. The pion beam is for practical purposes continuous, but with the nice feature that pions can come only at 20 ns intervals. This micro-structure is due to the structure of the proton beam provided by the cyclotron. Protons, which have been synchronized by the RF of the cyclotron, hit the pion production target nearly simultaneously once every 20 ns.

2.12 Beam Definition and Monitoring

Because the incident flux of pions from the beam line was usually kept less than $\approx 3 \times 10^6$ π^+/s, it was possible to monitor and count the beam with PMT's attached to scintillators which were placed directly in the beam. The S_{time} counter, a 3 mm thick scintillator counter with a radius of 6 cm, was placed at the entrance to LADS. Two light guides were attached to the edges of the scintillator, one on the top, the other on the bottom. These light guides were coupled to two Philips XP2020 PMT's, which had active, high performance bases designed at PSI and in common use there. In the analysis the mean time of these PMT's was used to define the time at which a pion entered LADS. The scintillator was 3 mm thick so that enough photons would be collected by the PMT's to obtain a good timing signal. For the runs analyzed, the average number of particles incident on S_{time} was $\leq 1.6 \times 10^6/s$, and typically $\approx 1.0 \times 10^6/s$.

There was a veto wall just in front of LADS. It was designed to reduce beam related background incident on the detector itself. It is large enough to shield the entire detector, and has a hole in it the size of S_{time} for the beam to pass through. It is made from plastic scintillator and read out with PMT tubes.

The S_{beam} counter was placed inside the inner MWPC, $\approx$ 35 cm from the entrance to the target cell. It was a 1 mm thick scintillator, with a radius of 1 cm and was attached to a Philips 1/2″ XP1911. The purpose of this counter was to count the number of pions incident on the target and to define a narrow beam centered on the target, which was much smaller than the radius of the target cell. For the runs analyzed, the average number of particles incident on S_{beam} was $\leq 1.8 \times 10^5/s$, and was typically $\approx 1.2 \times 10^5/s$.

To determine the shape of the beam, and for help during the beam tuning, a beam profile monitor supplied by PSI was used. The detection component of this profile monitor is an

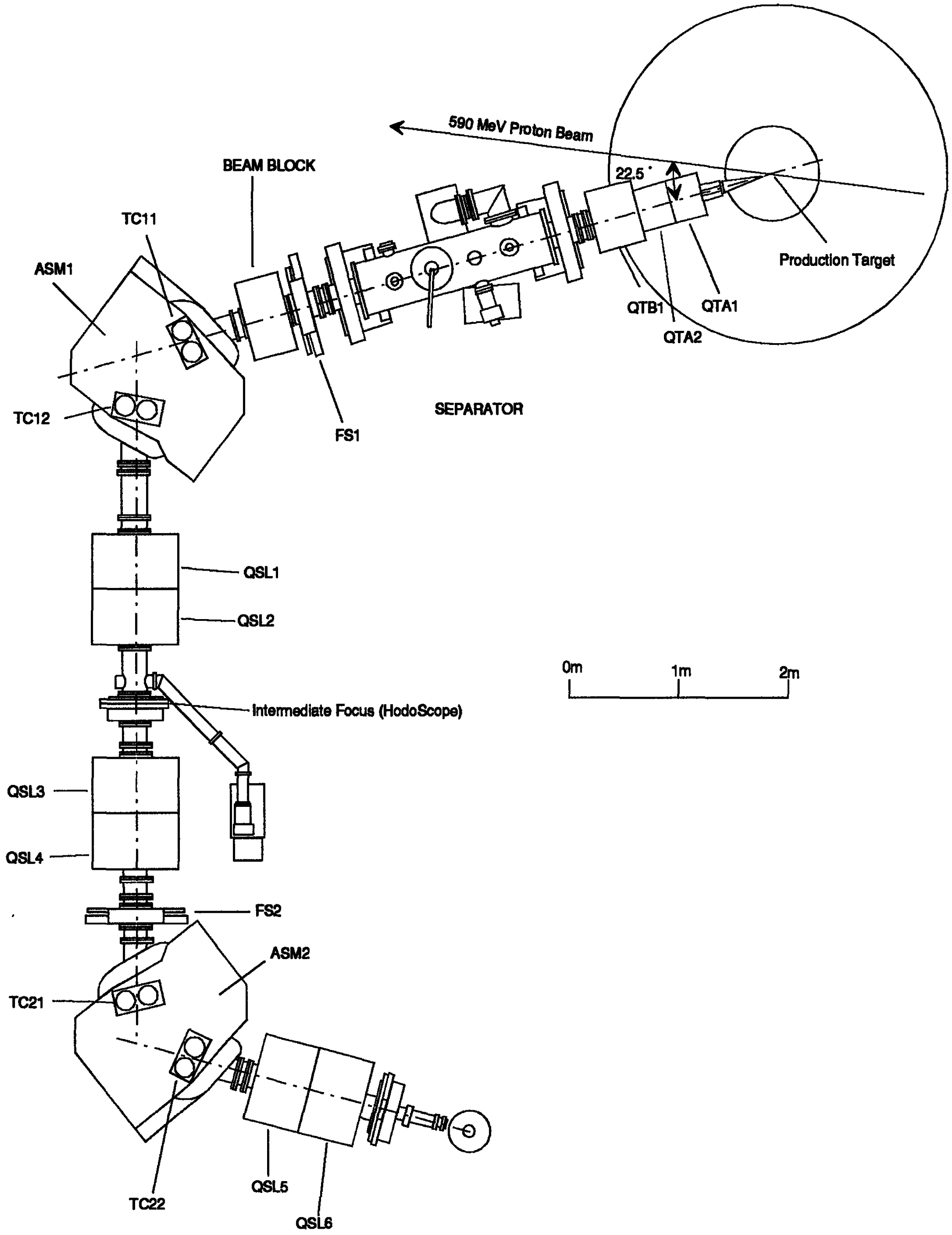

Figure 2-4: A scale drawing of the πM1 Channel at PSI.

MWPC which measures each beam particles horizontal and vertical position. The signals from this MWPC were integrated electronically and the results produced a real-time readout of the density of the beam in each of the two directions. The beam profile was displayed in the experimental shack which was where the pion beam was tuned and monitored.

The control room at PSI also supplied the electronics shack with the 50 MHz RF signal that is used in the cyclotron to produce the primary proton beam and thus determines the micro-structure of the secondary pion beam. This was fed into a very fast discriminator, which produced a logic signal which was 2-3 ns wide every 20 ns. Pions incident on LADS were in coincidence with the RF signal.

2.13 Triggers

A "trigger" will be defined in this work as a particular type of occurrence which is of interest to the experiment. For example, the most common trigger is the "Beam" trigger, which is used to signal that a pion is in the detector. There were a number of different triggers used in the experiment. Every trigger that occurred was recorded by the scalers, but only for a fraction of each trigger was the data of the entire detector (TDC's, ADC's, etc.) read out and recorded on tape. Prescalers on each trigger allowed the fraction written to tape of each trigger to be varied independently. An "analyzed" or "sampled" trigger, will be used to refer to a trigger which produced a readout of the detector.

The Beam trigger used the information from the beam monitors and scintillators described in Section 2.12 to indicate that there was a pion in the detector which fulfilled the further requirements described below.

At the output of the S_{time} PMT, two distinct types of signals in coincidence with the RF could be seen with an oscilloscope. One bright signal and one fainter but larger signal. The bright signal was pions, and the fainter, larger, signal was protons or two pions coming at the same time. To eliminate occurrences caused by two pions or a proton, a discriminator was set on the S_{time} PMT signal above the bright pion band, but below the fainter, two pion and proton bands. The output of this discriminator was named $S_{\text{time}}^{\text{big}}$, because it indicated when the S_{time} counter had a signal which was larger than the signal produced by a single pion.

Also seen at the output of the S_{time} PMT's were signals from positrons and muons that were not in coincidence with the pions, but arrived earlier [47] than the pions with respect to the

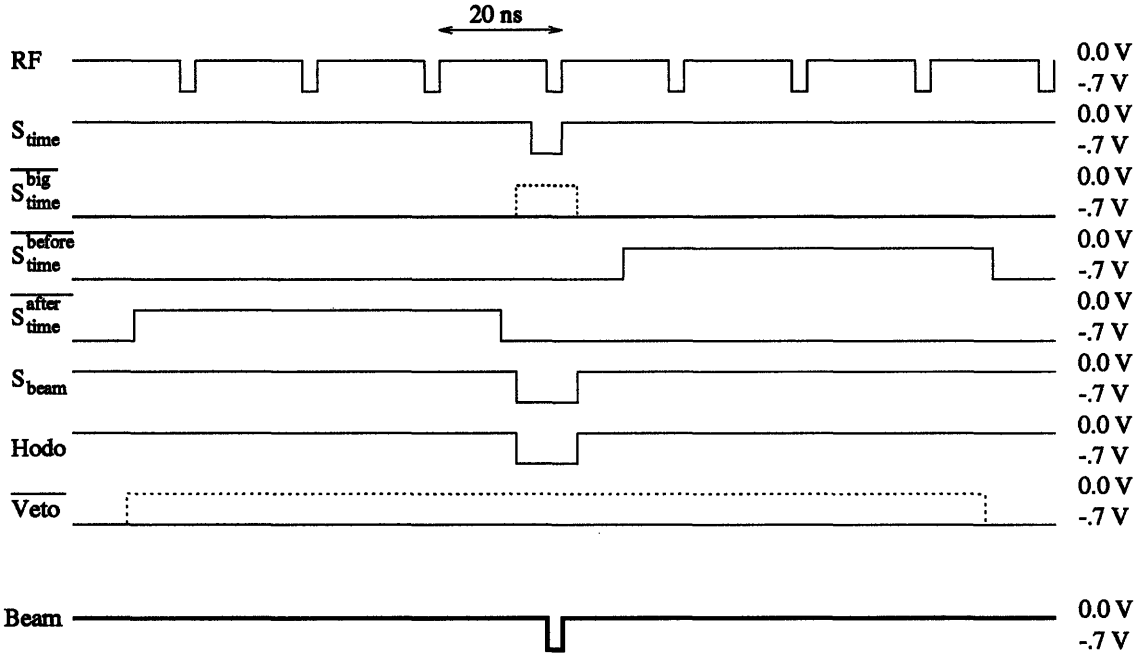

Figure 2-5: Diagram of the timing for the Beam trigger. 0 V is false, -0.7 V is true. The thin solid lines represents the input of an acceptable Beam trigger, while the dotted lines indicate the length of pulses not present for a good Beam trigger. The output of the Beam trigger, the thick solid line, is the logical AND of the input signals.

RF signal. A short, ≤ 5 ns, logic pulse generated from S_{time} was required to be in coincidence with the RF in order to eliminate the muon and positron contamination of the beam from the Beam trigger.

The amount of time that an event in the detector was considered "live" was about 50 ns, which was determined by the time it would take a slow (10-20 MeV) neutron to travel from the target and produce a signal in a CO counter. Accordingly, triggers were rejected when there was a particle from the beam in the detector within three beam bursts (60 ns) before or after the current pion. The occurrence of a charged particle in the previous or following three beam bursts was indicated by S_{time}^{before} and S_{time}^{after}, respectively.

A signal from the hodoscope at the momentum focus that indicated there had been a single or adjacent double hit was called HODO. A signal from the veto wall was labeled VETO.

A good Beam trigger was defined as:

$$\mathrm{Beam} = \mathrm{RF} \cdot \mathrm{S}_{\mathrm{time}} \cdot \overline{\mathrm{S}_{\mathrm{time}}^{\mathrm{big}}} \cdot \overline{\mathrm{S}_{\mathrm{time}}^{\mathrm{before}}} \cdot \overline{\mathrm{S}_{\mathrm{time}}^{\mathrm{after}}} \cdot \mathrm{S}_{\mathrm{beam}} \cdot \mathrm{HODO} \cdot \overline{\mathrm{VETO}}\,. \tag{2.8}$$

The timing of the Beam trigger was set up so that it was given by the RF signal, and the coincidence window from $\mathrm{S}_{\mathrm{time}}$ was ≤ 5 ns to eliminate muon and positron contamination. The Beam trigger was sent to a scaler (referred to as the "Beam scaler") and used in the experiment to determine the number of pions that could have caused a valid absorption reaction. A random sample of Beam triggers was also written to tape for use in the analysis as described in Section 4.4.

A "Physics" trigger is defined as a Beam trigger in coincidence with something detected by LADS. Physics triggers are divided into different types of triggers, based loosely on the number of charged and neutral particles in the detector. The number of charged particles in the detector is determined for the purposes of the trigger, by simply counting the number of cylinder and endcap ΔE's. If only one ΔE fires in coincidence with the Beam, it is denoted as a "1C" trigger. Two ΔE's are called a "2C" trigger, and events with three or more ΔE's are called a "3C" trigger.

The number of neutral particles is also counted. For the trigger, a neutral particle is defined as a CI or CO counter firing without the CD in front of it firing. Logically, for the i^{th} sector, a neutral in the cylinder is defined as:

$$\mathrm{N}_i = \overline{\mathrm{CD}}_i \cdot (\mathrm{CI}_i + \mathrm{CO}_i) \tag{2.9}$$

For the endcap, the definition of neutrals is complicated considerably by the offset of the ED sectors from the EI and EO sectors. ED_{i-1} and ED_i cover the i^{th} sector of the EI's and EO's. The definition of a neutral in the endcap was

$$\mathrm{N}_i = \Big(\overline{(\mathrm{ED}_i + \mathrm{ED}_{i-1})} + (\mathrm{EI}_{i-1} + \mathrm{EO}_{i-1})\Big) \cdot (\mathrm{EI}_i + \mathrm{EO}_i)\,. \tag{2.10}$$

After counting the number of charged and neutral particles using the above scheme, the following eight trigger types were formed in coincidence with the Beam trigger: 0C1N, 0C$\geq$ 2N, 1C0N, 1C1N, 1C$\geq$2N, 2C0N, 2C$\geq$ 1N, and $\geq$ 3C$\geq$ 0N and sent to the scalers. These triggers as a group are referred to as the Physics triggers, and as a set cover all of the possible charged and neutral multiplicities that could occur. For convenience, when the number of charged particles is referred to alone, it is inclusive of the possible neutrals, *eg.* the 2C trigger is the set consisting of the 2C0N and 2C$\geq$ 1N triggers. Also, the $\geq$ 3C$\geq$ 0N trigger type is referred to as the 3C trigger type, for short.

Different final states could be emphasized by varying this sampling fraction.

The prescalers determined the fraction written to tape for each of the eight types of Physics triggers. By adjusting these prescalers, different final states could be emphasized. For example, the 1C0N trigger type contained a large amount of elastically scattered pions. The LADS detector had no advantage over previous experiments for this type of data, so only a small fraction of the 1C triggers were written to tape. On the other hand, π^+ absorption events, where LADS does have an advantage over previous experiments, were usually in the 2C and 3C trigger types, so a large fraction of these events were written to tape.

These triggers only loosely select the number of particles of each type in the detector. One charged particle can look like two charged particles to the trigger if that charged particle goes through both an ED and a CD. Or, if a charged particle scatters into an adjacent sector, it can look like a charged particle and a neutral. This can all be sorted out in the later analysis, but it means that some fraction of each trigger type must be written to tape and analyzed for every reaction of interest. See also Section 4.3 for a discussion of the normalization of the experiment.

The electronics for the triggers were programmable logic arrays (modules PLB 300 and 301) built at PSI in the Fastbus standard. The FDMT 100 logic signals from one end of the cylinder and from each endcap counter were sent to a PLB 300 which applied the logic for each sector, determining if it had a charged particle, a neutral particle, or nothing at all. There were two PLB 301's, one for the charged particles and one for the neutral particles. The PLB 301's counted the number of charged (or neutral) particles and produced logical outputs indicating the presence of these multiplicities. These multiplicities were then used to form the eight Physics trigger types. The trigger electronics after the FDMT were relatively fast, being able to form the trigger signals in approximately 200 ns.

There were two other trigger types besides the Beam and Physics triggers. One was the LED trigger, which indicated that the LED's had fired and recorded a certain number of these events to tape. The other trigger was a Random trigger which, like its name, fired randomly. Its purpose was to track the non-beam-related background if necessary. It ended up not being used much in the later analysis.

2.14 Data Acquisition

The ADC's, MWPC read-out, and most of the scalers were in the CAMAC standard and connected to FASTBUS with a Struck FBD (STR-320) module. The TDC's, latches, and the rest of the scalers were in the FASTBUS standard. All of these units were read out with an Aleph Event Builder (AEB, STR-501) FASTBUS processor running OS-9 with Real-Time Fortran. Each event was approximately 600 bytes long, and these events were buffered by the AEB into blocks 50 events long and sent to a CHI (STR-330) FASTBUS processor. The CHI shipped the data through a DRQ-11 DMA interface directly to the memory of a μVAX 3600. The μVAX 3600 wrote the data to 8 mm, 2.5GBytes, Exabyte tapes. The average event rate was $\approx$ 200 events/s. Event rates of 340 events/s were achieved at a computer busy of 80%. The 1991 experimental run produced about 200 8 mm tapes.

Chapter 3

LADS's Analysis Tools

As described in the previous chapter, LADS is built from a large number of individual detectors. The software needed to calibrate, control, and transform the information provided by the numerous individual detectors into particles, tracks, and energies, and then to manipulate this information to extract the physics, is quite complex. Tens of thousands of man-hours were spent by the collaboration in the development of this software, and software development is still on-going. Nevertheless, by early 1993 the software was sufficiently developed so that the analysis of pion absorption on ^{2}H and ^{3}He, special cases since the final states of these reactions contain only protons, could proceed.

In this chapter, only a few of the many analysis tools will be described, and those only briefly. Included are topics which were felt to be particularly relevant to later chapters, or software worked on by the author. Many important aspects of the code, like how to use it, its structure, its conventions, and even the imaginative names of its various parts (like LADYBIRD, LARK, PEPSI, etc...) will by necessity be skipped entirely. The potpourri of topics chosen for inclusion in this chapter are: the coordinate systems used by LADS, the energy and timing calibration of the plastic scintillator components of the detector, how the signals from the many scintillator counters are grouped together into particles, how the MWPC information is transformed into "hits," and how the MWPC "hits" are used to determine the trajectories of the particles and the vertices of the events.

3.1 Coordinate Systems

There are three coordinate systems that will be useful at various times in later chapters, the detector coordinate system, the laboratory coordinate system, and the center-of-mass coordinate system. The detector and laboratory systems differ only by a spatial translation, while the laboratory and center-of-mass systems are related by a velocity boost. In each system, a right handed Cartesian coordinate system will be defined. When polar coordinates are used, θ is the polar angle with respect to the z-axis of the system and ϕ is the azimuthal angle around the z-axis, with ϕ measured starting from the x-axis of the Cartesian system.

The detector coordinate system is defined with respect to the detector. The z-axis of this system corresponds to the axis of cylindrical symmetry of the detector and points in the same direction as the incident pion beam momentum. The x-axis is in the horizontal direction, with the y-axis pointing up in the vertical direction. The origin of the detector is defined as being equidistant from the two endcaps; this position is 5 cm upstream from the middle of the long bars of scintillator that form the cylindrical part of LADS.

The laboratory coordinate system has axis parallel to those of the detector coordinate system, but its origin is defined to be at the vertex of the event.

The center-of-mass coordinate system is equivalent to the laboratory coordinate system, but boosted in velocity so that the center of mass of the system under study is at rest in this frame. The center-of-mass system for pion absorption on ^{2}H and for 2NA on ^{3}He is the π-^{2}H system; for 3NA on ^{3}He the center-of-mass system used is the π-^{3}He system.

3.2 Calibration

The energy calibration of the plastic scintillator was done using the $^2\mathrm{H}(\pi^+,pp)$ reaction. The angle of the protons measured using the MWPC's over-specified the final state, allowing the energy of each proton to be determined independent of the plastic scintillator. It was thus possible to use the protons from this reaction to calibrate the scintillator. This method used the scintillator saturation curve from References [49, 50], had corrections for energy lost in the dead material between the interaction point and the scintillator, and assumed that the photomultiplier tubes and their associated electronics had linear responses with respect to detected light. The resolution for the total energy deposited in the scintillator per event obtained upon using this calibration was 5-7% FWHM, which was sufficient for the integrated cross section measurements. The calibration of each counter was checked visually, to ensure that there were no large ($> 5 - 10\%$) non-linearities and to ensure that each counter was consistent with other counters of the same type.

By the time the analysis of the differential quantities was being done, a "fine calibration" procedure had been developed which used as its starting point the rough calibration above, but then took into account the non-linearities of each type of counter. This procedure was utilized in order to remove various non-linearities in the detector response. The $^3\mathrm{He}(\pi^+,ppp)$ reaction was used for this fine tuning of the energy calibration. Similar to the $^2\mathrm{H}(\pi^+,pp)$ reaction which was used for the initial calibration, the MWPC information alone is enough to determine the protons energies in the $^3\mathrm{He}(\pi^+,ppp)$ reaction, but this reaction has a much larger range of proton energies in its final state than the $^2\mathrm{H}(\pi^+,pp)$ reaction. This full range of proton energies in the final state allowed the fine calibration procedure to improve the energy resolution by making a non-linear fit to map the scintillator's energy response over the entire range of energies seen in the experiment. The resolution obtained for the total energy deposited in the scintillator improved to better than 5% FWHM, and most of the non-linearities of the individual counters were removed. This improvement is important because an accurate determination of the particle's energy is necessary to properly transform to the center-of-mass frame. Fine calibration was used in the production of all of the differential plots which appear in Chapter 6.

Improvements in methodology and software continue, and the energy resolution for the summed total energy obtained with these improvements is now less than 4% FWHM [51]. The best energy resolution obtainable with the LADS detector, assuming perfect calibration for all the sectors, can been estimated from tests done with a proton beam [43] to be slightly less than 3% FWHM for protons with 100 MeV of energy.

To obtain a timing calibration, the gains and offsets for each TDC needed to be measured. The gain of the TDC was determined during the setup of the experiment by using the LED's attached to each scintillator. Known lengths of coaxial cable were added and subtracted to the LED pulser and the difference between the peak positions for the various cable lengths was used to measure the gain of each TDC. The timing offsets were found by using scattered pions. The scattered pions traveled the distance to the scintillator quickly (typical flight times of 1-2 ns), so small uncertainties in the velocity or trajectory of the pion had little effect on the determination of the offset. This contrasts with the situation for that of heavier particles, such as protons and deuterons, which because of their lower velocities could take as long as 10-20 ns to reach the scintillator and thus would have introduced a greater uncertainty in the determination of the offsets.

A number of things can cause the offset of all of the TDC's to change by the same amount during the experiment. The overall offset changed significantly when the momentum of the pion beam was altered, because the amount of time the pions took to travel to the target changed. Also, small changes of as much as a few hundred picoseconds were seen between runs at the same beam energy. The change between adjacent runs was smaller, only approximately 100 picoseconds. A new run was started after 0.5 gigabytes of data had been written to tape, which usually took about an hour. The changes in the overall offset for the same pion momentum could have been caused by the delay cable's expanding or contracting with temperature, the proton beam's tune changing slightly, or other similar factors. Therefore, while the individual TDC offsets were determined at only a few intervals throughout the experiment, for example when equipment was changed or after the experiment had been shut down for a few weeks, an overall offset was determined for each experimental run. The overall offset was added or subtracted to the individual TDC offsets. The overall offset for the run could be determined by using the change in the peak position of the beam pions incident on the S_{beam} counter.

3.3 Building Particles

The experimenter is interested in the number of particles, their energy and trajectories, but the data is in the form of a multitude of digitized signals from individual detectors. Each of these detectors typically has a fraction of the information about a particular particle and the experimenter must deduce which particle the information goes with, and how many particles there were in the detector.

In LADS, the following steps were done to transform the information about the signals from the photomultiplier tubes into the number of particles, and the energy and identification of each particle. First, spurious signals needed to be rejected. Then, from the individual scintillator counters the number and approximate location of the particles in the detector needed to be deduced. Finally, the energy and timing information of each counter needed to be assigned to a particular particle so that the kinetic energy of the particle and its particle identification could be determined. This process, while often straightforward in detectors with only a few channels and with more favorable geometries, was difficult to perform with LADS until significant experience with the raw data had developed.

The information from each photomultiplier tube was recorded by ADC's, TDC's and latches. The scintillators which formed the cylindrical part of LADS were each connected to two PMT's, one at each end of these long bars. The scintillators which were used to make the endcaps were connected to only one PMT. Sometimes for a particular PMT, the ADC information would exist but there would be no TDC information, and vice versa.

ADC information without the corresponding TDC information was usually caused by an ADC pedestal drifting by a channel or two, or by a particle that was below the discriminator's threshold. For these cases, the information in the sector could safely be discarded; however, it was found that for two TDC channels, a bit was occasionally dropped in the address of the TDC and the TDC information was assigned to the wrong PMT. This problem developed in only two channels of a single TDC module. It was possible to fix this defect in the software by using the latch and ADC information to determine with which PMT the TDC information should be associated.

A channel that had TDC information without ADC information (which was rarer than the other way around) was usually caused by cross talk in the FDMT's or by a particle arriving so early or late that its signal fell outside of the ADC gate. Particles out of time with the ADC gate occurred in events that did not come from the target but came from particles reacting upstream in the S_{beam} counter or from other beam-related background. Events that came from the target region were reasonably clean.

For a scintillator counter to be considered to have valid information, it was required that there be recorded for that counter all of its ADC and TDC information. For the endcap counters that meant one ADC and one TDC; for the cylinder counters, two ADC's and two TDC's were necessary. The latches were not required, but were used only for diagnostic purposes. This procedure of removing counters from an event that lacked full information was termed "cleaning," and the data was checked to ensure that this procedure did not cause absorption events to be rejected (see also Section 5.7). The ϕ symmetry of the scintillator counters was examined to test for individual counters that were malfunctioning. Another test used ^{2}H absorption events that were separated out using only the ADC information; these events were checked for missing TDC's, and only a few out of thousands of absorption events were found with this problem. A similar check was done by using the MWPC to filter out ^{2}H absorption events and then looking for missing ADC's. These tests showed that no appreciable fraction of absorption events were lost during the cleaning procedure.

After the cleaning procedure, it was necessary to deduce the number of charged and neutral particles in the detector. Charged particles produced signals in the ΔE's, while a neutral particle would only very rarely produce a signal in the ΔE's. This relatively simple situation was complicated by two effects. First, for many trajectories a charged particle could go through both an endcap ΔE (ED) and a cylinder ΔE (CD). These "punchthroughs" were relatively common in the data analyzed because the trigger sampled more heavily events which fired more than one ΔE. Second, multiple scattering and reactions in the scintillator often caused charged particles to scatter into adjacent sectors, depositing some of their energy in those sectors. These "adjacencies" were considered to be neutral particles by the trigger, but if they were indeed caused by reactions or multiple scattering in the scintillator, they needed to be reclassified as part of a charged particle and their energy combined with the CD sector the particle went through. Otherwise, the multiplicity of the event would be incorrect and the amount of energy carried by the charged particle would be underestimated, which would have a number of deleterious effects. These two complications, punchthroughs and adjacencies, caused most of the difficulties in determining the number of charged and neutral particles that were in the detector.

The software first rebuilt the particles very naively using the cleaned data. It assumed that every ΔE that fired represented a charged particle, that every sector that did not have a ΔE present was caused by a neutral particle, and finally that particles did not cross from the endcap into the cylinder. After this initial step, flags set by the user determined whether more sophisticated rebuilding procedures were invoked. If the appropriate flag was set, the software would combine charged and neutral particles that were in adjacent sectors into a single charged particle. This procedure was relatively safe in the analysis of pion absorption on ^{2}H and ^{3}He, where the final state was unlikely to contain neutral particles*.

Appropriate flags could also signal the software to combine charged particles in the endcap with those in the cylinder, thus counting punchthroughs as one particle instead of two. This was done if two tests were satisfied: 1) the ED that fired overlapped, or nearly overlapped, the ϕ range that the cylinder covered, and 2) the CD timing difference, calculated using the two PMT's on the CD counter, indicated that the charged particle in the cylinder sector was in the

---

*Conservation of charge demands that there be no neutrons in the final state. It is possible to have γ's in the final state after pion absorption, but since this is caused by electromagnetic processes, it has a much smaller cross section than the strong processes being studied.

region covered by the endcap (either far upstream or downstream, depending on whether the ED was on the upstream or downstream endcap). The efficiency of this method could be tested with the outer MWPC, since it was active in the region between the endcap and the cylinder, and the information from the MWPC allowed the two parameters (how many cylinder sectors an ED "overlapped" and how much uncertainty was allowed in the z-position determined by the timing difference of the two PMT's) to be optimized.

Both of the more sophisticated procedures which were described and could be selected using software flags were used in the analysis.

While the MWPC was useful for testing the rebuilding procedure, information from it was not used to determine the multiplicity of an event. This choice was made primarily because the inefficiency of the MWPC might cause confusion in the reconstruction of an event, and because the efficiency of the MWPC and plastic scintillator would be difficult to measure accurately if the two were interdependent. Thus the scintillator's information was kept completely free of MWPC information. The MWPC information had some minor dependencies on the scintillator information, but this was kept to a minimum and only involved the final step of associating the hits on the inner and outer MWPC's with the particles formed by the scintillator. This dependence is described in Section 3.5.

3.4 Locating the Position of the Hits in the MWPC's

The MWPC information was presented in terms of wires that fired and cathode strip ADC data. The cathode ADC information needed to be separated into peaks and each peak's mean determined. Then the peaks on each of the two cathode planes on each chamber and the ϕ information from the anode wires were associated together so that the ϕ and z position of the charged particles' crossings of the MWPC could be determined. These crossings were called MWPC "hits."

The cathode ADC information was first cleaned by filling known dead strips by interpolating between their neighbors. The effects of noise on the individual strips was reduced by associating with each ADC value the median of its value and its two neighbors' values. Regions were located for which the medians were above threshold. Since charged particles typically produced a peak four strips wide, a region above threshold could have more than one peak. These regions were therefore separated into more than one peak whenever the region above threshold contained a median value for a strip which was 75% or less of the median values of any of the strips located on either side of it within the region. Some events had a large amount of low level noise which produced a large number of false peaks. To eliminate this noise, if more than five peaks were found on a cathode plane the threshold was increased and the peak search procedure was repeated. This technique was effective in eliminating the noise present for some of the events although it artificially limited the number of charged particles in the final state to five or less. Such a limitation is not a problem for light nuclei. After each peak was identified, its centroid was calculated using the raw ADC values, not the medians which were used only to delimit the peaks.

It was then necessary to associate the peaks on each cathode plane with the peaks on the opposite cathode plane of the same MWPC. This association was done by calculating the ϕ and z position of every possible permutation of peak associations. The permutation which had the most ϕ matches with the ϕ's reported by the anode wires was chosen. If more than one set of permutations had the maximum number of anode matches, the integrated ADC values of the cathodes were used to choose between these permutations, since a charged particle typically left similarly sized signals on both planes of a chamber.

3.5 Associating MWPC Hits with Particles and Forming Tracks

In the above sections, it was described how particles were defined using the information from the plastic scintillator and how the hits on both the inner and outer wire chambers were determined. After ascertaining this information it was then necessary to associate the hits of the two MWPC's with particles and form the particles' trajectories ("tracks") from the measurement of two points along the particles trajectory. Associating MWPC hits with particles was complicated because cathode pairs that were associated with each other but which lacked anode information[†] usually had two possible crossings.

The first step was to match outer chamber hits with cylinder ΔE's which fired. The ϕ and z of the MWPC hit were compared with the ϕ given by the middle of the ΔE and the z

---

[†] The anode planes were only 70-80% efficient, while the cathode planes were nearly 100% efficient. As a result, cathode pairs without an associated anode were not uncommon.

calculated from the timing difference of the two PMT's on the ΔE. If the ϕ's matched to within $\pm 11°$ and the z's were within ± 30 cm, the MWPC and ΔE were considered to be a possible match. Initially assigned as a definite match were MWPC hits which only had one possible match. Other possible matches were then assigned, giving preference to hits with associated wires. Finally, pairings between particles which did not fire a cylinder ΔE (and were thus considered to be a neutral particle) and the outer MWPC were matched. This uncommon occurrence was caused primarily by gaps between the CD sectors. To determine whether the gaps in the CD's were a significant problem, the ^{2}H(π^+,pp) reaction was used. The sharp summed-energy peak that is the signature of this reaction was used to isolate absorption events in the 1C1N and 1C2N triggers, because it was in these triggers that an absorption event in which a proton slipped through the gap in the ΔE's would appear. The handful of events that appeared within the summed energy cut were looked at individually. In general, these events lacked the back-to-back nature which is characteristic of the ^{2}H(π^+,pp) reaction, but instead looked like pions that absorbed in the scintillator. Thus, the amount of absorption cross section found in these triggers was less than 1%, which was ignorable.

The next step was to match the inner MWPC hits with particles determined using the plastic information. This matching was done by looking for inner MWPC hits that were within $\pm 14°$ of an assigned outer chamber hit. The code then looped over all possible associations trying to find a vertex, *i.e.* two tracks which passed within 1 cm of each other. If a vertex was found, it was a very powerful tool for untangling the other possible MWPC associations because other inner and outer MWPC hits should point back to the events vertex. If no vertex could be found, then the most reliable inner and outer MWPC association (as judged by a "one and only one association" and differences between the ϕ's on the two chambers, smaller being better) was used to find a crossing with the beam axis. This beam axis crossing was used in a manner similar to that used with the vertex and helped to disentangle the other associations.

After the inner and outer MWPC's were associated, leftover inner MWPC hits were associated with endcap ΔE's and cylinder ΔE's which did not have an outer MWPC associated with them. When available, a vertex or a z-axis crossing was used to more reliably make associations. Some possible matches of inner MWPC hits with ΔE's could be ruled out because the trajectory described by connecting the inner MWPC hit and vertex or z-axis crossing did not point in the direction of the ΔE.

After the MWPC hits were assigned to specific particles, the ϕ_{lab} and θ_{lab} of the particles were calculated. For particles with both an inner and an outer chamber hit, ϕ_{lab} and θ_{lab} were calculated using the chamber information. Then for those events with two or more tracks, the vertex of the event was found by looking for tracks which came within 1 cm of each other and choosing as the vertex the point midway between the two tracks. If tracks which came within 1 cm of each other were not found, or if only one particle had two MWPC hits, then one track was used (chosen randomly in the cases where there was more than one track) and the vertex of the event was assigned to the point on that track which was closest to the beam axis. After a vertex for an event was determined, it was used as another point along the particle's trajectory and thus made it possible to calculate ϕ_{lab} and θ_{lab} for particles which had only one MWPC hit.

Sections 4.1.1, 4.3.2, 5.1.1, and 5.3.2 discuss the overall performance of the hardware and software in associating MWPC hits with particles as well as calculating vertices and ϕ_{lab} and θ_{lab} information.

Chapter 4

Data Analysis

The data on tape contains many different pion reaction channels with events originating both in the target and in other material in the path of the pion beam. Many steps were necessary to isolate the pion absorption events and calculate total absorption cross sections. After these steps were completed, LADS's large acceptance and its ability to measure the angles and energies of particles allowed many differential and kinematic quantities to be examined. The steps that needed to be done were: determining those events which came from the target; separating the pion absorption events from other processes; making corrections for reactions of outgoing protons in the scintillator, wire chamber inefficiencies, computer dead time and prescale factors; and determining the number of incident pions, the target thickness, and the acceptance of the detector.

The events originating in the target were isolated by using the information provided by the MWPC's in LADS and by doing empty target subtraction. This procedure was necessary since other material in the beam (such as the target windows and walls, S_{beam}, and the air inside the detector) accounted for a substantial fraction of the events written to tape.

The "absorption yield" is the number of times an absorption event occurred, during an experimental run, that was both in the target region defined with the MWPC and from a beam particle that had appropriate ADC and TDC information in S_{beam}. The absorption yield was measured by determining from the data collected on tape the fraction of absorption events in each physics trigger that satisfied the target and beam criterion. The total number of each physics trigger as measured by the scalers was then multiplied by this fraction to determine the absorption yield contained in that trigger type.

The absorption events written to tape needed to be separated from those events which came from other pion reaction channels. This discrimination was done using the features inherent to pion absorption in combination with charged particle cuts, particle identification cuts, and a total energy cut.

The cuts that eliminated non-pion absorption processes also cut some number of absorption events due to reactions in the scintillator and wire chamber inefficiencies. The number of absorption events cut was quantified with a variety of techniques which typically used one component of the detector and a pion reaction on a particular target to measure the inefficiency of another component of the detector, and vice versa.

To determine the number of pions on the target, the "Beam" scaler described in Section 2.13 was corrected for those counts that were not caused by a pion on the target. Some of these processes were: pion decay, multiple scattering, muon contamination, and beam particles that had unusual TDC information in the S_{beam} scintillator.

Because pure gas targets were used for all of the data taken, the density and length of the target were straightforward to measure. Each target gas's density was calculated from its factor of compressibility and the measured pressure and temperature. The effective length of the target was determined by a cut on the z axis using the multi-wire proportional chambers.

The geometric and momentum acceptance of the detector were calculated using a Monte Carlo code, and some assumptions were necessary to extrapolate over the unmeasured regions of phase space.

This chapter will describe the procedures that were used to calculate the total π^+ absorption cross sections at 118, 162, and 238 MeV on ^{2}H and ^{3}He from the raw data. This analysis provided sets of absorption data which are used for subsequent analysis.

4.1 Isolating Events Occurring in the Target

4.1.1 Using the Wire Chambers to Select Events Originating in the Target

Many of the events written to tape did not come from the target gas (see Figure 4-1a). To ascertain which events came from the target, it was necessary to find where the interaction occurred, or in other words the vertex of the event. The vertex was calculated from the information provided by the two cylindrical MWPC's. The MWPC's measured the coordinates ϕ and z at the point of intersection of the particle's trajectory with the cylindrical chamber. For particles detected by both wire chambers, one may define a line in space which will be referred to as a "track." This track has coordinates ϕ_{lab} and θ_{lab} which are in the coordinate system having its origin at the point of the π-nucleus interaction. (See Section 3.1 for further information on the coordinate systems used).

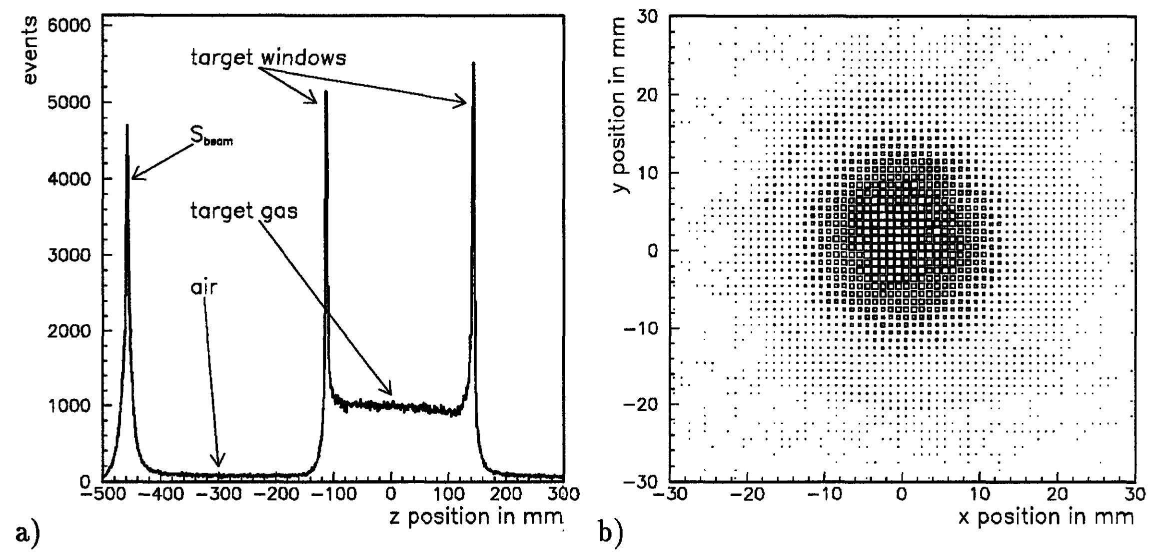

Figure 4-1: a) z projection of the filled target. b) x-y projection of the filled target after a cut has been made in z on the center 20 cm of the target.

The vertex of an event could be determined if the event had at least one track. For events with only one track, the vertex was calculated to be on the track at the point where it passed closest to the beam axis. For multiple-track events in which two of the tracks passed within 1 cm of each other, the vertex was chosen between those two tracks at their point of closest approach. When no track passed within 1 cm of the other tracks one track was randomly chosen to determine the vertex. This occurred at a frequency in the range of 2–4 % depending on the number of particles in the final state.

For events with only one track, the resolution of the vertex along the z direction was given by the beam's width, which was $\sigma \approx 0.8$cm (see Figure 4-1b). Since the angle of these tracks with respect to the beam varied between 40° and 140°, the z resolution of the vertex for an event with only one track was $\sigma \approx 0.8\text{cm}/\sin(40^\circ) = 1.25$ cm.

Figure 4-2 illustrates the resolution in space of the vertex for events with two tracks. The full-width, half-maximum (FWHM) of the distance at closest approach for two tracks was 2 mm. Since the vertex point lies halfway between the two tracks, the vertex resolution (FWHM) for two track events is 1 mm, half of the FWHM of the distance at closest approach. Therefore, the resolution of the vertex in each of the x, y and z directions is approximately $0.5\ \text{mm}/\sqrt{3}$.

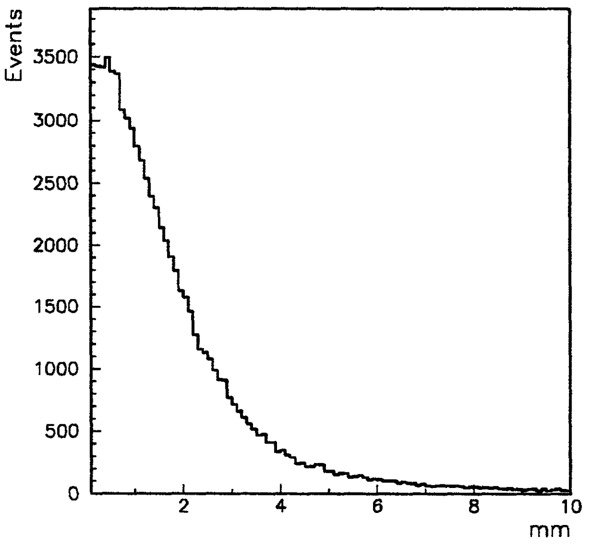

Figure 4-2: Distance, at the point of closest approach, between the two tracks in an event which define the vertex.

The following cuts were applied to isolate events which came from the target. First, events that did not have at least one track, and thus a well defined z-value, were rejected. Second, it was demanded that at least one of the tracks should not hit an endcap, since for some trajectories a particle with sufficient kinetic energy could pass through part of an endcap before it encountered the outer MWPC. Events that had only tracks that impinged on endcaps are difficult to model and include in the acceptance Monte Carlo code (see Section 4.6.1 for details) because of their strong dependence on both the intial energy of the particle and the amount of endcap material the particle traversed. Third, a cut was applied on the z-component of each event's vertex in order to remove events which did not come from the central 20 cm of the 25.5-cm-long target.

Energy (MeV)	Target	Trigger Type					Weighted Average
		2C0N	2C≥1N	3C≥0N			
		2 protons	2 protons	2 protons	3 protons	4 protons	
118	^{2}H	10%	15%	7%	75%	–	12%
162	^{2}H	5%	7%	4%	62%	–	7%
239	^{2}H	3%	4%	3%	53%	–	5%
118	^{3}He	11%	17%	8%	8%	45%	11%
162	^{3}He	6%	8%	5%	5%	31%	6%
239	^{3}He	3%	4%	3%	4%	24%	4%

Table 4.1: This is the size of the empty target background after all cuts to isolate pion absorption have been applied, displayed by trigger type and number of protons above threshold. The weighted average represents the size of the empty target subtraction on the total absorption cross section.

4.1.2 Empty Target Subtraction

No cut was applied to the radial coordinate of the vertex; there are several reasons for this choice. For events that had only one track, there was little additional information about the vertex's radial position, since the vertex's position was presumed to be at the closest approach to the beam's axis, and the accuracy of this assumption was determined by the beam's width. Therefore, for a meaningful cut to be applied to the radius, the data would have had to be restricted to only those events whose vertex had been calculated from two tracks. This restriction would have had at least two undesirable effects. First, it would have reduced the acceptance of the detector by $\sim$ 25% for absorption reactions in the target that had only two energetic protons and thus increased the error in the model-dependent extrapolations. Second, because the defined radius of the target would have been reduced, a much larger (and thus less accurate) correction for those pions which miss the target would have been required. (See Section 4.4.)

Instead of a radius cut, data on empty targets was used to subtract out the background produced by the target walls and air outside of the target. This subtraction of target wall background was done by analyzing both the empty and full target runs with the same cuts, normalizing the results with respect to the number of incoming pions, and then subtracting the empty target runs from the full target runs for each class of event. (See equation 4.7.) The size of this subtraction can be seen in the weighted average column of Table 4.1.

4.2 Isolating Pion Absorption

4.2.1 Requirement of at Least Two Charged Particles

After eliminating those events which did not come from pion reactions on the target nuclei, the next step was to isolate the absorption channel from the other reaction channels. The strongly interacting part (electromagnetic and weak channels will be ignored as insignificant) of the total pion nucleus cross section is composed at these energies of the following channels:

$$\sigma = \sigma_{el} + \sigma_{inel} + \sigma_{abs} + \sigma_{SCX} + \sigma_{DCX} + \sigma_{2\pi} \, , \tag{4.1}$$

where

σ_{el} = pion elastic scattering,
σ_{inel} = pion inelastic scattering,
σ_{abs} = pion absorption,
σ_{SCX} = pion single charge exchange,
σ_{DCX} = pion double charge exchange, and
$\sigma_{2\pi}$ = final states with two pions.

These channels are differentiated from each other by the types of particles that are present in the final state. The pion absorption channel is different from the other pion reaction channels in that it alone has only nucleons in the final state. In addition, the dominant pion absorption mechanisms have at least two energetic nucleons in the final state; this fact arises because single-nucleon absorption in a nucleus is strongly suppressed by the requirements of energy and momentum conservation and therefore makes a negligible contribution to the absorption cross section. Indeed, in absorption on the light nuclei ^{2}H and ^{3}He, energy and momentum conservation demand that there be at least two energetic nucleons in the final state because the recoil "nucleus" has the same or twice the mass as the ejected particle and thus is quite energetic. ^{2}H and ^{3}He each have only one neutron, so in π^+ absorption, all of the nucleons in the final state are protons. To isolate pion absorption events and because of the above conditions, it was required that all events have at least two charged particles above threshold in the final state. (See Section 4.3.3.1 for the threshold definition and Section 3.3 for an explanation of how charged and neutral particles were reconstructed and counted).

Two identifying characteristics of charged particles were employed to ensure a clean separation between charged and neutral particles. The first requirement for a particle to be counted as charged was that it caused a signal in one of the thin scintillators. The second requirement was that the particle had to have at least one MWPC hit associated with it. Therefore, events in which each "charged" particle did not have at least one MWPC hit were rejected. The reason for this rejection is that the MWPC was needed for the calculation of θ_{lab}, which is of particular importance for charged particle identification. Charged particle identification requires either an accurate determination of the particle's path length through the thin scintillator or the distance the particle has traveled from the interaction point, both of which depend on an accurate measurement of θ_{lab}. In the case in which a particle had only one MWPC hit, the particle's θ_{lab} and ϕ_{lab} could be calculated using the event's vertex and the particle's one wire chamber hit. When a particle had two MWPC hits, θ_{lab} and ϕ_{lab} were uniquely specified and the additional information from the vertex was ignored.

4.2.2 Particle Identification Cuts

Neutral pions decay almost instantaneously into two gammas, whereas charged pions have a half life of 26 ns. Twenty-six ns is much longer than the 1-5 ns flight time which was typical for pions between the point of interaction and the detector. When a charged pion does decay, 99.99% of the time it decays via $\pi^{\pm} \rightarrow \mu^{\pm} + \nu_{\mu}$. In these experiments the ν_{μ} went undetected, while the μ looked like a charged pion to LADS, as its mass and velocity were close to the mass and velocity of the pion from which it decayed. All of the reaction channels in Equation 4.1 other than pion absorption have either a charged or neutral pion in the final state. For this reason, those events in which a pion or gamma was detected in the final state were rejected by employing a series of particle identification tests.

The charged particle identification was based on both dE/dx vs. E and $1/\beta$ vs. E. The dE/dx for charged particles which are heavy compared to the electron mass is given by the Bethe-Bloch equation [4] and is a function of the particle's β and charge. For particles with $\beta > 1/137$, dE/dx initially falls off as $1/\beta^2$ until it reaches a broad minimum at $\gamma \approx 3.2$. In this experiment, only energetic pions had β values that were large enough to begin to approach this minimum. The dE/dx of the protons and deuterons was $\approx 1/\beta^y$ where y was between one and two. Therefore the two particle identification methods are mathematically very similar. E is the kinetic energy of the particle:

$$E + m = \gamma m \tag{4.2}$$

$$E = (\gamma - 1)m \tag{4.3}$$

$$\gamma \equiv \left(\frac{1}{\sqrt{1-\beta^2}}\right) . \tag{4.4}$$

For both methods, the pions, protons and deuterons will lie in bands according to their mass.

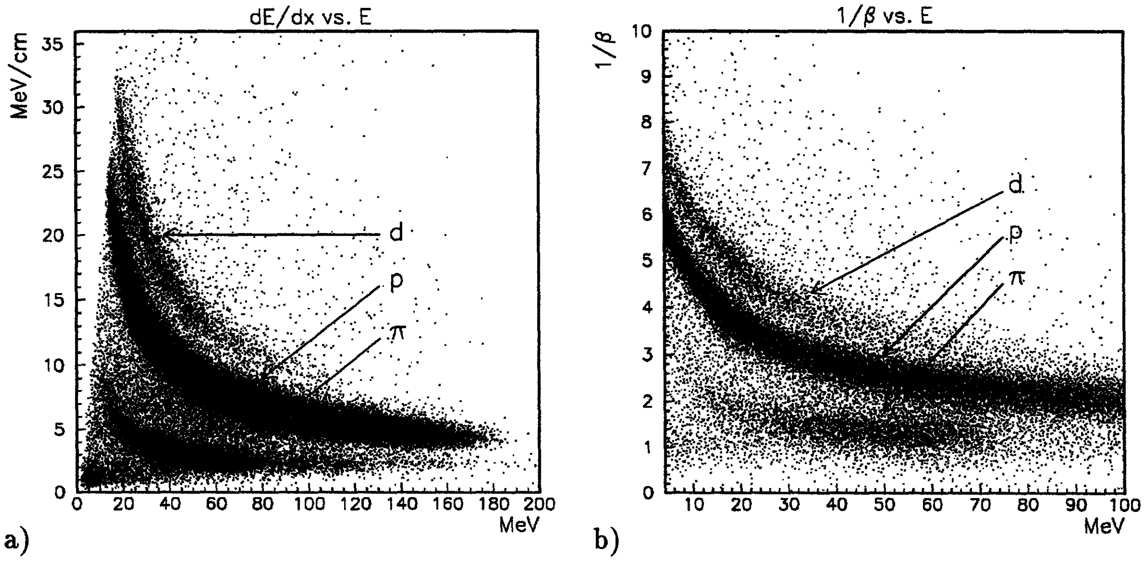

Figure 4-3: a)dE/dx vs. E for particles that are in the cylinder. b) $1/\beta$ vs. E for low energy particles in the cylinder. These graphs are after the target and charged particle cuts.

In the dE/dx vs. E method, the quantity dE/dx was determined by dividing the light deposited in a particular scintillator counter (such as a CD or CO counter) by the path length traveled in that counter. The path length was in turn calculated from the particle's angle of incidence on the counter as determined by the MWPC's and from the thickness of the scintillator counter. This method required the particle to pass through at least one counter of the scintillator; otherwise it would be incorrect to use the full thickness of the scintillator, as the path length could not be ascertained.

In the $1/\beta$ vs. E method, the trajectory of the particle was calculated using the wire chambers, and the time of flight was calculated using the beam timing scintillator (yielding the start) and the timing information from a scintillator counter (for the stop). The flight time for the final state particle was corrected for the pion flight time to the interaction point and divided by the distance from the interaction point to the scintillator. Unlike the dE/dx vs. E method, this method could be used for particles that did not go through a scintillator counter.

The energy for both methods was calculated using the calibrated light from the scintillators without energy-loss or saturation corrections. Those corrections could not be incorporated since they depend, of course, on knowing the particle's mass. The energy used in the dE/dx vs. E method was the energy deposited in the counter used for the dE/dx calculation and the subsequent counters that the particle entered. In the $1/\beta$ vs. E method, the energy used was the total energy of the particle deposited in all of the scintillator counters.

These two methods were used for particles that hit the cylinder, the endcap, or both. Because the relative accuracy of the two methods varied with the particle's energy, the following hierarchy decided which method was used on each particle to identify pions in the final state and eliminate events containing them.

a) For those charged particles which deposited at least 10 MeV of light in a CI counter, the pion cut shown in Figure 4-4a was applied.

b) If the condition in a) was not satisfied but the particle deposited at least 10 MeV of light in the sum of EI and EO, then the endcap dE/dx pion cut shown in Figure 4-4b was applied.

c) If neither of the above conditions was satisfied but the particle hit the thin scintillator in the endcap, then the endcap $1/\beta$ vs. E pion cut shown in Figure 4-4c was applied.

d) If none of the above conditions was satisfied then the cylinder $1/\beta$ vs. E pion cut in Figure 4-4d was used.

Even after cutting out events identified by the above hierarchy as having a pion, some pion contamination still remained. This contamination was concentrated in the region of particles with high incident kinetic energy. Further cuts, when applicable to a particular particle, were then applied as follows:

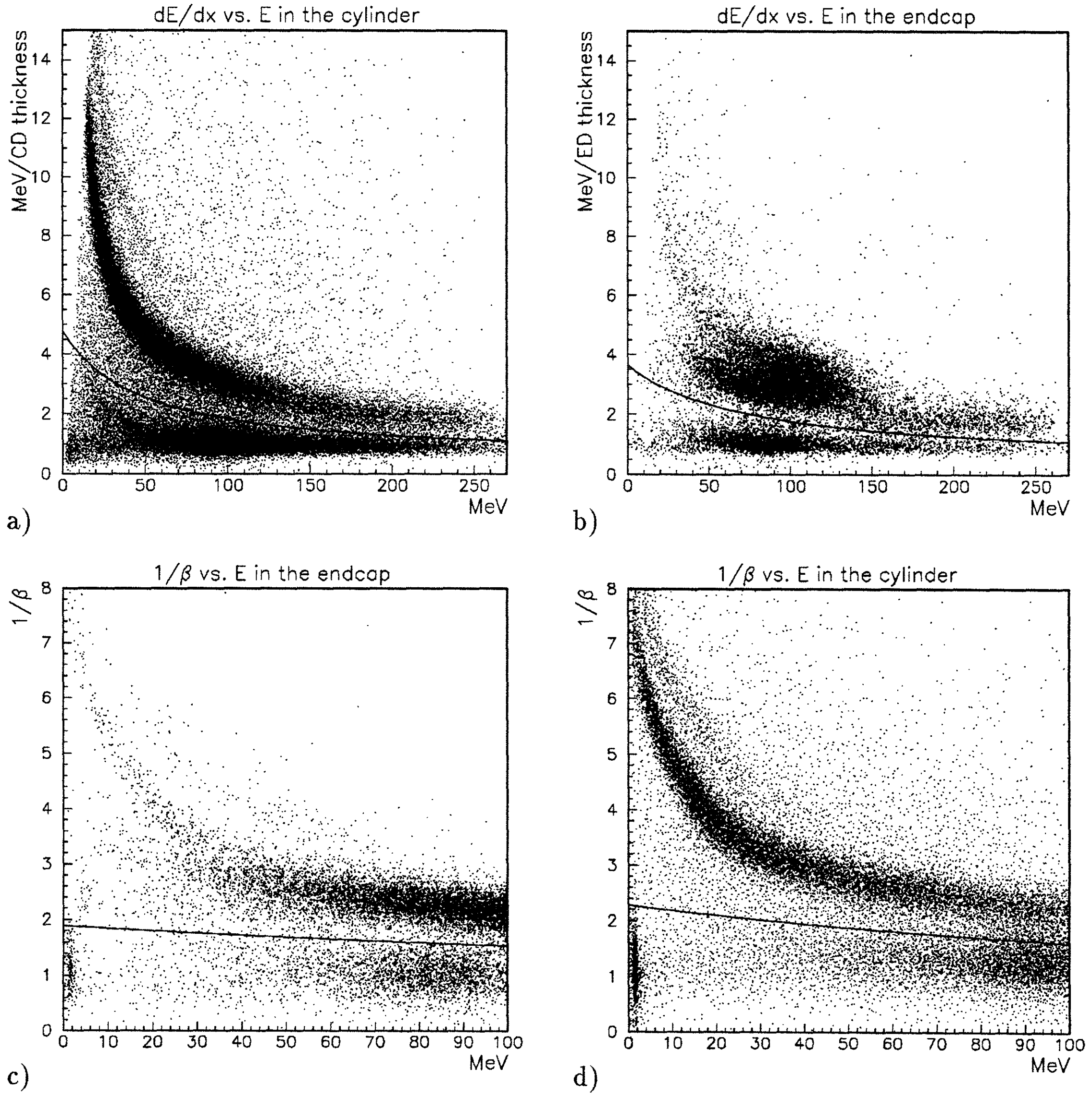

Figure 4-4: Events with particles below the solid line are cut if the method is used.

1) A cut was made on $1/\beta$ as measured by each counter in the cylinder, the CD, CI, and CO. This cut was kept well below the $1/\beta$ of the highest energy protons.

2) A cut was made for those particles which went through the CI and into the CO based on the dE/dx calculated using the CI counter (see Figure 4-5). This cut was limited to particles that fired no adjacent CI counters in order to ensure that the energy-loss and path length were well measured.

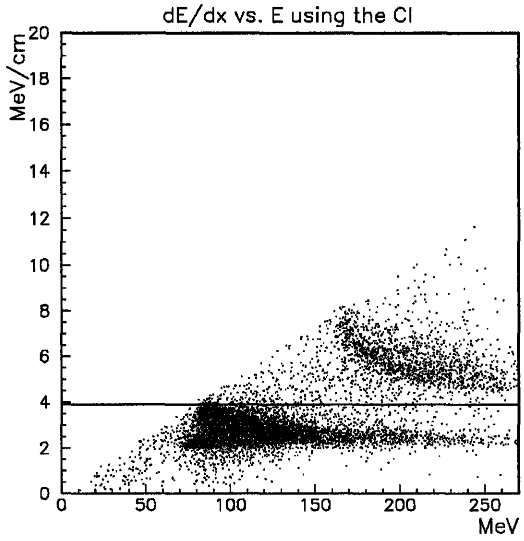

Figure 4-5: dE/dx was calculated from the energy deposited in the CI counter for particles that went through a CI counter and into a CO counter.

At this point, nearly all of the charged pions had been eliminated, but there remained a significant contamination from single charge exchange. This contamination could be reduced with a cut on the $1/\beta$ of neutral particles in the cylinder to eliminate some of the gammas produced in π^0 decay. $1/\beta$ was calculated from the particle's time of flight and the path length from the vertex to the point of interaction in the scintillator. The position of the particle in the scintillator was found from the timing difference of the two PMT's located on each counter. Because the gamma could convert anywhere along the thickness of the scintillator counter, the path length was not very well determined. In nuclei heavier than ^{3}He, this cut would have had to distinguish between neutrons from absorption and gamma rays. However, in this case there are no neutrons from absorption from the target gas. The "neutrons" seen in Figure 4-6 with

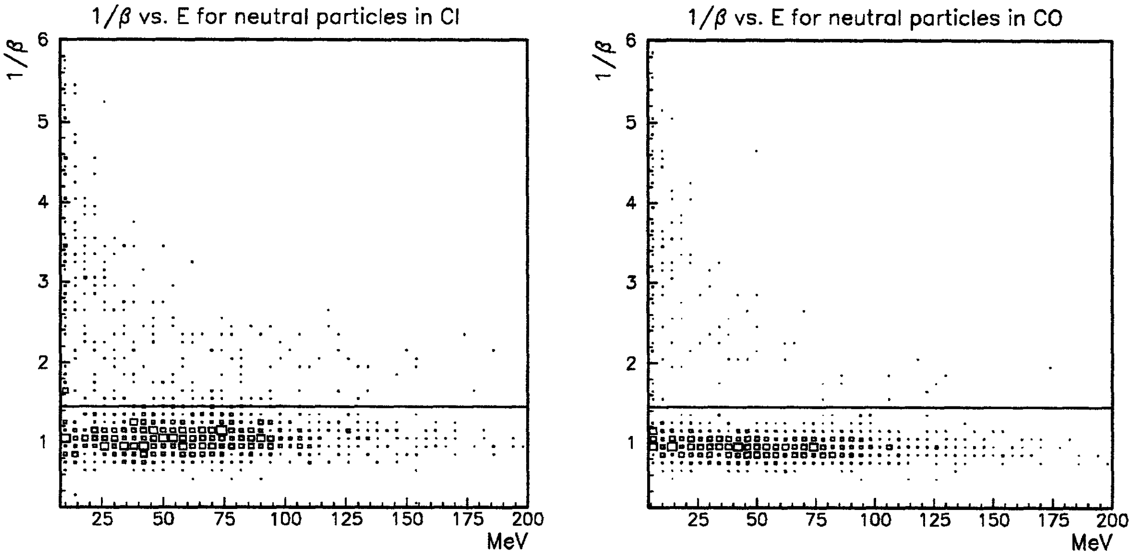

Figure 4-6: $1/\beta$ vs E for neutral particles in the CI and CO counters, after pion cuts, but before energy cuts and target subtraction. The target is ^{3}He with T_π = 239 MeV.

a $1/\beta$ much greater than two are either scattered reaction products or else neutrons from the target walls.

This $1/\beta$ cut on neutral particles greatly reduced the single charge exchange contamination of the cross section. However, since LADS does not always detect the gammas from the π^0 decay, some single charge exchange events still remained.

4.2.3 Total Energy Cut

Events that had passed the target and particle identification cuts described above still contained some contamination from reaction processes other than pion absorption. This residual contamination exists because the particle identification cuts were intentionally kept loose, so that few absorption events would be lost because of misidentification of final state particles caused by nuclear reactions in the scintillator. (See Section 4.3.1). The remaining events from non-absorption reactions were removed with an energy cut applied to the sum of the charged particle energies.

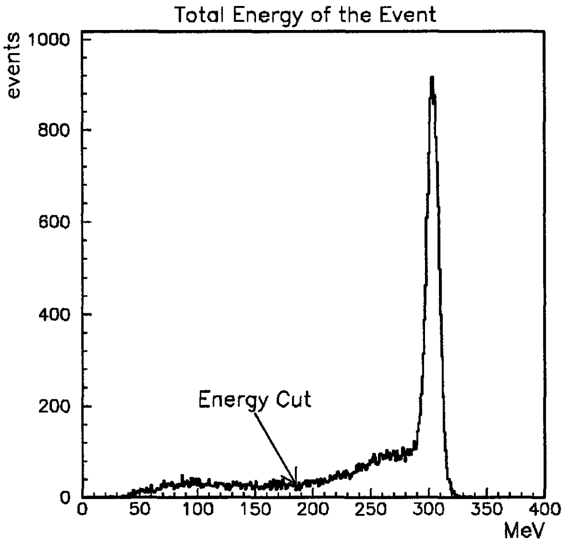

Figure 4-7: Sum of the charged particle kinetic energy for ^{2}H with incident π^+ at 162 MeV.

In π^+ absorption on ^{2}H and ^{3}He, conservation of charge demands that there be only protons in the final state. Furthermore, since the pion's mass is converted to kinetic energy, the sum of the final state nucleon's kinetic energies is $\approx$ 139 MeV greater than the sum of the kinetic energies of the pion and nucleons in non-absorption pion reactions. In the non-absorption reactions, the total kinetic energy is limited to the pion's incident kinetic energy. Using this fact, a total energy cut was placed on the sum of the charged particle energies approximately 20-30 MeV above the incident pion kinetic energy.

After this final cut, the amount of non-absorption events remaining in the data was quantified by looking at the CM opening angles between the two charged particles in ^{2}H runs (see section 5.2). The pion contamination was found to be 0.3%, 1.6%, and 3.9% of the total absorption cross section for incident pion energies of 118, 162 and 239 MeV respectively. The contamination was due to final state pions absorbing in the scintillator, thereby looking like high energy protons. The percentage of contamination in the analyzed triggers in ^{3}He was estimated from the contamination in ^{2}H using the ratio of absorption to quasi-free πp scattering in the two nuclei (see Table 4.2 and Section 5.2). The increased uncertainty of this extrapolation was taken into account in the systematic errors.

Energy (MeV)	Target	Trigger Type 2C0N	 2C≥1N	 3C≥0N	Weighted Average
118	^{2}H	0.0%	2.0%	0.3%	0.2%
162	^{2}H	1.1%	3.9%	1.0%	1.6%
239	^{2}H	1.6%	10.0%	3.3%	4.0%
118	^{3}He	0.0%	1.4%	0.2%	0.2%
162	^{3}He	0.6%	2.2%	0.6%	0.9%
239	^{3}He	1.3%	8.3%	2.7%	3.3%

Table 4.2: Pion contamination in each trigger type. The ^{3}He numbers are estimated from ^{2}H.

4.3 Determining the Absorption Yield Produced by the Target and Detected by LADS

The "absorption yield" is the number of times a pion passing the beam cuts in Section 4.4 absorbed on a target nucleus in the central 20 cm of the target region during the experimental run being analyzed.

Because of computer dead time and prescale factors, the data on tape represented a random selection of the total absorption yield. The total absorption yield was calculated from the number of absorption events that were written to tape and the information from the scalers. This calculation was done using the data written to tape to measure the fraction of absorption events that each particular trigger type contained. The product of this fraction with the total number of recorded triggers of this type gave the total absorption yield in this trigger type.

While the cuts on the data which were described in the previous sections eliminated all non-absorption events from the data set, some absorption events were also cut out. This problem was unavoidable because reactions in the scintillator could cause a particle's energy to be inaccurately measured and the MWPC's were not 100% efficient. It was therefore necessary to determine for each trigger type how many of the pion absorption events that were written to tape had been incorrectly classified as non-absorption events. With this information, the true number of absorption events that were written to tape could be determined.

4.3.1 Reaction Corrections

Sometimes the final state particles interacted with nuclei in the scintillator. These nuclear reactions can cause some of a charged particle's kinetic energy to be expended in non-ionizing processes that go undetected. These processes include the knockout of neutrons from nuclei, the loss of kinetic energy in overcoming the binding energy of complex nuclei, and the production of particles that escape the detecting volume. All of these processes cause the measured kinetic energy to be smaller than the actual kinetic energy of the particle when it entered the scintillator. Since the charged particle identification is based on the particle's kinetic energy (see Equation 4.4) a particle that undergoes a nuclear reaction can be misidentified as a lighter particle. Thus, protons that lose enough kinetic energy to nuclear reactions are mistaken for pions, causing some absorption events to be rejected.

The probability of a proton undergoing a reaction depends on its kinetic energy, rising approximately exponentially with energy [52] for proton energies up to 250 MeV. However, only some of the protons that undergo nuclear reactions lose so much energy that they cannot be distinguished from pions.

The particle identification and energy cuts were constructed to minimize the number of protons incorrectly identified as pions. Such errors were minimized by a) making the particle identification cuts as generous as possible while still excluding pions, and b) keeping the total energy cut as low as is reasonable given the point where the other reaction channels begin to contaminate the spectrum. This procedure was successful at keeping the reaction corrections small. (See Table 4.3.) Still, the number of absorption events lost because of reactions needed to be quantified and the cross sections corrected.

It was possible to quantify the reaction corrections with the data, using the MWPC's and specific absorption channels whose complete kinematics could be calculated from only the angular information.

In the reaction ^{2}H(π^+, pp), the two protons come out back to back in their CM frame. By transforming the angles of all the charged particles to the π - ^{2}H CM frame and making a sharp cut on the opening angle between the protons, it was possible to make a clean identification pion absorption events on ^{2}H. To have an accurate enough determination of the opening angle, the events had to be restricted to absorption events in which both protons left a signal in both MWPC's. In order to eliminate πp final states from heavier nuclei, a target and target radius cut were also required. These requirements meant that events in which one proton stopped in

Energy (MeV)	Target	Trigger Type 2C0N 2 protons	 2C≥1N 2 protons	 3C≥0N 2 protons	 3 protons	Weighted Average
118	^{2}H	1.04	1.17	1.05	–	1.06
162	^{2}H	1.07	1.21	1.08	–	1.10
239	^{2}H	1.13	1.27	1.32	–	1.20
118	^{3}He	1.04	1.18	1.05	1.03	1.05
162	^{3}He	1.07	1.21	1.08	1.06	1.09
239	^{3}He	1.13	1.28	1.34	1.13	1.17

Table 4.3: Reaction corrections as calculated from $^2\mathrm{H}(\pi^+, pp)$ and $\pi^+ + {}^3\mathrm{He} \rightarrow \mathrm{p} + \mathrm{p} + \mathrm{p}$ events separated out using the MWPC's. These factors corrected the number of absorption events found in each trigger type and number of protons above threshold for reactions in the scintillator. (See Equation 4.6.) The weighted average was not used in the analysis but represents the size of the correction to the total absorption cross section.

the endcap were not included in this sample. It was assumed that the reactions in the endcaps, since they were made of the same material, were not significantly different than the reactions in the cylinder. This assumption is adequate, given that the total phase space coverage of the endcaps was small; thus, the correction in the endcap would have to have been much different than in the cylinder to have had a significant effect on the cross sections.

This set of events, which had been separated out completely independently of the scintillator, could then be run through the particle identification and energy cuts, thereby measuring the percentage of absorption events that were rejected in each analyzed physics trigger type. The size of the correction was different for each event type, as may be understood by considering the 2C0N and 2C1N event types. The 2C0N events contained particles that scattered into an adjacent counter, while such occurrences made up a major fraction of the 2C1N event type. Particles that had a nuclear reaction in the scintillator were much more likely to fire an adjacent counter, because the reaction products or the particle's altered trajectory were not necessarily directed radially outward from the target. Therefore particles that underwent a reaction made up a larger fraction of the 2C1N event type than of the 2C0N event type.

To obtain the reaction corrections for ^{3}He, a similar trick was performed using the reaction $\pi^+ + {}^3\mathrm{He} \rightarrow \mathrm{p} + \mathrm{p} + \mathrm{p}$ to obtain events with three protons in the final state. It was again imperative that all protons have two MWPC hits and that the events be restricted to coming from ^{3}He by a target cut in both the z and r coordinates. The six angles measured with the wire chamber together with the incident pion momentum and the ^{3}He mass over-determine the

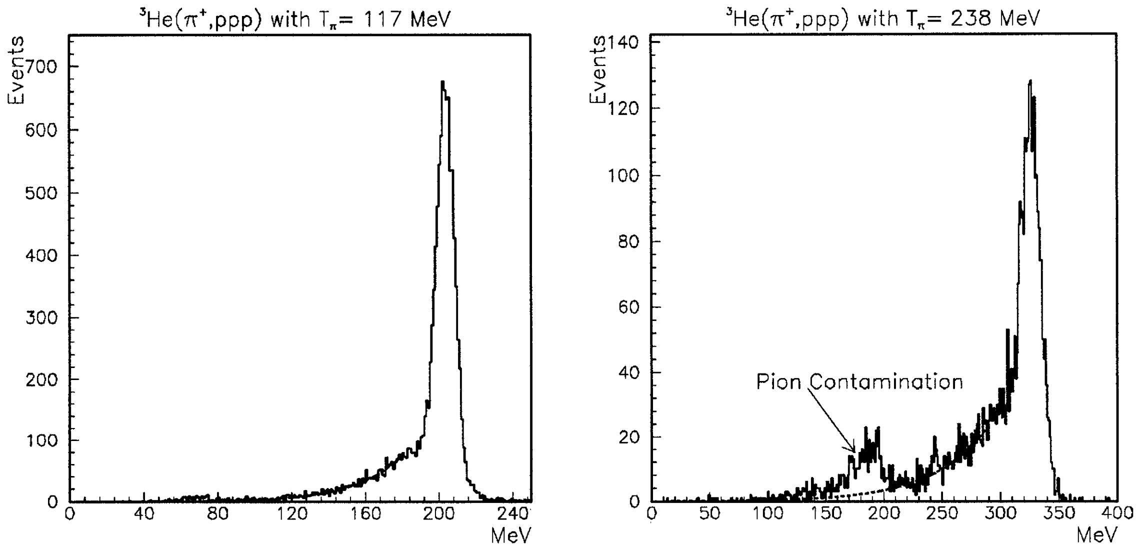

Figure 4-8: Sum of the kinetic energy of the three charged particles after the events have been separated using only the MWPC information. The runs at the highest pion kinetic energy had the largest amount of pion contamination, while the runs at the lowest energy had almost none. The dashed line is the exponential fit to the reactions which was used to extrapolate the number of three-proton absorption events through the pion contamination to zero energy.

kinematics of the final state by one measurement *if* the masses of outgoing particles are known. The invariant mass of the system could be reconstructed assuming a three-proton final state and if the final state particles were indeed protons, the invariant mass calculated corresponded to the invariant mass of the initial state. Cutting on this peak in the invariant mass spectrum separated out the $\pi^+ + {}^3\mathrm{He} \rightarrow \mathrm{p} + \mathrm{p} + \mathrm{p}$ reaction. Unfortunately, this separation was not as clean as the ${}^2\mathrm{H}(\pi^+, pp)$ separation; some πpp contamination remained in the data and is shown in Figure 4-8. To estimate the pion contamination the reaction tail above the incident pion kinetic energy was fit to the expression:

$$Counts = ae^{b(1-f)} , \tag{4.5}$$

where f represents the fraction of energy lost by the absorption event and a and b are arbitrary constants. The form of this equation can be justified by the shape of the summed energy plot at the lowest energy where the pion separation using the MWPC's only was the cleanest.

This method determined the pion contamination in these data sets to be to be 1%, 5%, and 11% for incident pion energies of 118, 162, and 239 MeV, respectively. The particle identification and energy cuts were then applied to the set of data filtered using only the MWPC's. The number of events cut out which exceeded the pion contamination was used to quantify the reaction correction for the three proton final states in ^{3}He.

It was not possible to use the wire chamber to isolate a set of absorption events for the final states in ^{3}He when only two of the three protons were detected. However, since LADS's solid angle is 98.5% of 4π, the undetected proton was almost always undetected because it had very little energy. Therefore the energy distribution of the two proton final states are very similar to the energy distribution of the ^{2}H(π^+, pp) final states. The major differences between the two reactions are the difference in binding energy between ^{2}H and ^{3}He, and the average amount of energy carried away by the undetected proton in ^{3}He. Since these differences are small, the two proton final states of ^{3}He were corrected with the same correction that was used in the ^{2}H(π^+, pp) reaction after a small adjustment was made to allow for the increased binding energy of ^{3}He. This procedure could be flawed if the reaction corrections were large.

4.3.2 Wire Chamber Efficiency

There are three separate effects that cause the MWPC's in LADS to be less than 100% efficient for the detection of protons. MWPC's commonly have a single charged particle detection efficiency that is slightly less than 100%. When several particles pass through a MWPC during a single event, two further complications arise. In LADS, a hit is found by the intersection of two cathodes, and in multiple particle events it is possible for the software to incorrectly associate cathodes from different particles with each other. Incorrectly associated cathodes result in reported hits having ϕ and z values that do not match either particle's actual ϕ and z values and these reported hits will most likely not be associated with any of the hits in the scintillator (see Section 3.5). In multi-particle events it is also possible for two or more particles to hit the same cathode strips. Since assignments are made for pairs of hits and double assignments of cathode hits are forbidden by the code, this procedure typically results in only one cathode intersection being reconstructed.

It was possible to measure and closely examine the single particle efficiency of each chamber using the ^{2}H(π^+, pp) reaction and the energy determination from the plastic scintillator. Because the deuteron is loosely bound, the two protons from ^{2}H(π^+, pp) have 20–30 MeV more kinetic energy than protons from any other reaction that is possible when the target cell contains

Run Number	Energy	Proton Detection Efficiency	
n	T_π	ϵ_{inner}	ϵ_{outer}
733	239 MeV	$0.978 \pm .02$	$0.963 \pm .01$
851	118 MeV	$0.978 \pm .009$	$0.975 \pm .006$
1215	162 MeV	$0.977 \pm .008$	$0.981 \pm .02$

Table 4.4: Single proton detection efficiencies for the inner and outer MWPC's for three ^{2}H runs at approximately the beginning, middle and end of data taking.

^{2}H. By placing a cut on the total light deposited in the cylinder part of the plastic scintillator, it was possible to separate out ^{2}H(π^+, pp) events in which both protons went through both MWPC's. The kinematic correlation of the two protons was doubly advantageous. Since the opening angle could be calculated from the θ of one proton it was possible to ensure that the two protons did not hit the same cathode strips. When two protons hit the same cathode strip, only one is properly reconstructed. However, since its angle is known, that event can be rejected as having an overlapping strip problem. Rejection of events with overlapping strips is desirable since this problem is a multi-particle effect and the attempt here is to measure the single particle efficiency. Moreover, if an event had two hits on one wire chamber and one assumed that the interaction took place on the beam axis, one could specify the angles of the protons. Using this correlation it was then possible to examine the single particle efficiency of the MWPC's as follows: if one MWPC had two hits, the other MWPC was checked to see if hits could be found in the appropriate places on the other MWPC. A single-particle efficiency was calculated by dividing the number of times a hit was missing by the total number of hits the MWPC should have had according to the other chamber. The single particle efficiency was measured for three different points of the run: near the beginning, in the middle, and at the end. The chamber efficiency was found to remain the same within statistical uncertainty. (See Table 4.4.)

It was also possible to use the above method to check the response of the chambers to particles traversing the MWPC with different angles and energies. The response of the MWPC's did not change over the range of available angles and energies sampled in the ^{2}H(π^+, pp) reaction where both protons stopped in the cylinder.

The MWPC efficiency for multi-particle events is very complicated since it depends in a complex way on the relative positions of the particles, which are among the quantities that LADS is attempting to measure. However, if it were possible for each target nuclei and incident pion energy to isolate a random sampling of the absorption data independent of the MWPC's, it would become possible to measure the multi-particle efficiency of the MWPC's. First, one would classify the absorption events by trigger type as well as the number of protons which traversed both chambers and the number which passed only through the inner chamber. Then each class of events would be run through the analysis to determine the efficiency for that class of events. This method would be a true measure of all of the MWPC inefficiencies.

While choosing a completely random set of absorption events is not actually possible, it is possible to approximate this criterion for the ^{2}H and ^{3}He nuclei by cutting on the light deposited in the scintillator. The amount of energy carried by the charged particles in absorption on both ^{2}H and ^{3}He is larger than the amount of energy released in any other possible pion reaction channel in these targets or the nuclei of the target container or the air inside the detector. When all the absorption protons with significant energy deposit this energy in LADS, an absorption peak is produced (as in Figure 4-9). Because of the LADS 4π solid angle coverage and low threshold, almost all absorption protons with more than 20 MeV of energy enter the scintillator. In some absorption events, one or more protons have a reaction and their energy is outside of the peak. We assert that the correlation between an event being within the peak and the relative position of the particles is weak *within* each class. Variations between classes are provided for since each class has its own MWPC efficiency correction.

This reasoning suggests the following procedure to measure the MWPC efficiency. For ^{2}H a rather tight cut is made on the light deposited in the scintillator around the absorption peak. Because of the geometry of LADS, a particle originating at the target and stopping in the endcap goes through only the inner MWPC, and a particle originating at the target and entering the cylinder must have gone through both MWPC's. The events are then classified by trigger type. Because all the final state particles are charged and neutral hardware triggers do not come from neutral particles but rather from protons crossing sector boundaries, it is necessary only to separate the protons into two groups, those events coming from triggers of 2C0N and 2C1N, and those events coming from the 3C trigger. Next, the events must be further divided into those events in which both protons went through both chambers and events in which one proton went through both chambers and one proton stopped in the endcap. Because of the requirement that each event have at least one particle that did not hit an endcap, the 3C triggers had no events in the class of events in which one proton went through both chambers and the other proton stopped in the endcap. Events in each class were analyzed to see if they passed the requirements of adequate MWPC information as described in Sections 4.1.1 and 4.2.1, but excluding the cut on the z-coordinate of the vertex since the absorption events could come from the entire target volume in this procedure.

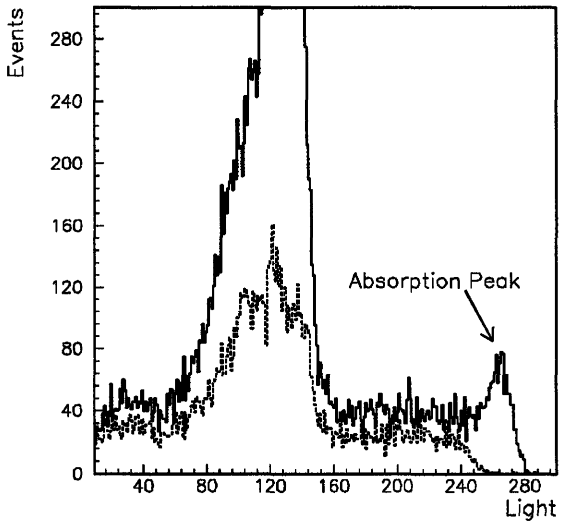

Figure 4-9: Figure shows light deposited in the scintillator when two charged particles were detected in ^{3}He. This is among the worst cases, since there is a spectator proton in the final state whose energy is not detected. The solid line is the spectrum when the target was filled; the dashed line is the spectrum when the target is empty. The incident beam is π^+ with $T_\pi = 162$ MeV. The spectra are not normalized to the amount of incident pion flux.

A problem encountered for ^{2}H at 240 MeV was that the most forward proton was not stopped by the scintillator in the class of events where one particle went into the endcap. This effect meant that these events were not in the absorption peak because some of the energy escaped the detecting volume. The variations with energy were not large, and this class of events represents less than 10% of the total cross section, so the closest energy to it was used and larger systematic uncertainties were assigned (for further details see Section 5.3.2).

For ^{3}He, the procedure was essentially the same, except that the number of different classifications was larger. For two detected charged particles, a cut was made on the absorption peak and these events were classified in the same manner as on ^{2}H. For three detected charged particles only the analyzed 3C trigger type was relevant and the three classes were: three protons passing through both chambers, two protons passing through both chambers and one proton stopping in the endcap, and one proton passing through both chambers with two protons stopping in the endcap. (See table 4.5.)

T_π (MeV) ^{2}H	MWPC Efficiency for an Absorption Events on ^{2}H					
	2C		3C			
	$\eta_{(2,0)}$	$\eta_{(1,1)}$	$\eta_{(2,0)}$	$\eta_{(3,0)}$	$\eta_{(2,1)}$	$\eta_{(1,2)}$
118	$.994 \pm .001$	$.817 \pm .011$	$.987 \pm .003$	–	–	–
162	$.992 \pm .001$	$.777 \pm .018$	$.989 \pm .003$	–	–	–
239	$.991 \pm .002$	–	$.988 \pm .007$	–	–	–
^{3}He	MWPC Efficiency for an Absorption Events on ^{3}He					
118	$.985 \pm .001$	$.774 \pm .010$	$.966 \pm .002$	$.935 \pm .001$	$.871 \pm .003$	$.609 \pm .010$
162	$.982 \pm .002$	$.782 \pm .020$	$.967 \pm .003$	$.939 \pm .001$	$.880 \pm .004$	$.585 \pm .018$
239	$.981 \pm .003$	$.722 \pm .033$	$.939 \pm .007$	$.923 \pm .002$	$.858 \pm .005$	$.565 \pm .027$

Table 4.5: η represents the probability that the MWPC's will provide the angular information needed for an event to be analyzed. η is dependent upon the trigger type and the geometry of the event which is represented by the ordered pair (i, j) where i and j are the number of protons that stop in the cylinder and endcap respectively. Uncertainties are statistical only.

4.3.3 Classifying and Quantifying Absorption Events

4.3.3.1 Separating Events by Number of Detected Protons

Within each trigger type, the events were further broken down by the number of charged particles above the threshold energy. The number of absorption events with two protons above threshold was calculated separately from those events with three protons above threshold. Absorption events with only one proton above threshold were cut out by the charged particle cut (described in Section 4.2.2).

The threshold was set on the energy of the particle after energy-loss and saturation corrections had been applied. Only those particles above threshold were used in the analysis. Particles below threshold were ignored for the purposes of determining the number of protons in the final state, the total energy of an event, the number of protons in the endcap, etc. The only exception was that the event was rejected if the below-threshold particle was identified as a pion or if it did not have the MWPC information required of charged particles.

For the total cross sections, the threshold was set at 5 MeV. Setting the threshold so low meant that the effective threshold was determined by the amount of material between the interaction point and the scintillator. This effective threshold energy varied between 12 and 20 MeV because of the variation in angles of the particles' trajectories. This threshold value was termed the "detector threshold." When a constant threshold over the entire detector was desired for differential plots, the threshold was set to a value above 20 MeV.

4.3.3.2 Calculating the Absorption Yield with Two and Three Detected Protons

For each experimental run, the above analysis yielded the number of absorption events with two and three detected protons above threshold. The following expression was used to calculate the absorption yield:

$$N_p = \sum_{trig} m_p X_{trig,p} \ ; \tag{4.6}$$

$$m_p = n_{p,full} - n_{p,empty} \left(\frac{B_{full}}{B_{empty}} \right) \ ; \tag{4.7}$$

$$n_p = \frac{S_{trig}}{A_{trig}} \sum_{all\ g} \frac{a_g}{\eta_g} \ . \tag{4.8}$$

N_p = the number of detected absorption reactions with p protons above threshold.

m_p = the number of absorption reactions in a specific trigger with p protons above threshold after empty target subtraction.

$X_{trig,p}$ = the correction for reactions in the scintillator for this trigger type with p protons above threshold.

$n_{p,full}$ = the number of absorption reactions in a specific trigger with p protons above threshold before empty target subtraction.

$n_{p,empty}$ = empty target background for this trigger type with p protons above threshold. $n_{p,empty}(B_{full}/B_{empty}) = n_{p,full} \times$ the percentage reported in Table 4.1.

B = number of pions incident on the full (empty) target.

S_{trig} = the number of times a given trigger occurred. This number came from a scaler and was not affected by computer dead time or prescale factors.

A_{trig} = the number of analyzed events of this trigger type.

g represents a particular event configuration classified by the number of charged particles that are in the cylinder and/or endcap. For example one charged particle in the cylinder and one charged particle in the endcap is a different configuration than two charged particles in the cylinder and none in the endcap.

a_g = the number of absorption events found in the analysis for a particular configuration.

η_g = the wire chamber efficiency calculated for this configuration.

4.4 Beam Normalization

To determine the number of pions incident on the target, several corrections must be applied to the beam scaler. (The beam scaler counts "beam triggers" which are described in Section 2.13.)

First, there was the problem of satellite peaks in the TDC spectrum of S_{beam} which are shown in Figure 4-10. These events are believed to come from pions hitting the phototube attached to the S_{beam} scintillator. The summed energy spectrum for events associated with the satellite peaks was much different than the spectrum for those events that came from the target. However, it was not necessary to know the cause of the satellite peaks to exclude them with a cut on the S_{beam} TDC. Second, a small fraction (1–2%) of events left a very large signal in the S_{beam} ADC. These events were excluded to ensure that the pions had not lost large amounts of energy before hitting the target.

The corrections for the cuts placed on the S_{beam} TDC and ADC were done as follows. The "beam events" written to tape consisted of a random sampling of those triggers which counted beam particles on their way to the target. "Physics events" consisted of a random sampling of those occurrences where something was detected in the plastic scintillators of LADS in coincidence with a beam particle on its way to the target. The cuts on the S_{beam} TDC and ADC were set in the same place for both the physics and beam events that were analyzed. Physics events which failed the S_{beam} ADC and TDC cuts were not analyzed further and thus did not contribute to the absorption yield (see Section 4.3). The beam scaler counted the total number of "Beam events." To correct the beam scaler so that it represented the number of acceptable beam events, the beam scaler was multiplied by the fraction of beam events written to tape that were not cut out by the S_{beam} ADC and TDC cuts. (See Equation 4.9.) This

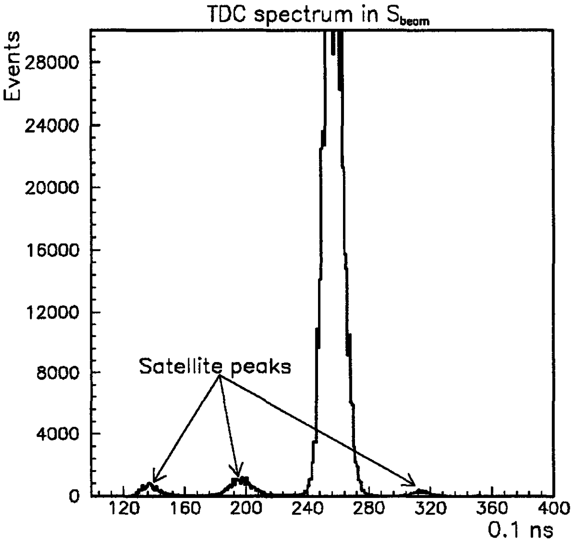

Figure 4-10: Example of S_{beam} TDC spectrum showing the satellite peaks for runs with an incident pion energy of 118 MeV. The satellite peaks were many times larger at this energy than at the other two energies. Events that were below channel 240 or above channel 280 in this spectrum were cut for this run.

procedure meant that the beam scaler could be properly normalized for any arbitrary cut on the TDC and ADC of S_{beam} as long as these cuts were tight enough to reject any events that were not caused by a pion on its way to the target cell. The procedure is robust in that even if the cuts reject some pions, the beam scaler will still be properly normalized.

The beam had some muon contamination due to pions decaying in the πM1 channel and going through S_{beam}. To model this, TURTLE [53] was run with the parameters of the πM1 channel with the slit and magnet settings used during the experiment. The multiple scattering in the air of the channel and in S_{time} were included. This simulation gave an estimate of the number of muons which would cause a beam trigger and not be vetoed by time of flight. The muon contamination to the beam is given in Table 4.6 as f_{contam}.

The beam was also corrected for those pions that decayed after S_{beam} to the middle of the target. The total decay length was 47.5cm. This correction, f_{decay}, was always less than 3%.

Corrections were also made for those pions lost from the beam by reactions in the S_{beam} counter, air, target entrance window, or target gas. These corrections, f_{react}, were calculated

Energy (MeV)	Target	Beam Corrections $f_{Sbeam\ cut}$	f_{contam}	f_{react}	f_{decay}	f_{miss}
118	^{2}H	0.076 ± .015	.020	0.018	0.027	0.061 ± .005
162	^{2}H	0.025 ± .005	.018	0.022	0.025	0.057 ± .005
239	^{2}H	0.029 ± .008	.018	0.015	0.021	0.052 ± .005
118	^{3}He	0.075 ± .010	.020	0.018	0.027	0.060 ± .003
162	^{3}He	0.028 ± .007	.018	0.022	0.025	0.060 ± .004
239	^{3}He	0.025 ± .003	.018	0.017	0.021	0.049 ± .003

Table 4.6: Corrections to the $\mathrm{S_{beam}}$ scalar. Uncertainties are statistical and given only for quantities determined from the data. For definitions of each quantity see equation 4.9.

analytically using previously measured pion reaction cross sections [9, 13, 8]. They were less than 2.5%.

It was also necessary to account for the fraction of pions that missed the target due to multiple scattering and beam optics. The profile of the beam was found by using the air in LADS as a target of uniform thickness. A cut was made with the MWPC's on the events originating in a 5 cm slice of air a few centimeters before and after the target. The ratio of the number of events that were found in each slice within a 2 cm radius (the radius of the target) to the number outside of the 2 cm radius represented the fraction of the beam that missed the target. The fractions calculated from the slices before and after the target were averaged to give an overall correction factor (f_{miss}) for the total beam on target.

The following expression was used to calculate the number of pions on target:

$$B = S_{beam}\,(1 - f_{Sbeamcut})\,(1 - f_{react})\,(1 - f_{decay})\,(1 - f_{miss})\,(1 - f_{contam}) \;, \tag{4.9}$$

where

B = the number of pions incident on the target;

S_{beam} = the number of pions counted by the beam scaler;

$f_{Sbeam\ cut}$ = the fraction of beam events that failed the cuts on the $\mathrm{S_{beam}}$ ADC and TDC;

f_{react} = the fraction of pions that reacted in the air, target windows, etc;

Target	Energy (MeV)	Temperature (°C)	Pressure (Bar)	Z(T,P)
^{2}H	118	33.1	98.7	1.057
^{2}H	162	31.4	94.8	1.056
^{2}H	239	35.0	74.4	1.051
^{3}He	All	32.0	95.0	1.043

Table 4.7: Temperature, pressure and factor of compressibility used in calculation of target density. The target was filled with ^{2}H and emptied at each of the three different energies, while for ^{3}He the target was only filled once and the density remained the same for all experimental runs.

f_{decay} = the fraction of pions that decayed;

f_{miss} = the fraction of pions that missed the target due to beam optics and multiple scattering;

f_{contam} = the fraction of beam events due to contamination of the beam.

4.5 Calculating the Target Thickness

The pressures in the target were high enough that the gas density differed appreciably from the ideal gas law. These deviations were calculated using the expression:

$$PV = Z(T,P)nRT \, , \tag{4.10}$$

where Z is defined as the factor of compressibility and is a function of temperature and pressure. Values for ^{2}H and ^{4}He are tabulated in the *Encyclopedie des Gaz* [54]. Since the atomic properties of ^{3}He and ^{4}He are identical in this temperature regime, the factors of compressibility for ^{4}He were used to calculate the density of ^{3}He. (See Table 4.7.)

4.6 Calculating the Acceptance of LADS

4.6.1 Monte Carlo Calculations of LADS's Acceptance

To obtain integrated cross sections, the data had to be corrected for the geometrical acceptance and energy thresholds of LADS. To make this correction, a specific model of the absorption process needed to be used to extrapolate over the unmeasured regions. In ^{2}H, the model used was a parameterization in terms of Legendre polynomials by B.G. Ritchie [8]. In ^{3}He, the model used was that absorption is dominated by two distinct mechanisms. One is a two-nucleon quasi-free absorption mechanism in which the pion is absorbed by a $T = 0$ pair inside the ^{3}He nucleus with a spectator proton. The second is a three-body mechanism characterized by a final state distributed like three-body phase space. These models will be justified when the results are discussed, though they have previously been indicated by other experiments [55, 56]. Because LADS covers nearly all of phase space, the determination of the total cross sections in ^{2}H and ^{3}He is largely independent of the details of the model, but the determination of the partial cross sections for two- and three-nucleon absorption in ^{3}He are more strongly model dependent and are sensitive to the accurate modeling of the thresholds and geometry of LADS.

To calculate the acceptance of the detector, a Monte Carlo code was developed at MIT to implement the above models. Different mechanisms and nuclei were contained in event generators which were selectable within the Monte Carlo. Otherwise, the acceptance calculations were identical. The geometry, including the position, radius, and sectorization of the endcaps and cylinder, was included. Energy loss for each proton produced by the event generators was done sequentially for each layer of material in Table 2.3. The program LOSSPROG [57] was used to calculate the range tables for each type of material; these range tables were then used to calculate the mean energy loss of the proton through each layer, taking into account the pathlength differences due to the proton's angle of incidence on the material. For those particles near threshold, straggling was also included using the model for straggling developed by C. Tschalär [58].

The Monte Carlo code demanded that a "detected" particle have enough energy to deposit 2.1 MeV of energy in the scintillator, which corresponds to the DE's threshold of detection for protons. If in an event two particles hit the same counter, the code counted only a single detected particle, which is analogous to how LADS counts particles. The energy cuts and threshold cuts used in the analysis of the data were included in the Monte Carlo algorithm. The code had an extended target model with a 2-D Gaussian distribution for the beam profile.

Typically one million events were run. The Monte Carlo programs then used the geometry, energy-loss, thresholds, and total energy cuts to find the fraction of the time that zero, one, two, and three particles were detected.

To calculate the acceptance of LADS for ^{2}H(π^+, pp), the Monte Carlo event generator was the following:

1) GENBOD was called to throw an event in two-body phase space. For each event, it returned two four-momenta and a weight associated with the event.
2) An additional weight associated with this event was calculated using the parameterization of B.G. Ritchie. These two weights, from Genbod and the Ritchie parameterization, were then multiplied together to obtain the weighting for that event.

For ^{2}H(π^+, pp), the acceptance was the sum of the weights when the Monte Carlo reported that two protons were detected for an event, divided by the sum of the weights for all of the events generated by the Monte Carlo. The acceptance was 0.8394, 0.8614 and .8785 at 118, 162 and 239 MeV, respectively.

To calculate quasi-deuteron absorption in ^{3}He, the following method was used:

1) A modified GENBOD was used to throw events in three-body phase space returning three outgoing four-momenta and a weight associated with the event. GENBOD was modified so that it sampled more often in the regions of phase space where quasi-deuteron absorption takes place, and the weights produced by GENBOD were adjusted to compensate for the non-uniformity of the sampling [59]. This procedure reduced the variance of this generator by a factor of five and was in agreement with the results that were produced using an unmodified GENBOD.
2) One proton was designated as the "spectator" proton. This designation defined the spectator proton's four-momenta in the final state to be equal to its four-momenta in the initial state. The event's weight was multiplied by the probability that the spectator proton would have had this Fermi momentum in the initial state, and was calculated from the ^{3}He wavefunction [26, 60] using a particular assumption about the quantum state of the absorbing pair. The quantum state of the absorbing pair had a large effect on the spectator momentum distribution. For this reason, the calculation was done both with the assumption that the absorbing pair was a real deuteron and also with no restrictions on the absorbing pair. The two results were then averaged to obtain the acceptance of LADS to quasi-deuteron absorption.

^{3}He Acceptance for Two and Three Protons				
T_π (MeV)	Mechanism modeled	Spectator distribution	Fraction Detected	
			$f_{p=2}$	$f_{p=3}$
118	2NA	$N_{pd}(k)$	0.7927	0.0501
118	2NA	$N_p(k)$	0.7718	0.0732
118	3NA	–	0.2223	0.7353
162	2NA	$N_{pd}(k)$	0.7935	0.0673
162	2NA	$N_p(k)$	0.7651	0.0975
162	3NA	–	0.1862	0.7692
239	2NA	$N_{pd}(k)$	0.7801	0.1093
239	2NA	$N_p(k)$	0.7171	0.1739
239	3NA	–	0.1424	0.8059

Table 4.8: Results from the Monte Carlo for the 2NA and 3NA generators. The 2NA mechanism uses a quasi-deuteron model where the absorbing pair is either a real deuteron, or has no restrictions. These restrictions affect the spectator momentum distribution, $N(k)$, which is discussed in Section 5.6.4.2. The 3NA mechanism assumes isotropic three body phase space. $f_{p=n}$ is the fractional amount of each mechanism that the Monte Carlo predicts would result in n protons detected by LADS.

3) The non-spectator particles were then treated as the absorbing pair. The CM frame of this pair together with the incoming pion was calculated, and the event was weighted using the ^{2}H(π^+, pp) differential cross section as parameterized by Ritchie. The total energy used in Ritchie's parameterization was calculated from the energy of the absorbing pair in the final state. This method had the effect of including the energy dependence of the ^{2}H(π^+, pp) total absorption cross section into the model, thus including the effect of the Δ-resonance. If the absorbing pair was so far off the mass shell that the energy of the incoming pion was not large enough to bring the particles back onto the mass shell, the event was rejected. This occurred in only a handful of cases in a typical 1 million event run. The weight of the event was also adjusted to take two-body phase space out of the ^{2}H(π^+, pp) differential cross section.

To calculate three-body phase space, GENBOD was called to throw an event in three-body phase space. For each event it returned three outgoing four-momenta and a weight associated with the event.

For both of the ^{3}He generators, the fraction when two (three) protons were detected was calculated using the sum of the weights when two (three) protons were detected divided by the sum of all the weights generated.

4.7 Cross Section Calculations

4.7.1 Cross Section Calculations for ^{2}H

The following formula was used to calculate the total cross section for pion absorption on ^{2}H:

$$\sigma = \frac{N}{\Omega B T}, \tag{4.11}$$

in which

N is the number of absorption reactions that were detected by LADS;

Ω is the acceptance of LADS for $^2\mathrm{H}(\pi^+, pp)$ events;

B is the number of pions incident on the target;

T is the target thickness in nucleons per cm^2.

4.7.2 Cross Section Calculations for ^{3}He

For ^{3}He, both a quasi-deuteron process and a phase space distributed absorption process could generate reactions where two or three protons were detected. To separate out the fraction of the reactions that were classified as two nucleon absorption (2NA) and the fraction that were classified as three nucleon absorption (3NA), it was necessary to solve two equations with two unknowns. This separation depended on the accuracy of the event generators which were employed, although the total cross sections were much less model-dependent.

$$\begin{aligned}
\sigma_p &= \frac{N_p}{BT} && (4.12)\\
\sigma_{p=2} &= \sigma_{2NA} f_{2NA,\ p=2} + \sigma_{3NA} f_{3NA,\ p=2} && (4.13)\\
\sigma_{p=3} &= \sigma_{2NA} f_{2NA,\ p=3} + \sigma_{3NA} f_{3NA,\ p=3} && (4.14)\\
\sigma_{total} &= \sigma_{2NA} + \sigma_{3NA}, && (4.15)
\end{aligned}$$

where

p is the number of detected protons above threshold, and can equal 2 or 3;

f_{2NA} is the fraction of the weights in which the quasi-deuteron Monte Carlo code reports that p protons are detected. These are found in Table 4.8;

f_{3NA} is the fraction of the weights in which the phase-space Monte Carlo code reports that p protons are detected;

σ_{2NA} and σ_{3NA} are the cross sections for 2-nucleon absorption and 3-nucleon absorption, respectively, which are calculated by solving Equations 4.13 and 4.14 simultaneously.

Chapter 5

Uncertainties

The previous chapter described the steps and procedures used to measure the absorption cross section in ^{2}H and ^{3}He. Because of LADS's ability to collect copious amounts of data and the relatively large cross sections being measured, the uncertainty in the cross section was dominated by the systematic uncertainties. Systematic uncertainties are often difficult to estimate, and much of the analysis was devoted to quantifying these uncertainties.

The statistical uncertainties for the cross sections were calculated using the standard formula for binomial distributions, where p is the probability of having one of two possible outcomes, and N is the number of trials.

$$\sigma = \sqrt{p(1-p)N} \, . \tag{5.1}$$

The systematic uncertainties were not always symmetrical. For example, sometimes a systematic uncertainty can only influence the cross section in one direction. Often it is likely that this uncertainty has some effect, but only an upper limit to the size of the effect of this uncertainty can be determined. There are different ways of dealing with this. In this thesis the method adopted in these cases was to correct the cross section by 1/2 of the size of the upper limit, and to assign an uncertainty to this correction of 1/2 of the upper limit.

After each uncertainty was determined and ascertained to the best of our ability to be independent, the uncertainties, both statistical and systematic, were propagated using the standard error propagation formula for independent variables.

$$\sigma_f = \sqrt{\sum_i \left(\frac{\partial f(x_1, x_2, \ldots, x_i)}{\partial x_i} \sigma_i \right)^2} \tag{5.2}$$

This chapter describes the efforts to quantify the uncertainties associated with each analysis step in the previous chapter. It is organized to examine the analysis steps in the same sequence as the previous chapter in order to facilitate references between chapters and to demonstrate completeness. This chapter focuses primarily on the systematic uncertainties, because they dominate the error and are more difficult to estimate.

5.1 Systematic Uncertainties in the Isolation of Events Occurring in the Target

5.1.1 Reconstruction of Incorrect Vertices by the Wire Chambers

When absorption events were separated from the data, one of the first steps was a cut on the z-axis position of the event. The events which came from the region of the cut, but lacked a vertex because of missing MWPC information, were taken care of by the MWPC efficiency correction. The MWPC efficiency correction did not correct for events in which a vertex was incorrectly calculated to be far outside of the target region.

There is evidence that sometimes, but rarely, the vertex was reconstructed far from the actual point of origin. This incorrect reconstruction of the vertex was not a resolution effect, since the misreconstructed vertices were many σ from the point of origin and had a flat distribution. The cause of the misreconstructions is unknown, though it plausibly could be caused by the incorrect matching of cathode strips.

There are two ways of estimating the failure of the MWPC to determine correctly an absorption event's vertex, and both give approximately the same answer. Both methods start by using absorption events chosen without MWPC information. These events were separated from the raw data by a tight cut on the absorption peak in the summed light of the scintillator. (See Figure 4-9.)

The first way is to look at absorption events chosen by the above cut in the summed light that have two tracks which do not come within 1 cm of each other. Such events occurred in ^{3}He with a frequency of about 1.5% for 2p events and about 3.0% for 3p events. Since one track is randomly chosen for the determination of the vertex, one expects to be correct 1/2 the time for 2p events and 1/3 the time for 3p events. These frequencies would imply a misreconstruction of about 0.8% for 2p and 2.0% for 3p.

The second way to measure misreconstructed events is to look at the vertices reconstructed from events known to come from the target gas because of the tight cut in summed light on the absorption peak. In ^{2}H, about 0.8% of these events had reconstructed vertices that were not in the target region, which agrees very well with the above estimate. In ^{3}He, the estimate was more difficult since the difference in binding energy between ^{3}He and the air in the detector is not as great, and some of the events whose vertices have been reconstructed to come from the air might indeed originate in the air. For example, a very small peak coming from the S_{beam} was clearly evident in the ^{3}He data indicating some contamination in the data from elements heavier than ^{3}He. However, because the total background was small, it was possible to set an upper limit of 2.0% on the possible vertices that were misreconstructed.

The 2p and 3p data were corrected by $1.008 \pm .004$ and $1.02 \pm .01$ respectively to account for the misreconstruction of vertices.

These corrections do not account for vertices that are mistakenly reconstructed to be just outside the z-axis cut due to the finite resolution of the MWPC's. The loss of events due to the MWPC resolution from the defined target volume is compensated for by the events just outside the defined target volume that are included because of the MWPC resolution. These competing effects should exactly cancel each other.

5.1.2 Uncertainties and Corrections to the Empty Target Subtraction

The z-axis cut served to eliminate most of the background from the target cell. The cut eliminated background from the target's entrance and exit windows, but background from the target walls remained, since no radius cut was applied. See Section 4.1.2. The background subtraction to account for events originating in the target cell's walls was performed using empty target runs. The empty target was verified to be in the same place as the full target to within 1 mm using the MWPC's vertex reconstruction. One complication which arises from using an empty target is that one expects the multiple scattering of the beam to be less in the

Fraction of beam within the target radius			
Energy	Target	Before	After
118	Empty	0.965 ± .004	0.922 ± .005
118	^{2}H	0.967 ± .005	0.912 ± .009
118	^{3}He	0.965 ± .003	0.915 ± .006
162	Empty	0.966 ± .003	0.934 ± .005
162	^{2}H	0.960 ± .006	0.925 ± .009
162	^{3}He	0.951 ± .004	0.929 ± .006
239	Empty	0.959 ± .004	0.952 ± .005
239	^{2}H	0.960 ± .006	0.936 ± .009
239	^{3}He	0.961 ± .004	0.942 ± .005

Table 5.1: This table shows the fraction of the beam within the target cell radius, measured before the target cell's entrance window and after the target cell's exit window.

empty target than in the full target. This decrease in scattering should reduce the fraction of beam that hit the target walls in the empty target runs.

The expected spreading of the beam due to multiple scattering was sought by looking at the vertices from pion reactions in the air just before and after the end of the target in both the full and empty target runs. In Table 5.1, little statistically significant increased beam spreading is seen in the filled target runs in comparison to the empty target runs.

Another check of the adequacy of the target subtraction is the number of four detected protons from the ^{2}H runs. Four protons in the final state are unlikely to come from processes other than absorption in the heavier material of the target walls. Therefore, the fact that the cross section for four protons in ^{2}H is larger than zero (see Table 5.2) could be evidence that the empty target subtraction is too small. While the amount of data in this channel is completely insignificant for the total cross section, it can be used as an upper limit on the increased empty target subtraction necessary to account for multiple scattering in the target gas. The empty target subtraction was increased by 1/2 of the missing fraction plus the error, and the possible uncertainty of the subtraction was assigned to be the same size. Because the total background target subtraction was small and a more accurate estimation of the increased multiple scattering would not have substantially changed the results, it was assumed that the multiple scattering in ^{3}He was the same size as that measured in ^{2}H.

Fraction of 4 proton events left in ^{2}H		
Energy	Fractional Excess of 4p	Empty target correction
118	$0.2 \pm .1$	$1.15 \pm .15$
162	$0.3 \pm .1$	$1.2 \pm .2$
239	$0.3 \pm .1$	$1.2 \pm .2$

Table 5.2: After empty target subtraction, some fraction of the cross section in the four detected proton channel was left. This fraction plus its associated uncertainty was used as an upper limit for the amount the empty target should be increased by to account for the difference between the full and empty target runs.

5.2 Contamination of the ^{2}H and ^{3}He Absorption Events from Other Reactions

Substantial effort was made to eliminate from the absorption data set all events that had a pion in the final state. This rejection of the pions was done using particle identification and total energy cuts as described in Sections 4.2.2 and 4.2.3. Nevertheless, some pions passed all of these cuts. In ^{2}H, the number of pions that passed the cuts could be quantified by looking in the π - ^{2}H center of mass system at $\theta_{1CM}+\theta_{2CM}$ vs. $|\phi_1-\phi_2|$. See Figure 5-1. Pion absorption on ^{2}H appears as the sharp peak at $\theta_{1CM}+\theta_{2CM} = 180°$ and $|\phi_1-\phi_2| = 180°$. The rest of the events can be explained as: a) absorption on nuclei other than ^{2}H, for example absorption on C in the walls of the target, or b) events from the reaction ^{2}H(π^+,π^+p) where the pion was absorbed in the scintillator, releasing enough energy that the particle passed the particle identification cuts and the event passed the total energy cut.

The reaction ^{2}H(π^+,π^+p) has most of its strength at $\theta_{1CM}+\theta_{2CM} < 180°$ and $|\phi_1-\phi_2| \approx 180°$, as shown in Figure 5-2. To quantify the pion contamination in the data, the region $110 < \theta_{1CM}+\theta_{2CM} < 175$ and $120 < |\phi_1-\phi_2| < 240$ was used. Empty target background in this region was subtracted from the ^{2}H events in this region, and the remaining events were used as a measure of the pion contamination. This process was done for each analyzed trigger type, and the data in Table 5.3 follow the general trends that were expected. In particular, the pion contamination increased as a function of incident pion kinetic energy, and the amount of contamination was largest for the 2C1N analyzed triggers. The energy dependence can be understood by noting that high energy pions are more likely to react in the scintillator than low energy pions, and that the difference between the β of protons and pions becomes smaller

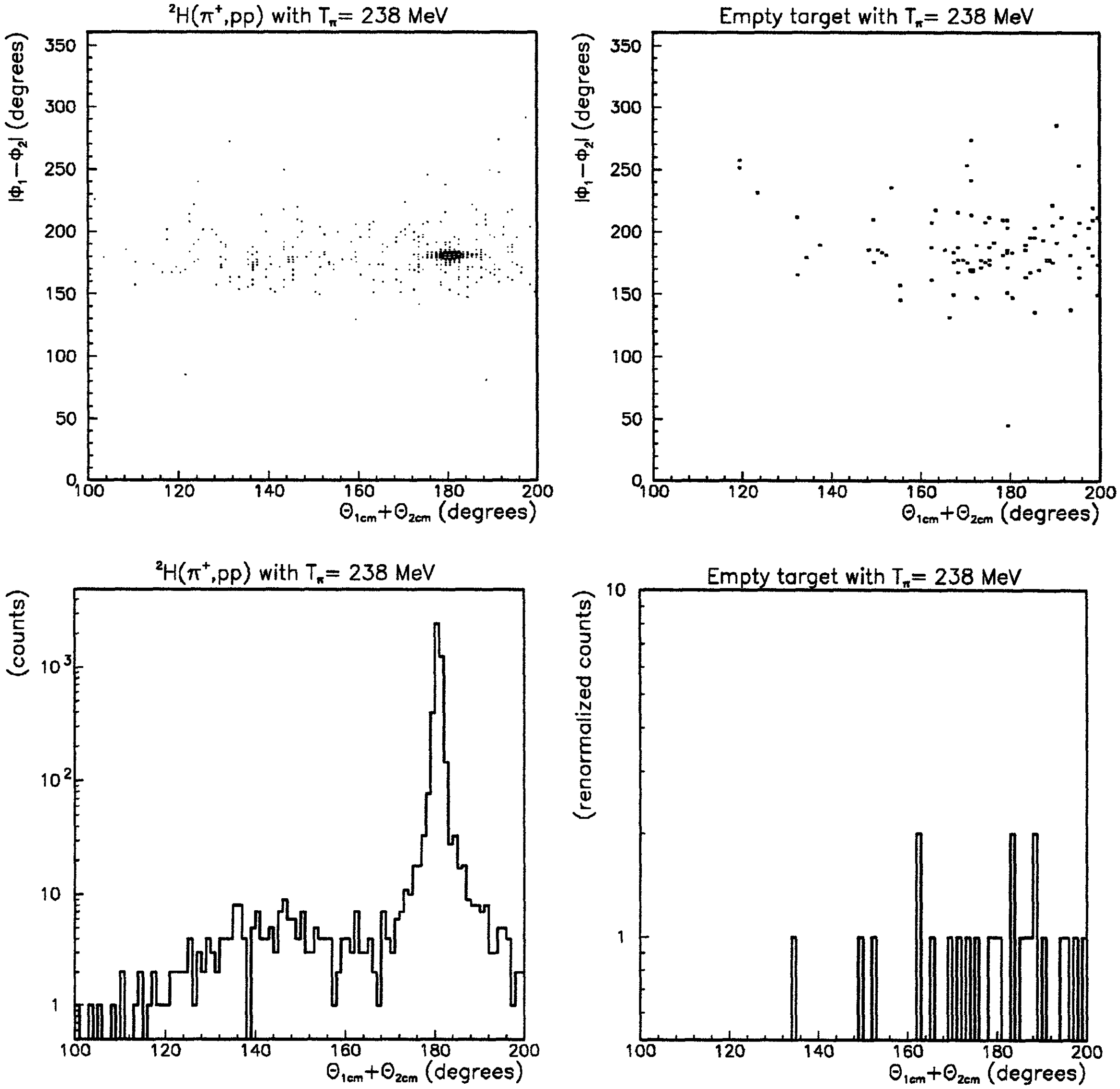

Figure 5-1: The comparison of the number of counts in the region $110 < \theta_{1CM} + \theta_{2CM} < 175$ and $120 < |\phi_1 - \phi_2| < 240$ provided a measurement of the pion contamination. The projection of the empty target run on $\theta_{1CM} + \theta_{2CM}$ is normalized with respect to the ^{2}H run shown. These figures have both 2C and 2C1N triggers, when both charged particles are in the cylinder and after the PID and total energy cut have been applied.

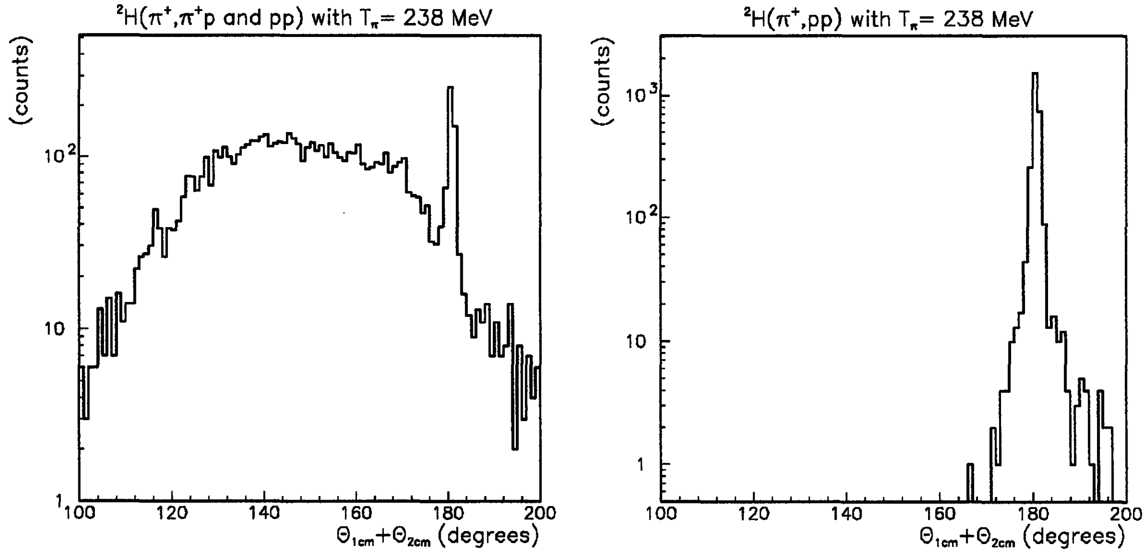

Figure 5-2: Figure a) depicts the opening angle between the two charged particles when there are no PID cuts, which shows the πp contamination as a broad peak located primarily in the range $110 < \theta_{1CM} + \theta_{2CM} < 175$. Figure b) shows the absorption peak which is isolated using the PID cuts and a very tight cut on the total energy deposited by the particles. These figures have both 2C and 2C1N triggers when both charged particles are in the cylinder.

Energy (MeV)	Target	Trigger Type 2C0N	 2C≥1N	 3C≥0N	Weighted Average
118	^{2}H	0.0±0.0%	2.0±0.7%	0.3±0.1%	0.2±0.1%
162	^{2}H	1.1±0.4%	3.9±1.3%	1.0±0.3%	1.6±0.5%
239	^{2}H	1.6±0.5%	10.0±3.3%	3.2±1.1%	4.0±1.3%
118	^{3}He	0.0±0.0%	1.4±1.0%	0.2±0.2%	0.2±0.2%
162	^{3}He	0.6±0.4%	2.2±1.5%	0.6±0.4%	0.9±0.6%
239	^{3}He	1.3±0.9%	8.3±5.5%	2.7±1.8%	3.3±2.2%

Table 5.3: Pion contamination in each trigger type when there were two charged particles detected. Errors are systematic. Statistical errors are much smaller than the systematic errors. The ^{3}He numbers are estimated from ^{2}H.

as the kinetic energies increase. The larger amount of pion contamination in the 2C1N events comes from the fact that pions are more likely to scatter into an adjacent E-block than are protons. This is especially true since the pion contamination came from events where the pion absorbed in the scintillator. If one looks at 3C events in which there were actually only two charged particles, one obtains a level of contamination which is between the contamination in the 2C1N and 2C0N events. The 3C trigger includes events both with and without adjacent E-blocks.

The contribution to the cross section from events where one particle stops in an endcap is relatively small (about 8% at 239 MeV), so the pion contamination for this part of the cross section, though looked at, was not measured with the angular distributions. The pion contamination, for events with a particle stopping in an endcap (as seen in the opening angle distributions) did not differ significantly from that for events where both charged particles stopped in the cylinder. The MWPC resolution was a little worse, since endcap particles do not go through the outer MWPC, and the absorption peak was not as narrow as the peak shown in Figure 5-2b) for events with two cylinder particles. Instead of attempting to measure and apply a different correction for events where one of the two particles stopped in the endcap, these events were assigned the pion correction factor that was found for events where both charged particles stopped in the cylinder.

Because the Fermi momentum of the spectator proton in the $^2\mathrm{H}(\pi^+,\pi^+p)$ reaction permits contamination in the separation of absorption using only the angular information, the measurement of the pion contamination being limited to the cylinder and extrapolated over the endcaps, and the target background subtraction being possibly incomplete, the systematic uncertainty of the pion contamination in ^{2}H was estimated to be 1/3 of the correction factor. Though the size of this uncertainty is somewhat arbitrary, it is difficult to argue that it should be larger because each of the three contributions appears to be significantly smaller than 1/3 of the total correction. For example, Figures 5-1 and 5-2 show that the Fermi momentum smearing could not cause an uncertainty of even 25% of the correction factor. The endcaps had only a small percentage of the total events, so given that the spectrum certainly had much less than a factor of three more pion contamination than the cylinder, this uncertainty was also less than 1/4. The empty target subtraction accuracy was discussed in Section 5.1.2, and its uncertainty combined with the uncertainty illustrated in Figure 5-1 d) could not contribute greatly.

In ^{3}He it was not as easy as in ^{2}H to determine the pion contamination when there were two protons detected. The third nucleon could carry away a significant amount of energy, so the absorption peak was not as sharp as in $^2\mathrm{H}(\pi^+,\pi^+p)$. See Figure 5-3. The absorption peak

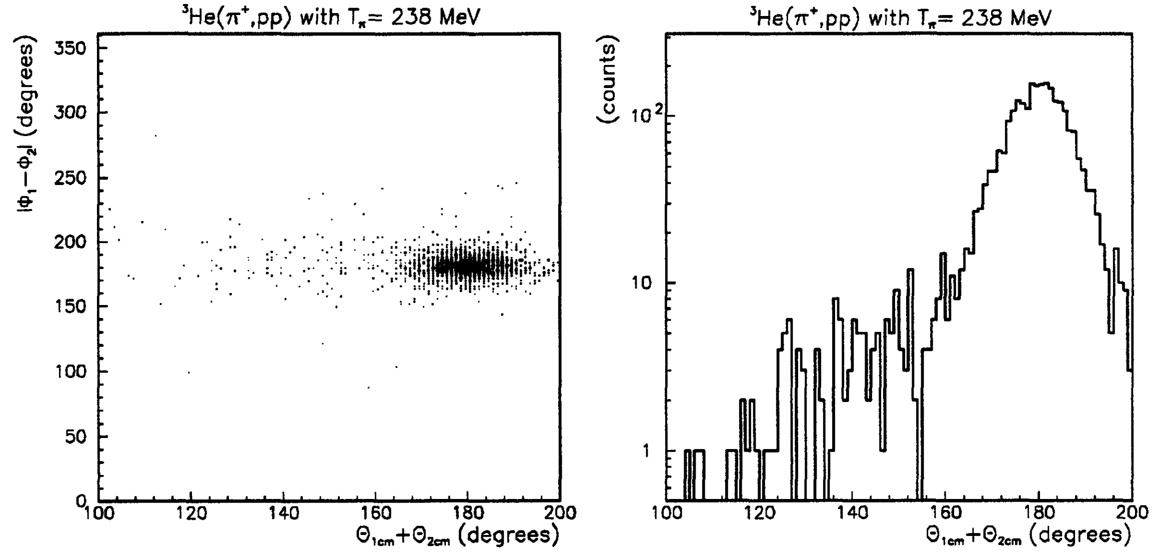

Figure 5-3: Pion absorption in ^{3}He when two protons were detected in the cylinder, showing the smearing of the quasi-deuteron peak due to the Fermi momentum of the spectator proton. (Compare to Figure 5-1.)

overlaps the angular region where inelastic π^+p scattering is expected, but other than this broadening, the spectrum does not look qualitatively different from that of $^2\mathrm{H}(\pi^+,\pi^+p)$. It was necessary to estimate the pion contamination in ^{3}He from the pion contamination found in ^{2}H. As was shown in Figure 5-1, the primary cause of pion contamination in ^{2}H was inelastic π^+p scattering. The $^2\mathrm{H}(\pi^+,\pi^+p)$ cross section is for our purposes essentially equal to the $^1\mathrm{H}(\pi^+,\pi^+p)$ cross section minus 10% to account for shadowing due to the neutron [61]. For the events in ^{3}He in which there are only two detected protons, it is reasonable to attribute the main source of pion contamination to $^3\mathrm{He}(\pi^+,\pi^+p)$, though other channels may also contribute. In ^{3}He the ratio of $^3\mathrm{He}(\pi^+,pp)$ to $^3\mathrm{He}(\pi^+,\pi^+p)$ is somewhat larger than in ^{2}H [13]; therefore it is reasonable to expect the amount of pion contamination in ^{3}He to be less than in ^{2}H. At 118, 162, and 239 MeV the ratios

$$\frac{\sigma\,(^3\mathrm{He}(\pi^+,\pi^+p))}{\sigma\,(^3\mathrm{He}(\pi^+,pp))} \Bigg/ \frac{\sigma\,(^2\mathrm{H}(\pi^+,\pi^+p))}{\sigma\,(^2\mathrm{H}(\pi^+,pp))}$$

are approximately 1.4, 1.8, and 1.2, respectively. The pion contamination in ^{2}H was divided by the ratio at each energy and the systematic uncertainty was increased from 1/3 to 2/3 of the total to account for the increased inaccuracy due to the uncertainty of the ratios and the possible contribution from other channels (see Table 5.3).

To measure the pion contamination for the three-proton events in ^{3}He, it is useful to have a kinematic quantity which is independent of the plastic scintillator, as is the opening angle for the two-proton events in ^{2}H. One such quantity is the energy difference ΔE:

$$\Delta E = \left(\sum_{i=1}^{3}\sqrt{p_i^2+m_p^2}\right) - \left(m_{^3He}^2 + \sqrt{p_\pi^2+m_\pi^2}\right) . \tag{5.3}$$

The $|p_i|$ were obtained by conservation of momentum,

$$0 = \sum_{i=1}^{3} |p_i| \sin\theta_i \cos\phi_i \tag{5.4}$$

$$0 = \sum_{i=1}^{3} |p_i| \sin\theta_i \sin\phi_i \tag{5.5}$$

$$p_\pi = \sum_{i=1}^{3} |p_i| \cos\theta_i , \tag{5.6}$$

Pion Contamination in Three Proton Events from ^{3}He		
Energy	Upper Limit	Correction
118	1.7%	$0.991 \pm .009$
162	3.0%	$0.985 \pm .015$
239	4.4%	$0.978 \pm .022$

Table 5.4: The upper limit in the table represents the percentage of counts in Figure 5-4 b) in the -600MeV spike and the excess in the tail of the distribution at negative ΔE after subtraction of Figure 5-4 c). The correction is the amount that the three detected proton cross section was multiplied by to account for the pion contamination.

using only the angles of the three particles as determined by the MWPC. Events which come from ^{3}He(π^+, ppp) should have $\Delta E = 0$. See Figure 5-4.

The calculation of $|p_i|$ assumes that all final state particles are detected. For πpp final states and for absorption in the heavier nuclei contained in the target walls, not all final state particles were detected; therefore $|p_i|$ could be calculated to have a negative value. Also, $|p_i|$ could be calculated to have a negative value if one particle of a two particle event had a reaction in the scintillator and a reaction product caused an apparent extra track (*i.e.* another dE and MWPC hit). These types of reactions in the scintillator could occur for any process, including absorption. When a $|p_i|$ was negative, it was not possible to calculate a meaningful energy difference for the event and ΔE was assigned to be -600 MeV. Therefore, the spike at -600MeV contains pion contamination, target wall background, and both absorption and non-absorption events where there was a reaction.

Events with a pion have a negative ΔE, since the calculation assumes protons in the final state. See Figure 5-4 a). The pion contamination is almost completely absent from Figure 5-4 b) which represents the three detected proton cross section, in the cylinder part of LADS at $T_\pi = 239$ MeV, before target empty subtraction. Some pion contamination seems to remain even after the subtraction of Figure 5-4 c) from b) in the -600MeV spike, and in the tail of the distribution at $\Delta E < -100$MeV. The number of counts at -600MeV and the excess in the tail of the distribution at negative ΔE were used to set an upper limit on the pion contamination in the three-proton part of the cross section.

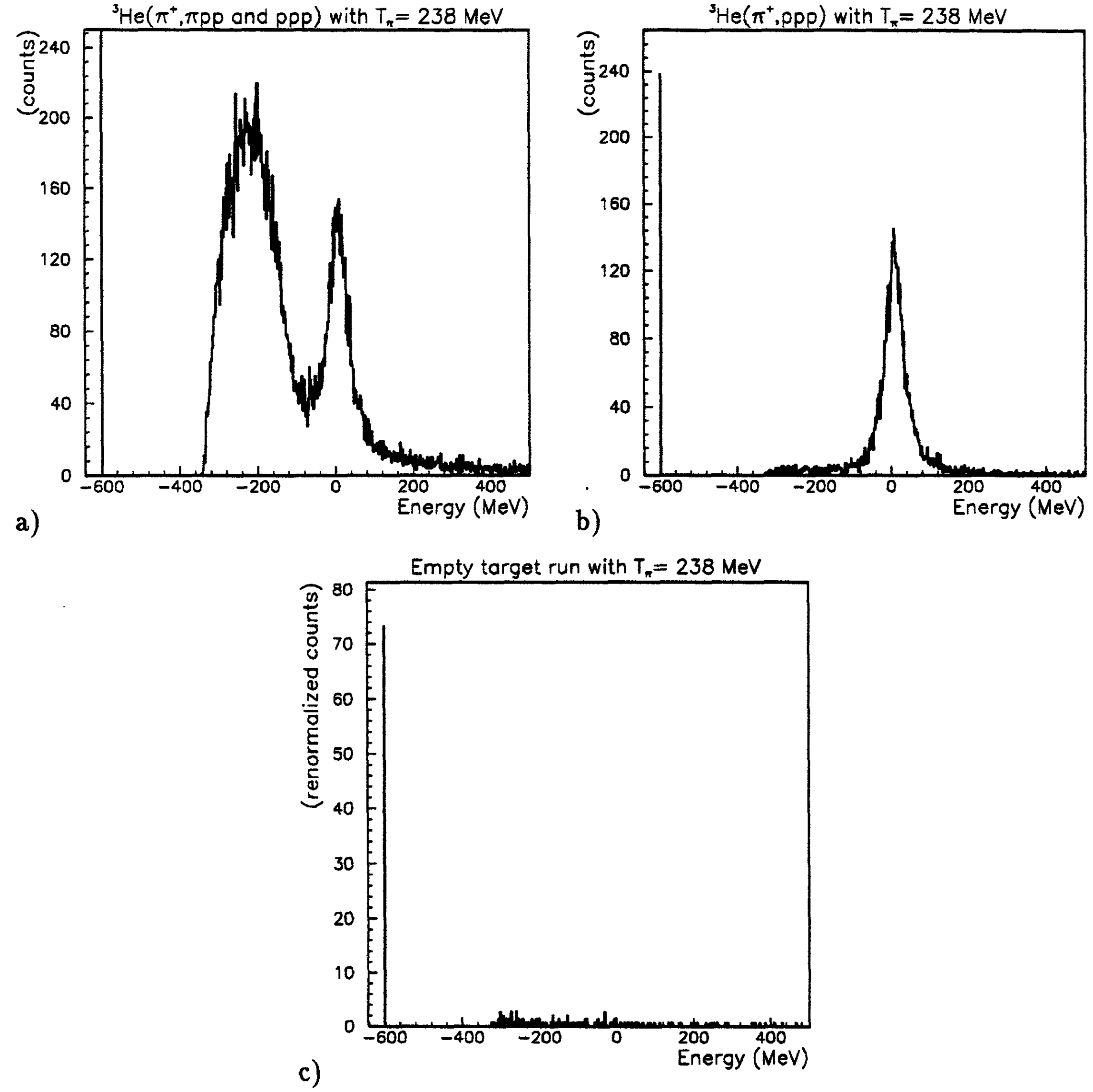

Figure 5-4: The ΔE of the event is calculated using only the MWPC's and assumes that the three final states particles are protons. In Figure a), which has only a target cut on it, the πpp peak at negative ΔE dominates. The peak at -600 MeV, which is explained in the text, is more than an order of magnitude larger than shown. Figure b) represents those events accepted by the analysis cut as part of the absorption cross section before empty target subtraction. Figure c) is an empty target run which is normalized to be directly comparable to Figure b).

5.3 Uncertainty of the Absorption Yield

5.3.1 Uncertainties in the Determination of Reaction Corrections

Section 4.3.1 described how a set of absorption events was filtered using only the MWPC information. In the measurement of the reaction correction, it was assumed that the two-proton events in ^{2}H filtered in this way had no pion background. While it is theoretically possible because of the Fermi momentum for the πp final state in ^{2}H to be back-to-back, it is highly unlikely. It was possible to look at the summed light of the events filtered using only the MWPC information and to set an upper limit on the pion contamination. If the data had been contaminated by pions, a peak in the kinematic region of πp, much like the peak seen in Figure 4-8, would be observed. The lack of any discernable peak in the spectrum at the incident pion kinetic energy allowed the reaction correction for ^{2}H to be specified to better than 0.5%.

The ^{3}He reaction correction for two detected protons was performed in the same manner as in ^{2}H, except for a small adjustment to take into the account the difference in binding energy between ^{2}H and ^{3}He. This adjustment was done by moving the cut on the total summed light in the ^{2}H data 8 MeV higher in energy, to account for the fact that the absorption peak in ^{3}He is about 8 MeV lower in energy. To test this procedure, the energy cut was moved by a further 15 MeV, and this change affected the cross section by only 2% because there are relatively few events in the region of the energy cut. This value of 2% was used as the magnitude of the uncertainty for the ^{3}He two detected proton reaction correction.

Pion contamination affected the determination of the reaction correction for the events with three detected protons to a greater extent than for those with two detected protons. In the data which was separated out using the energy difference (ΔE), the runs with beam energies of T_π = 162 MeV and 239 MeV had clearly evident pion peaks corresponding to the incident pion kinetic energy. See Figure 4-8. This pion contamination was measured using an exponential fit to the data and found to be 1%, 5%, and 11% at beam energies of 118, 162, and 239 MeV. The accuracies of these fits were estimated to be .5%, 1.5%, and 3% respectively. These uncertainty estimates are large enough to account for the inaccuracy of the phenomenological nature of the model and the uncertainty of the fit.

T_π (MeV) ^{2}H	Systematic Error of the MWPC Efficiency for ^{2}H					
	2C		3C			
	$\eta_{(2,0)}$	$\eta_{(1,1)}$	$\eta_{(2,0)}$	$\eta_{(3,0)}$	$\eta_{(2,1)}$	$\eta_{(1,2)}$
116	0.01	0.03	0.02	–	–	–
162	0.01	0.03	0.02	–	–	–
240	0.01	0.06	0.02	–	–	–
^{3}He	Systematic Error of the MWPC Efficiency for ^{3}He					
116	0.01	0.03	0.02	0.015	0.015	0.03
162	0.01	0.03	0.02	0.015	0.015	0.03
240	0.01	0.03	0.02	0.015	0.015	0.03

Table 5.5: This is a list of the systematic uncertainties for the MWPC efficiencies given in Table 4.5. 2C and 3C represent the trigger while the ordered pair (i,j) give the geometry of the event. i and j are the number of protons that stop in the cylinder and endcap respectively.

5.3.2 Systematic Uncertainties in the Measurement of the MWPC Efficiencies

The MWPC exhibited nearly constant efficiency during the run. The Table 4.4 single particle efficiencies for the inner and outer chambers, combined with the 2C $\eta_{(2,0)}$ efficiencies shown in Table 4.5, give strong evidence that the chambers were working well during the experimental runs that were analyzed.

Because of the different relative angular distributions represented by the different energies, targets, and event types, there is no *a priori* reason to expect the η's in Table 4.5 to be equal. However, it is reasonable to expect that η's representing similar angular distributions to be similar, and that is indeed what is observed. For example, the 2C $\eta_{(2,0)}$ in ^{3}He is within 1% of the 2C $\eta_{(2,0)}$ in ^{2}H at each beam energy. Sufficient reason to expect the η's not to be exactly equal is given by the spectator nucleon in ^{3}He, which spreads out the correlation of the two protons. However, other explanations for the differences are possible. To be conservative, a systematic error of 1% was assigned to 2C $\eta_{(2,0)}$. Similar comparison of the 2C $\eta_{(1,1)}$ and 3C $\eta_{(2,0)}$ in ^{2}H and ^{3}He was used to estimate their systematic errors. Because there was little data at 239 MeV on ^{2}H for the 2C $\eta_{(1,1)}$, a systematic error of approximately twice that of the other energies was assigned.

A similar method was used in estimating the systematic uncertainty when three protons were detected. Again there is no *a priori* reason for the different energies to have exactly the same η's. However, the η's for each class of events are remarkably similar. Whether the differences are due to the differences in the relative angular distributions of the particles, or to some other cause, is an open question. Again, to be conservative, the differences between the η's at different energies were used to estimate the systematic uncertainty.

5.3.3 Uncertainties in the Determination of the Number of Protons in the Final State

As stated in Section 5.2, it is possible for a particle to have a reaction which alters its trajectory such that it passes into another sector's ΔE and through the outer MWPC in front of that ΔE. This type of trajectory would have caused some of the two-proton events to be counted as three-proton events. The size of this effect can be estimated from the three-proton part of the ^{2}H data, where there can only be two protons in the final state, if the background subtraction is done accurately. See Section 5.1.2. The amounts of three-proton events in ^{2}H are $0.3 \pm 0.3\%$, $0.9 \pm 0.3\%$, and $1.2 \pm 0.4\%$ at 118, 162, and 239 MeV incident pion energies, respectively.

Since ^{3}He$(\pi^+, pp)p$ has a very similar distribution in energy and angle to absorption on ^{2}H, the percentages of two-proton cross section incorrectly counted as three-proton events are considered to be the same. In ^{2}H, the three-proton events are simply included in the total cross section. In ^{3}He, the percentages found in ^{2}H at each energy are used to correct the two- and three-detected-proton cross sections. The two-proton cross section is increased by these percentages, and the three-proton cross section is decreased by the appropriate amount. The small amount of four-detected-proton events found in ^{3}He are simply added to the three-proton cross section.

5.4 Uncertainties in the Beam Normalization

The five corrections needed to normalize the beam scaler are given in Table 4.6. The dominant corrections are $f_{Sbeam\ cut}$ and f_{miss}. Both of these corrections were measured with the data. The other three corrections were calculated analytically.

$f_{Sbeam\ cut}$ is well-determined, except for its statistical uncertainty, which is given in the table. f_{miss} is well-determined except that the model used for the beam spreading was linear, ie. a simple average of the beam outside the target radius before and after the target. Since the differences are small (see Table 5.1), this procedure does not introduce much uncertainty. Nevertheless, 10% of the size of f_{miss} was assigned as a measure of the systematic error of f_{miss}.

The uncertainty in f_{decay} is dominated by the distance from $\mathrm{S_{beam}}$ to the center of the target, which is known to better than 5%. Therefore, the uncertainty of f_{decay} is of the order of .05*f_{decay}, which is small enough to ignore.

The uncertainty in f_{react} is due to the uncertainty of the material in the path of the beam and the uncertainty in the relevant nuclear cross sections. The amount of material in the beam is known to better than 10%, and the nuclear cross sections to better than 25%. Therefore f_{react} was assigned a systematic error of 30%. This value was always less than 0.007.

The systematic uncertainty in f_{contam} is more difficult to estimate. It depends on the adequacy of the model of the πM1 channel and how accurately the model reflects the experimental setup. There are experimental measurements for N_{μ^-}/N_{π^-} at 165 MeV which find the ratio of .015 at the SUSI pivot point [47]. Since the N_{μ^+}/N_{π^+} should be the same, if we allow for the extra decay between the SUSI pivot point and $\mathrm{S_{beam}}$, we expect $f_{contam} = .019$. The calculation using TURTLE gives $f_{contam} = .018$. It is also possible to use TURTLE to explore the sensitivity of f_{contam} to the beam tune. Changing various magnets within reasonable ranges produces a variation of f_{contam} of the order of .005. To be conservative, f_{contam} was assigned an uncertainty of ±0.01.

5.5 Uncertainties in the Thickness of the Target

The length of active target was given by the vertex cut in z, determined using the MWPC. To ascertain that the MWPC accurately measured distance, the distance between the target entrance and exit windows was measured using the MWPC and found to be 25.6 cm (see Figure 4-1). The distance between the target windows was also measured with vernier calipers and found to be 25.7 cm. This measurement indicates that the accuracy of the MWPC in defining the target length was better than 1%.

The uncertainty in the density of the target is determined from the uncertainties in the pressure and temperature. The pressure gauge was checked to be accurate to better than 0.1%. The temperature was checked in several places using thermo-couples. Because of the heat from the photomultiplier tube bases, the inside of the detector was about 31 degrees Celsius. The temperature readings varied by a few degrees, depending on where the sensors were placed and the temperature outdoors. One sensor was kept close to the target and was checked at the beginning of each run. This sensor was used in the calculation of the target density. However, because of the temperature gradients present, an uncertainty of 3° Celsius was assigned to the temperature. These uncertainties in pressure and temperature yield an uncertainty in the target density of 1%.

5.6 Uncertainties in Calculating the Acceptance of LADS

The uncertainty in the acceptance calculation primarily affected the division of the total ^{3}He cross section into its 2NA and 3NA components and had little effect on the total absorption cross sections in both ^{2}H and ^{3}He. This is because LADS covers nearly all of phase space and the size of the extrapolations for the total cross sections was under 15% at all three energies for both nuclei. Since these corrections are small, the determination of the total cross section is largely model independent. The determination of the partial cross sections for 2NA and 3NA in ^{3}He is more strongly model dependent and is also much more sensitive to the accurate modeling of the thresholds and geometry of the LADS detector by the Monte Carlo code.

The systematic uncertainties in the ^{3}He cross sections do not include any uncertainty associated with the possibility that absorption is not dominated by quasi-free absorption on a $T = 0$ pair and a phase-space like three nucleon absorption mechanism. In the next chapter it will be shown that this model seems justified by the data, particularly with respect to the energy of the final state protons. This justification is important because the breakup into 2NA and 3NA is particularly sensitive to the energy of the protons, whereas it is relatively insensitive to the angular distribution of the protons in the final state because of the almost complete angular coverage of the detector.

The systematic uncertainty of all the cross sections was estimated by making changes to the Monte Carlo that reflected the uncertainties of the geometry and thresholds of LADS, as well as reasonable variations in the implementation of the models.

Systematic Uncertainty Due to Material in LADS				
Target	Energy	Change in Cross Section		
		2NA	3NA	Total
^{3}He	118	1.9%	6.1%	0.1%
^{3}He	162	2.1%	4.7%	0.1%
^{3}He	239	2.1%	5.1%	0.1%

Table 5.6: The change in the integrated cross sections due to the removal of approximately one-half of the inner MWPC, which represents 25.12 mg/cm^2 composed of a variety of materials.

5.6.1 Uncertainty in the Thresholds

The detector threshold was determined by the energy lost in the material between the pion-nucleus interaction point and the scintillator together with the amount of energy a proton had to deposit in the scintillator to be above the electronic threshold. In addition, the effect of straggling for protons undergoing very large energy losses was included. The threshold was only important for the ^{3}He models, since in ^{2}H absorption all protons have a high enough energy to be well above threshold.

All the material between the pion interaction point and scintillator was put into the Monte Carlo code, which then calculated the energy loss of the particle. This material included the target gas, target walls, inner and outer MWPC's, the scintillator wrapping, and the air inside the detector. The uncertainties for the thicknesses of these elements are given in Table 2.3. The total amount of material is 275 ± 25 mg/cm^2 measured perpendicularly from the beam axis to the scintillator. Most of the material in the beam was carbon or a carbon compound. To estimate the effect of the uncertainty in the material thickness, two things were done. First, a carbon cylinder 25 mg/cm^2 thick was inserted into the code right after the target. The second test was the removal of the first half of the inner chamber, from the grounding foil through the MWPC gas for a total thickness of 25.12 mg/cm^2 of a variety of materials. The latter technique produced the largest change in the cross section, so it was the one used to estimate the size of the uncertainty in the cross section.

Saturation of the scintillator response occurs for protons at the end of their range. A proton of 2.1 MeV produces light in plastic scintillator equivalent to a 0.6 MeV energy loss for a minimum ionizing particle [49]. A proton of 2.6 MeV produces light corresponding to 0.8 MeV energy loss for a minimum ionizing particle. The threshold of the DE's in LADS was set

Systematic Uncertainty Due to the Electronic Threshold for Protons in LADS				
Target	Energy	Change in Cross Section		
		2NA	3NA	Total
^{3}He	118	0.1%	0.5%	0.0%
^{3}He	162	0.1%	0.4%	0.0%
^{3}He	239	0.1%	0.7%	0.0%

Table 5.7: Affect of changing the threshold for detection of protons by the plastic scintillator by ±0.5 MeV.

low enough to have a nearly 100% efficiency for minimum ionizing particles normally incident on the scintillator. These particles would have a mean energy loss in the DE's of 1 MeV, but because of Landau broadening the FWHM of the peak is of the order of 0.2 MeV and the modal energy loss is somewhat less than 1 MeV. These facts imply that the electronic threshold was no higher than 0.8 MeV for minimum ionizing particles. The threshold was also not less than 0.4 MeV for minimum ionizing particles, as this would not have been sufficiently above the noise level of the electronics. Therefore, a proton threshold energy of 2.1 ± .5 MeV is a reasonable assumption. Table 5.7 shows that the cross sections were not sensitive to this threshold.

Straggling was done for those protons near threshold by converting the mean energy loss to the modal energy loss after the particle had lost $\approx 80\%$ of its energy. The particle's energy was then modified by a random amount whose probability of occurrence was found using the skewed distribution and FWHM prescribed by C. Tschalär's article [58]. The particle was then propagated through the rest of the material using the mean energy loss as determined by the range tables until it reached the scintillator. Adding straggling in this way had no measurable effect on the cross sections.

5.6.2 Uncertainty in the Geometry

The geometrical acceptance of LADS depended on the outer and inner radii of the endcap DE's. The outer radius was important because of the requirement in the analysis that at least one proton be in the cylinder part of the detector. The inner radius was important because it determined the size of the beam entrance and exit holes where particles could escape the detector without being detected. These radii were specified as 25.8 ± 1.0 cm for the outer endcap radius, and 8.80 ± 0.5 cm for the inner endcap radius.

Change in the Cross Section Due to Radius of Endcap							
Target	Energy	Outer Radius			Inner Radius		
		2NA	3NA	Total	2NA	3NA	Total
^{2}H	118	–	–	1.1%	–	–	0.0%
^{2}H	162	–	–	0.9%	–	–	0.0%
^{2}H	239	–	–	0.7%	–	–	0.0%
^{3}He	118	0.9%	0.0%	0.7%	0.2%	0.7%	0.3%
^{3}He	162	0.9%	0.1%	0.6%	0.2%	0.7%	0.4%
^{3}He	239	0.9%	0.7%	0.4%	0.0%	1.4%	0.5%

Table 5.8: The geometrical acceptance of the detector was dependent on both the inner and outer radius of the endcaps. The two columns represent a change in radius of 1 cm for the outer radius and 0.5 cm for the inner radius.

The ^{2}H absorption cross section did not depend on the inner endcap radius. This insensitivity to the inner radius was because the two protons were back-to-back in the center of mass frame, and the requirement that one proton be in the cylinder meant that the other proton could not escape the detector through the beam entrance or exit holes.

5.6.3 Uncertainty in the Implementation of the ^{2}H absorption model

The differential absorption cross section in ^{2}H has been comprehensively measured by previous experiments and is well described by the Ritchie parameterization of the Legendre polynomials [8]. To allow for the uncertainty of this parameterization, the ratio of A_0/A_2 was varied by 10%.

5.6.4 Uncertainty in the Implementation of the 2NA model

In the Δ-resonance region there is much evidence that the two-nucleon absorption is dominated by absorption on $T = 0$ pairs within the nucleus [15, 16]. The angular distribution of the absorbing pair in the final state is similar to that of ^{2}H(π^+, pp)[28, 29] and is dominated by the formation of a Δ in an intermediate state [33]. In this classical picture of the 2NA mechanism, the third nucleon is by definition a spectator proton and has the same momentum and energy in the final state as it had in the initial state. In this picture, it is assumed that the spectator proton is on its mass shell; otherwise it must interact with the other particles to get back on the

Effect of Changing A_0/A_2 by 10%				
Energy (MeV)	Target	Change in the Cross Section		
		2NA	3NA	Total
118	^{2}H	–	–	1.0%
162	^{2}H	–	–	1.0%
239	^{2}H	–	–	0.7%
118	^{3}He	1.0%	0.1%	0.7%
162	^{3}He	0.9%	0.1%	0.6%
239	^{3}He	0.7%	0.3%	0.5%

Table 5.9: This shows how the cross section changes if the ratio of the coefficient of the Legendre Polynomials (A_0/A_2) is varied by 10% in the Monte Carlo program that models the acceptance.

mass shell and thus in some way take part in the interaction. If the spectator proton interacted with the absorbing pair, this situation would be considered 3NA. Therefore, all of the off-shell nature of the nucleus must be assigned to the absorbing pair.

Thus in the model it is assumed that the absorbing pair is a $T = 0$ pair, that the pair has a final state angular distribution similar to ^{2}H(π^+, pp)and proceeds by the formation of a Δ, and that the absorbing pair contains all of the off-shell character of the nucleons in the ^{3}He nucleus.

5.6.4.1 Angular Distribution of the Absorbing Pair

The 2NA mechanism used the Ritchie parameterization to weight the energy and the angle of the absorbing pair, as described in Section 4.6.1. The total energy of the πd system was allowed to vary, and the formation of a Δ in the intermediate state was modeled using the shape of the total absorption cross section in ^{2}H(π^+, pp).

The geometrical acceptance of the detector to 2NA was dependent on the Legendre coefficients calculated from the Ritchie parameterization. To check the sensitivity of the results to these Legendre coefficients, A_2/A_0 was varied by 10% in the Monte Carlo simulation. This variation produced changes in the cross sections of 1% or less.

5.6.4.2 Various Choices for the Spectator Momentum

The ^{3}He wavefunction is well modeled, as the Faddeev equations can be solved exactly for a given Hamiltonian. This technology has progressed to the point where there is good agreement between the various groups [23]. However, especially because ^{3}He is a three-body system, the momentum of the spectator proton is dependent on the initial state of the absorbing pair. The $T = 0$ constraint is not enough to specify the absorbing pair's initial state, as the momentum, energy, spin and angular momentum of the pair remains unspecified. Assumptions about the initial state of the absorbing pair can dramatically affect the spectator momentum distribution even when the ground state wavefunction is well known.

The spectator momentum is often expressed as $N(p)$, with subscripts added to N to indicate whether the spectator momentum is for the proton or neutron and whether any restrictions have been placed on the other pair of nucleons. The model does not depend on the magnitude of $N(p)$, but only on its shape, since $\int_0^{p_{max}} N(p)dp = 1$ must be normalized to unity to represent a probability distribution of the spectator momentum.

There are two extreme assumptions which can be made about the absorbing pair that can also be related to $(e, e'p)$ experiments. One is to assume that the 2NA mechanism does not favor any particular quantum state for the absorbing pair. This assumption implies that the momentum distribution of the spectator should be the same as the momentum distribution of one of the protons in the ^{3}He ground state wavefunction. This momentum distribution can be projected out from the ground state wavefunction and compared to the experimental measurement of ^{3}He$(e, e'p)$. In the low momentum region, theory and experiment agree quite closely, but the experimental data is lower than the theory at higher p. This disagreement has been explained by the fact that ^{3}He$(e, e'p)$ measurements contain final state interactions and the exchange of particles in the final state, both of which lie outside our model of two-nucleon pion absorption. The theoretical curve is therefore likely a more realistic representation of the spectator momentum distribution for the present purposes. The second assumption is that the absorbing pair is a real deuteron. This assumption is comparable to measurements using ^{3}He$(e, e'p)d$ experiments. The theoretical calculation is done by taking the overlap of the ^{3}He wavefunction with a real deuteron and a proton in a plane wave state.

Neither of the above assumptions is a particularly good match to the model of the absorbing pair specified earlier. The first does not take into account the $T = 0$ nature of the absorption, and the second puts unrealistic restrictions on the energy, momentum, spin, and angular momentum of the absorbing pair. Ishikawa and Wu did a calculation where the absorbing pair was

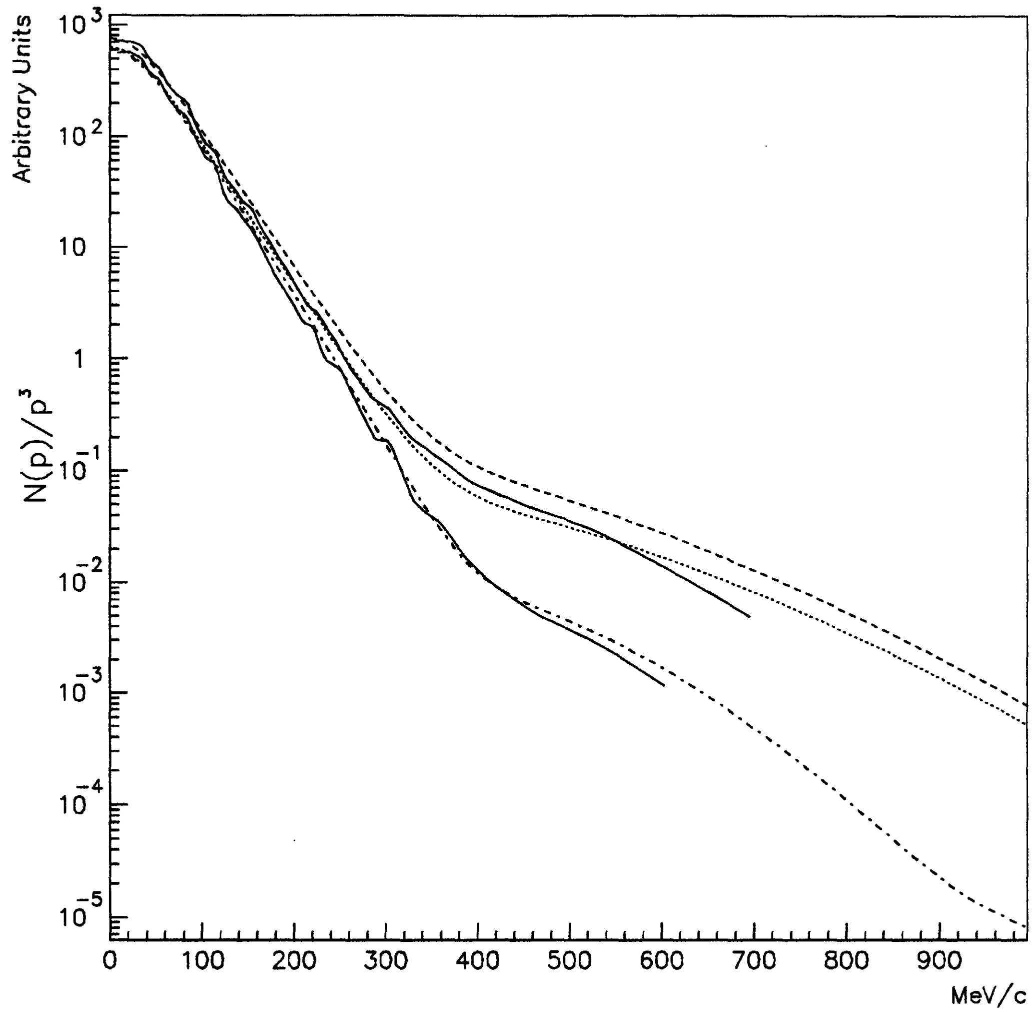

Figure 5-5: $N(p)$ represents the probability that the spectator proton has momentum p. The solid lines are data from ^{3}He$(e,e'p)$, the lower solid line is ^{3}He$(e,e'p)d$, and the upper is ^{3}He$(e,e'p)$ [62, 63]. The dotted and dashed lines are from Faddeev calculations of the ^{3}He wavefunction [26, 60]. $N_{pd}(p)$,$N_p(p)$, and $N_{p,T=0}(p)$ are the dot-dashed line, the dashed line, and the dotted line, respectively.

Change in the Cross Section for Different Spectator Momentum Probability Densities in ^{3}He									
Energy	$N_p(k)$			$N_{pd}(k)$			$N_{p,T=0}(k)$		
(MeV)	2NA	3NA	Total	2NA	3NA	Total	2NA	3NA	Total
118	+1.5%	−6.1%	+0.1%	−1.5%	+6.1%	−0.1%	+0.4%	−1.3%	0.0%
162	+2.4%	−5.4%	+0.1%	−2.4%	+5.4%	−0.1%	+0.5%	−1.4%	0.0%
239	+5.6%	−11.8%	+0.2%	−5.6%	+11.8%	−0.2%	+1.4%	−3.7%	0.0%

Table 5.10: From this table it is possible to calculate the change in the cross section given a specific momentum distribution. $N_p(k)$, $N_{pd}(k)$ and $N_{p,T=0}(k)$ represent the momentum distribution for the spectator for the following three cases: there is no restriction on the absorbing pair, the absorbing pair is a real deuteron, and the absorbing pair is restricted only to be $T = 0$, respectively. The momentum distributions are calculated using the ^{3}He wavefunction of Ishikawa *et al.* with three-body forces.

only restricted to be $T = 0$ [60]. The shape of $N_{p,T=0}(p)$ is intermediate to that of $N_p(p)$ and $N_{pd}(p)$, though it is closest to $N_p(p)$. The momentum distribution from this calculation would be the appropriate spectator momentum to use, if it was known that the other variables had no influence on the Δ formation and subsequent de-excitation of the Δ back into a nucleon. However, it seems highly improbable that these variables do not affect the cross section.

To reflect the uncertainty of the initial state of the absorbing pair, the two extreme distributions, $N_p(p)$ and $N_{pd}(p)$ from Ishikawa *et al.* with three-body forces, were used. The average of the two results for the integrated cross sections are quoted and the uncertainty attributed to this part of the model was made just large enough to incorporate both momentum distributions. These uncertainties were among the largest contributors to the uncertainty of the breakup of the total cross section into 2NA and 3NA cross sections. The percentage uncertainty was largest for the 3NA cross section, contributing uncertainties of 6.1%, 5.4%, and 11.8% at 118, 162, and 239 MeV, respectively. The size of the contribution of these uncertainties to the 2NA and total cross section are shown in Table 5.10.

5.6.5 Uncertainty in the Implementation of the 3NA model

Three-nucleon absorption was modeled with three-body phase space. As with previous experiments, it was assumed that the phase space was isotropic. Since the 3NA model is well specified, no systematic error was assigned to represent the possibility that 3NA might be non-isotropic.

It may be that the 3NA process occurs when the angular momentum of the pion is not $L = 0$; this would lead to a non-isotropic angular distribution of the final state protons in the center of mass system. However, an initial pion state of $L > 0$ would not effect the energy distribution of the protons in the center of mass system [64, 65, 66]. Because of the large angular acceptance of LADS, the results should be relatively insensitive to the assumption of isotropy of the 3NA mechanism. (See also Section 6.6).

5.7 Miscellaneous Uncertainties

There were various other possible sources of uncertainties that were also checked.

One is the possibility of the scalers double counting or being inefficient. The scalers were tested before the experiment and monitored during the experiment by putting the critical scalers in more than one module. No significant discrepancies between the different identical scalers were observed during the runs that were analyzed.

Another possible source of error that was checked was the exclusivity of the trigger types. For instance if a single event was counted as both a 2C0N trigger and a 3C trigger, one could have a problem with the normalization of the experiment. This double counting was indeed observed, but at a very low level (less than 0.1%). This value was too small to affect the experiment and was diagnosed as coming from events with very peculiar timing, most likely associated with extraneous beam particles in coincidence with a pion.

Another problem was the software reconstruction of pathological events. Some events were aborted by the CTP software because they were too bizarre geometrically to analyze. For example, the software did not handle the case when four or more adjacent cylinder E-blocks reported signals. The number of CTP aborts was quantified, and it was demonstrated that an upper limit of 1% of absorption events could have been aborted because of these strange geometries. This 1% was unlikely to be absorption, but it could not be firmly ruled out. Since other errors dominated, it was ignored.

Finally, it was assumed in the analysis that the ADC's and TDC's were 100% efficient. This is a reasonable assumption given our relatively low singles rate. The TDC's were specifically tested, and for absorption events the TDC information was always there. Note that inefficiencies of ADC's and TDC's in the E-blocks would have been corrected for with the reaction correction of Section 4.3.1, since this correction used data filtered out using only the MWPC's and dE's.

Chapter 6

Results and Conclusions

This chapter will present LADS's high-statistics, large phase space measurements of pion absorption on ^{3}He. These measurements are unique and important because of the large acceptance of the detector. This means the extrapolations over unmeasured phase space are small, and that several new kinematic variables could be examined.

Previous experiments have already established that the pion absorption process can be separated into two types of interactions with ^{3}He: one in which only two of the three nucleons are directly involved in the interaction, and one in which all three nucleons take part in some way in the interaction. The final states of these processes cannot be separated on an event by event basis; however, in aggregate they have different and distinct characteristics. The division of the absorption process into these two classes is inherently model dependent, which is complicated by the fact that a realistic model for 3NA is a matter of current debate. For the total cross section, we can use LADS's large acceptance to make a relatively model independent measurement. We will attempt to quantify the size of the 2NA and 3NA processes using our model. We will also look at differential quantities, some that are in agreement, and some that are in disagreement with the model. Fortunately, the differential quantities that vary from our model are in the angular distributions of the final state protons. The large angular acceptance of the detector minimizes the influence of these deviations from the model when the model is used to divide the total cross section into 2NA and 3NA integrated cross sections. However, the deviations from three-body phase space that we see contain information about the mechanism(s) responsible for the 3NA process and can hopefully be used to gain an understanding of 3NA.

6.1 Justification of the 2NA and 3NA Model

While the total absorption cross section is relatively insensitive to the model used to extrapolate over the small unmeasured regions, the breakup of the cross section into 2NA and 3NA integrated cross sections was more sensitive to the model. The model used can be justified both from previous experiments and from LADS data.

Previous experiments of pion absorption on ^{3}He in the energy region around the Δ-resonance have provided evidence that a large part of the pion absorption cross section can be attributed to a 2NA mechanism which has angular and energy distributions similar to those of pion absorption on ^{2}H [27, 29, 28, 31]. These experiments detected two energetic protons whose $d\sigma/d\Omega$ in the π–d center of mass system was symmetric around 90° and could be well fit using Legendre polynomials of the zeroth and second order. These experiments lacked the angular coverage necessary to determine whether a fourth or higher order Legendre polynomial term was necessary. However, the ratios of the Legendre polynomial coefficients A_2/A_0 measured on ^{3}He were similar to the ratios measured on ^{2}H. These experiments also looked at the energy distribution of the undetected proton in ^{3}He. At low energies, the shape of the distribution was consistent with the undetected proton being a spectator in the reaction and having a final state energy which was the same as its Fermi energy inside the nucleus.

While 2NA is the largest part of the absorption cross section, previous experiments have found evidence for a 3NA mechanism with a size of 15–40% of the total absorption cross section. The energy distribution of the protons originating from this 3NA mechanism seemed to have a phase space distribution. However, the most convincing evidence for this conclusion is the result of an experiment at $T_\pi = 119$ MeV that had measurements at seven different regions of phase space. Each of the seven measurements in this experiment subtended on average $\approx 0.14\%$ of three-nucleon phase space [55]. Furthermore, these seven measurements were "in-plane" *i.e.* limited to the portion of phase space where the final state protons were in a plane containing the incident pion. That experiment saw no statistically significant deviation in the angular distribution of the protons from that of three-nucleon phase space. Other in-plane experiments [27, 31], both below and above the Δ-resonance and with somewhat less phase-space coverage, also found a phase space distribution in the energy of the outgoing protons; however, these experiments saw variations from phase space in the angular distributions of the protons.

The model of pion absorption used in the present analysis was based on the above observations. This model consists of a 2NA mechanism, based on absorption on a "quasi-deuteron" pair with a spectator proton that has a Fermi momentum distribution, and a 3NA mechanism consisting of an isotropic three-body phase space distribution. (For a more thorough description see Sections 4.6.1 and 5.6.) The possible deviations from isotropic three-nucleon phase space seen in some (but not all) experiments were not included in the model. However, because our separation into 2NA and 3NA is based primarily on the energy distributions of the protons, and because LADS's large angular coverage minimizes the extrapolations over angles, the breakup into 2NA and 3NA cross sections is not very sensitive to variations in the angular distribution of the protons. The uncertainty due to possible angular variation from isotropic three-body phase space is not included in the present results uncertainty.

The model used to extract the integrated cross sections can be tested by comparing it to some of the differential quantities measured using LADS. A test of the 2NA mechanism contained in the model can be performed by comparing the $d\sigma/d\Omega$ the model generates to the $d\sigma/d\Omega$ measured by LADS when exactly two high energy protons were detected. Under these conditions, $d\sigma/d\Omega$ is symmetric in the π–d center of mass system and can be fit with the even terms of a Legendre polynomial. The model's ratios of the coefficients of these Legendre polynomial fits can be compared to that obtained from the data.

Though Chapter 4 describes fully all of the cuts that were used for the integrated cross sections reported in Sections 6.2 through 6.5, a few additional cuts were needed before the $d\sigma_{2NA}/d\Omega$ measured by LADS could be fit to a Legendre polynomial. Any pion contamination could affect the shape of the distribution, causing it to be asymmetric and producing too much strength at forward angles. This contamination would be difficult to correct for, so a much tighter cut was placed on the total energy of the charged particles in Figure 4-7 to ensure that there were no pions left. To remove the dependence of the energy threshold on the outgoing proton's direction and to ensure that the angular distribution would be less affected by the detection of the spectator proton in a 2NA process, a 30 MeV threshold was set in the software so that there would be a constant and rather high threshold over the entire detector. Protons which were below this threshold were not counted as "detected." These two cuts required a larger reaction correction, which was determined using the methods described in Section 4.3.1. In addition to these cuts, it was necessary to require that neither of the two protons that were above threshold hit the endcaps of the detector. This requirement was necessary because the cylinder region of the detector has a much better angular resolution, since each proton goes through two MWPC's. This restriction of not allowing protons in the endcap also avoided a problem of overlapping cathode strips on the outer chamber. For particles that are back-to-back and have center of mass angles θ of about 32° and 148°, the protons hit the same cathode strips. This causes a hole in $d\sigma_{2NA}/d\Omega$ at these values, but this area is outside the acceptance when both protons are limited to in the cylinder region. The restriction of the protons to the cylinder also eliminates problems with multiple scattering of protons that first go through the endcap before entering the cylinder. Finally, to avoid the complication of less than 100% acceptance due to the extent of the target in z, $d\sigma_{2NA}/d\Omega$ could be reliably fit only in its central region. With these restrictions $d\sigma_{2NA}/d\Omega$ cannot be used to determine whether a fourth order Legendre polynomial is necessary, but it still allows qualitative comparisons to check the validity of the 2NA mechanism in our model.

Figure 6-1 shows $d\sigma/d\Omega$ for ^{3}He(π^+,pp) in the π–d center of mass system. For each event, both detected proton θ's are plotted. The data are fit well by a Legendre polynomial of the second order.

$$\frac{d\sigma}{d\Omega} = A_0 + \frac{1}{2}A_2(3\cos^2\theta - 1)\,. \tag{6.1}$$

However, the data can be fit equally well if a fourth order Legendre polynomial is included with an A_4 fixed at 1.5 times* the A_4 value found in ^{2}H(π^+,pp). This is shown by the dotted line in Figure 6-1. Including an A_4 in this way lowers both A_0 and the ratio A_2/A_0. At 120 and 165 MeV, A_0 dropped by 3% and 7%, respectively, while the ratio was reduced by 6% and 13%. The effect on the highest energy was considerably larger, with A_0 14% smaller and A_2/A_0 30% smaller. The systematic uncertainty of the fits in Figure 6-1 has not been fully investigated, a correction for contamination from 3NA has not been included, and the fits are poorly constrained because of the lack of data close to the beam axis. Nevertheless, Figure 6-1 does give qualitative support for the 2NA event generator that is in our model. The shape of the distribution is similar to that of ^{2}H(π^+,pp) [8], and the ratios of A_2/A_0 found in Figure 6-1, for the fit with $A_4 = 0$, are $0.99 \pm .07$, $1.07 \pm .10$, and $1.29 \pm .23$ at $T_\pi = 118$, 162, and 239 MeV respectively. Fits over the same region of the distribution of events generated by the 2NA generator gave $A_2/A_0 = 1.17, 1.13$, and 1.15 at $T_\pi = 118$, 162, 239 MeV respectively. The 2NA cross section calculated from these fits by multiplying A_0 by 2π† compare favorably with the cross sections which will be reported in Section 6.4. With no A_4 term included, these values tended to be slightly high. If a fourth order Legendre polynomial with the coefficient fixed at 1.5 times the A_4 from ^{2}H(π^+,pp) were added and the zeroth and second order coefficients fit to the data, the values of the cross section were equal to or slightly lower than the values reported in Section 6.4. However, because of the problems with this method discussed above and the unmeasured systematic errors, this analysis can at most lend support to the more accurate numbers of Section 6.4, which cover a much larger angular range because they do not contain any of the additional cuts described above.

---

*There are 1.5 $T = 0$ isospin pairs in ^{3}He, which is useful as a first-order estimate for the scaling of the ^{2}H cross section.

†$\sigma = \int (d\sigma/d\Omega) d\Omega = 4\pi A_0$, which is divided by two since two protons are plotted for each event.

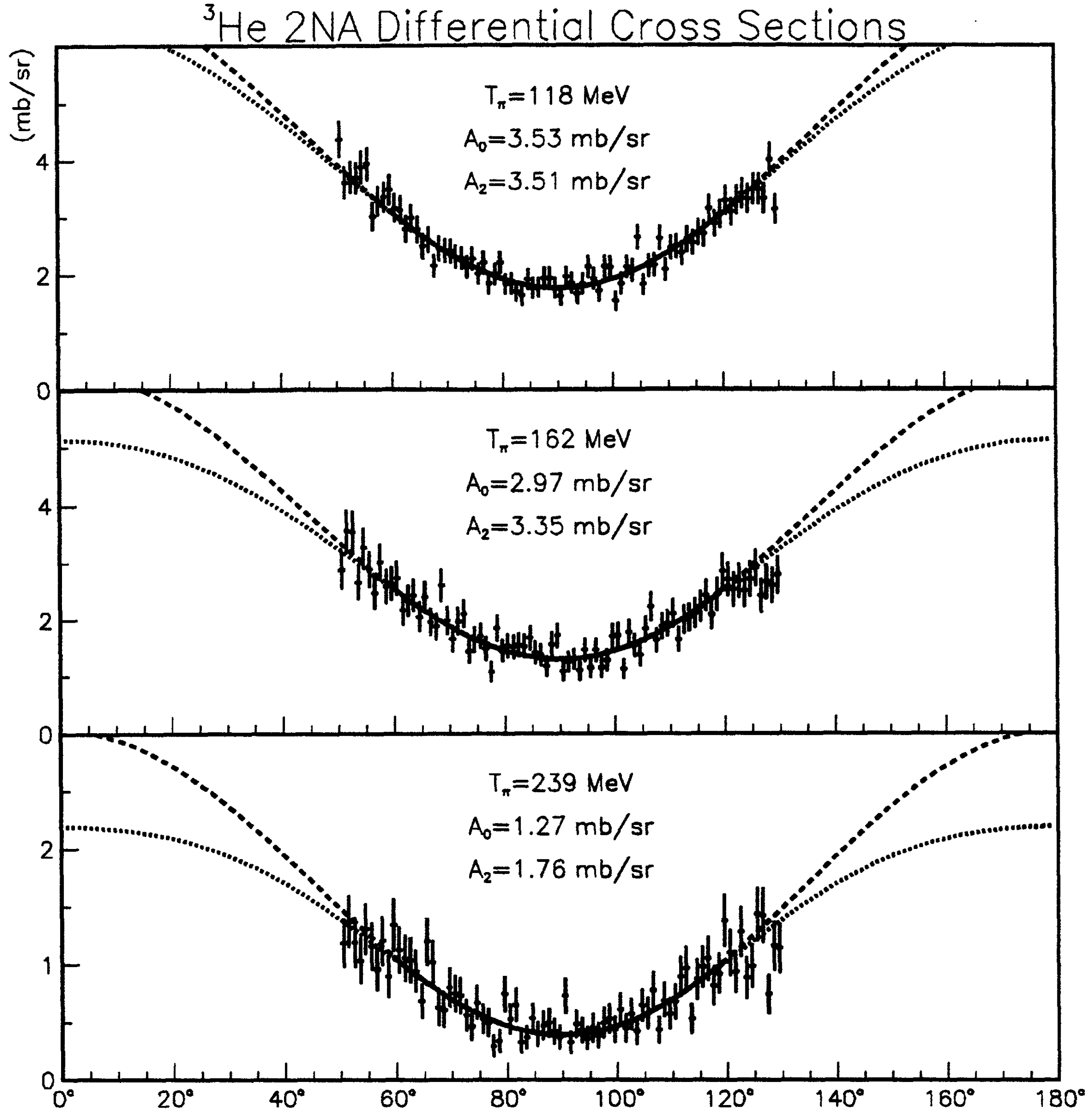

Figure 6-1: $d\sigma/d\Omega$ for π^+ absorption in the π–d center of mass system, where the cross section has been fit with zeroth and second order Legendre polynomials. The solid line shows the region of the fit and the dashed line is an extension of this fit. The dotted line is a fit which includes the fourth order Legendre polynomial term whose coefficient has been fixed at 1.5 times that found in deuterium. All of the corrections discussed in Chapter 4 have been applied except for those having to do with the acceptance of the detector, which is 100% in the region fit. Additional constraints, including the requirement that neither proton hit an endcap, are described in the text. The uncertainties are statistical.

Another test of the model's assumption about the characteristics of the 2NA and 3NA mechanisms is provided by the energy distribution of the least energetic proton. In two-nucleon absorption the spectator proton will usually be the least energetic, and its energy should be similarly distributed to the Fermi energy of a proton in ^{3}He. In three-nucleon absorption, the model predicts the energy of the least energetic proton will be determined by three-nucleon phase space.

Absorption events with both two and three detected protons were used to produce the energy distribution of the least energetic proton. When two protons were detected, the energy of the undetected proton was reconstructed by energy conservation and the least energetic of the three protons was graphed. When three protons were detected, the measured energy of the least energetic proton was ignored, and instead its energy reconstructed from the two more energetic protons using energy conservation, so that the calculation would be exactly analogous to the case of two detected protons. Since a reaction in the scintillator of one of the protons used in the reconstruction would destroy the shape of the spectrum by causing the energy of the spectator to appear to be higher than it actually was, a tight cut was placed on the invariant mass of the reconstructed proton. No attempt was made to correct for the loss of events due to this cut, as this loss would have little effect on the shape of the spectrum but would primarily affect only the overall magnitude, which in this case has been left arbitrary.

Figure 6-2 shows that the model does well in reproducing the data with respect to the energy distribution of the least energetic proton.

These two tests provide justification for using the model to extrapolate over the small regions of unmeasured phase space which are necessary for the determination of the total absorption cross section and for the use of the model to determine what amount of the cross section which is due to 2NA and to 3NA.

6.2 ^{2}H Absorption Cross Section

The ^{2}H(π^+,pp) total absorption cross section was measured at 118, 162, and 239 MeV and found to be $11.5 \pm .4$ mb, $10.9 \pm .3$ mb, and $4.2 \pm .2$ mb. As shown in Figure 6-3, these measurements are in good agreement with previous measurements of the ^{2}H(π^+,pp) absorption cross section [67, 68, 69] as well as with Ritchie's parameterization based on the world's data for this reaction below 1 GeV [8]. This agreement demonstrates that the experiment's overall

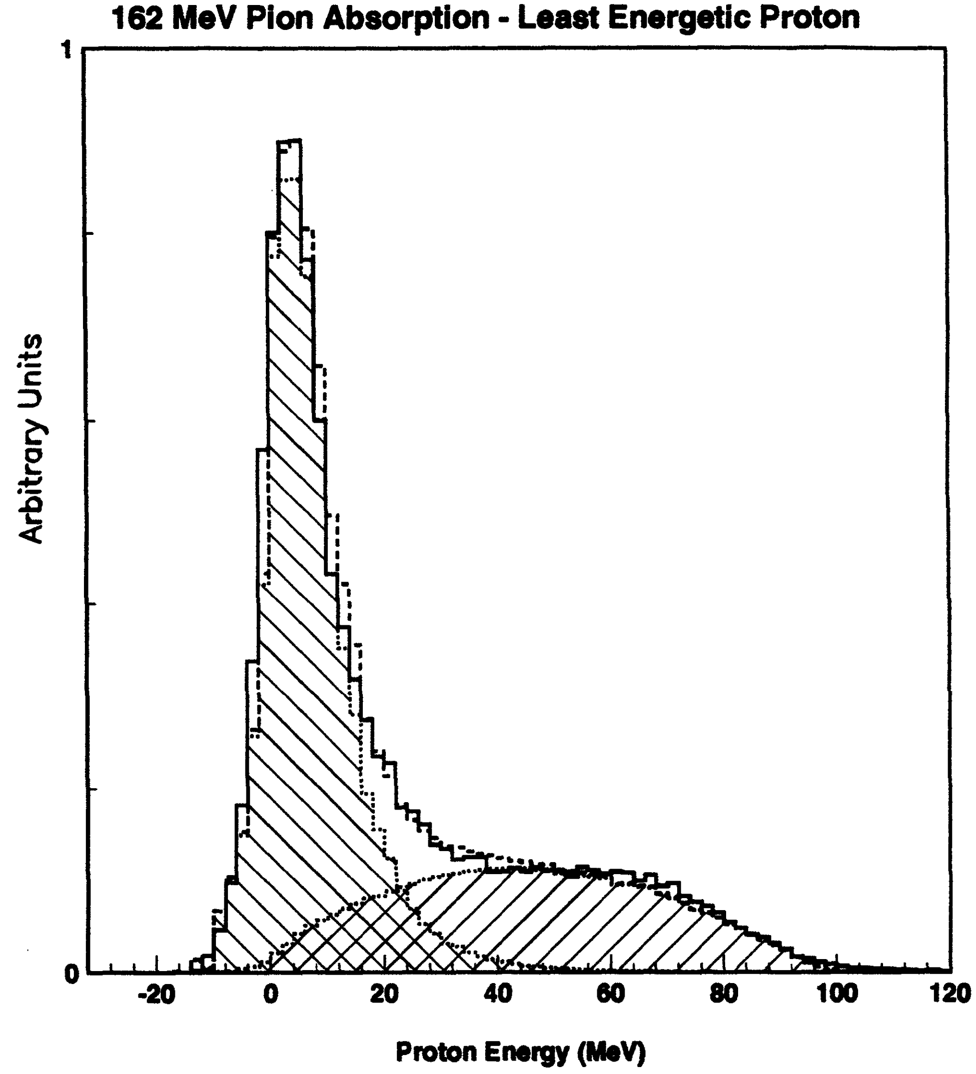

Figure 6-2: The energy of the least energetic proton after pion absorption on ^{3}He with T_π = 162 MeV. The solid line is the data. The dotted lines are from the simulations of 2NA and 3NA by the model after the application of resolution smearing and LADS's acceptance. The narrow distribution peaked at low energy was generated by the 2NA, "quasi-deuteron," part of the model while the broader energy distribution associated with 3NA is generated using three-body phase space. The dashed line is the sum of the dotted lines. The figure is reproduced here from reference [37].

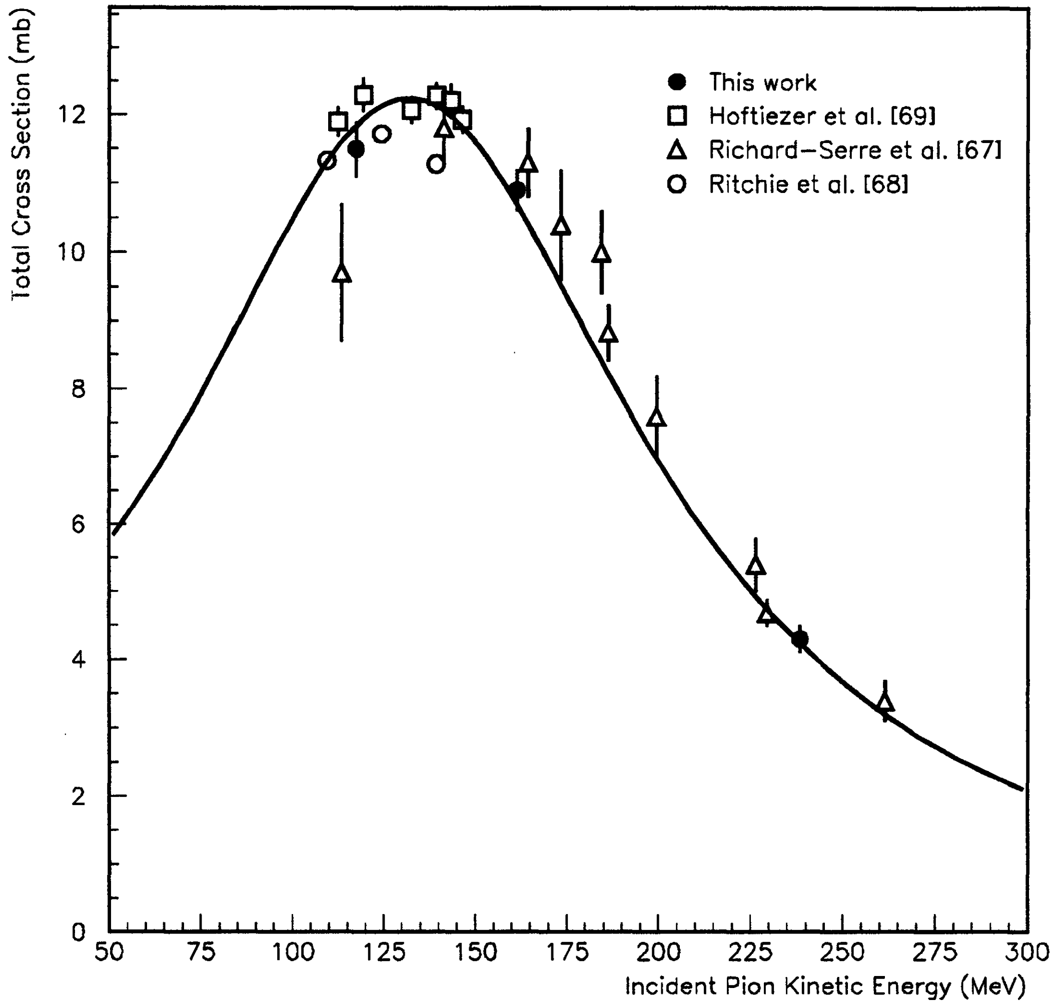

Figure 6-3: The deuterium total pion absorption cross section with data from measurements in the same energy region as that of the LADS points. The solid line is a parameterized fit to the world's data for incident pion kinetic energies less than 1 GeV [8].

π^+ Absorption on ^{3}He			
T_π (MeV)	2NA (mb)	3NA (mb)	Total (mb)
118	21.3 ± 1.0	6.0 ± 0.6	27.3 ± 0.8
162	17.4 ± 0.8	7.2 ± 0.7	24.7 ± 0.7
239	7.0 ± 0.6	3.0 ± 0.5	10.0 ± 0.4

Table 6.1: Integrated cross sections for π^+ absorption on ^{3}He. The uncertainties given include both the statistical and systematic uncertainties; the systematic uncertainties dominate. The uncertainties are larger on the 2NA and 3NA cross sections than on the total absorption cross section because the total is much less dependent on the details of the model.

normalization was correct and shows that the analysis and error estimates described in Chapters 4 and 5 were reasonable. It also shows that the geometric acceptance of the detector has been well reproduced by the Monte Carlo code.

6.3 ^{3}He Total Absorption Cross Section

The total absorption cross sections on ^{3}He are reported in Table 6.1 and shown in Figure 6-4. The uncertainty of the measurement, which includes both the statistical and systematic uncertainty, is much less than in previous experiments. The greater precision of the LADS data is due in a large part to the smaller acceptance corrections, the lower beam rates, and the extended gas target whose density and thickness could be accurately measured. Previous experiments in the Δ-resonance region [29, 30, 12, 28] had very large acceptance corrections, which contributed to their quoted error by typically 5% [29, 28]. Because of the previous experiment's lower acceptance, higher beam rates were necessary to obtain the needed statistics. These higher beam rates were frequently measured by calibrating to the ^{12}C$(\pi, \pi n)^{11}$C reaction, and the normalization uncertainty varied in the range of 5-10% [29, 28]. The measurement of a single conjugate angle per experimental setting required a thin target to prevent the uncertainty in the conjugate angle from being large. These experiments used thin liquid ^{3}He targets where the thickness and density of the target were sometimes not known to better than 6% [28].

What is not apparent in Figure 6-4 is this work's much smaller model dependence. All of the experiments use a model of a quasi-deuteron mechanism and an isotropic three-body phase

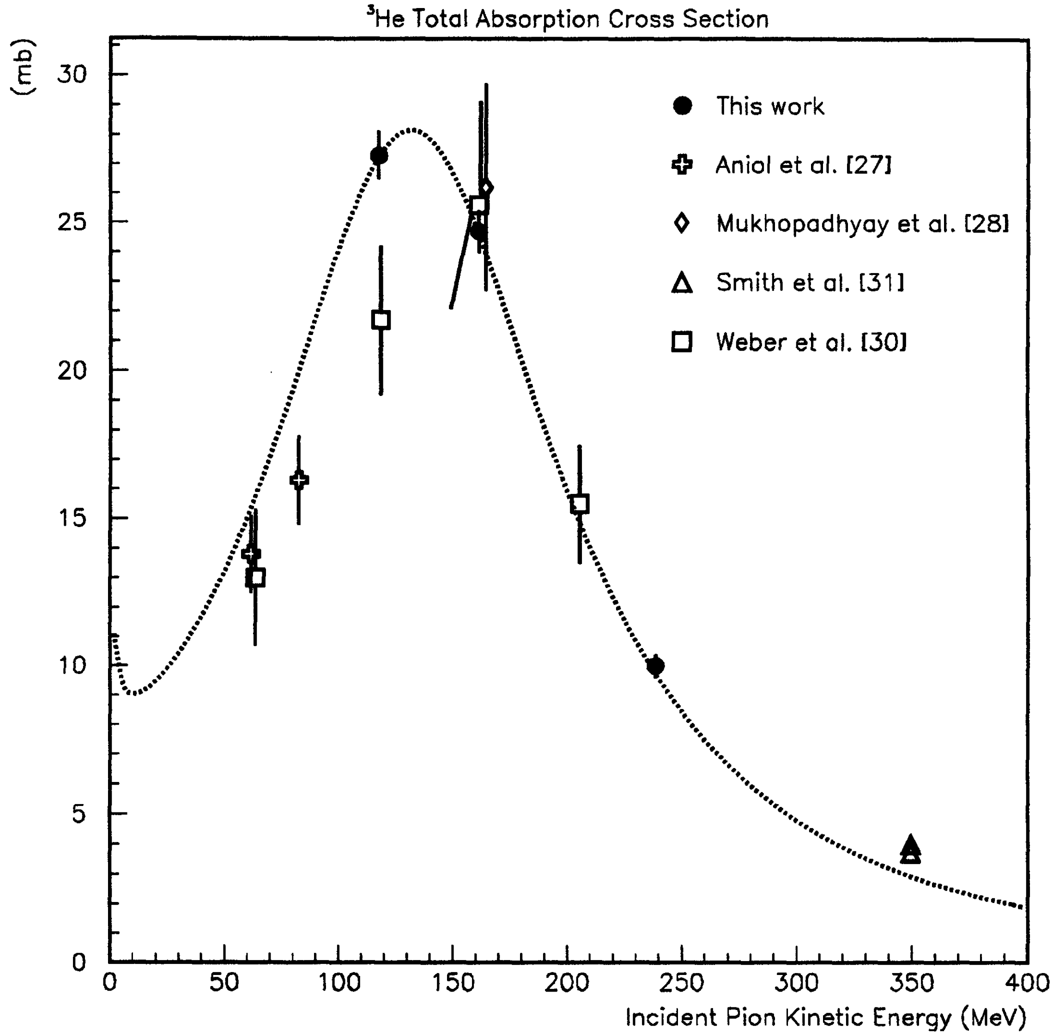

Figure 6-4: The dotted line is the parameterization of the ^{2}H absorption cross section, scaled by a factor of 2.3. None of the measurements include any model-dependent uncertainties, although the two data points by Smith *et al.* [31] represent two different assumptions about the 3NA mechanism.

^{3}He Detector Cross Sections			
T_π (MeV)	$\sigma_{p=2}$ (mb)	$\sigma_{p=3}$ (mb)	Total (mb)
118	18.0	5.8	23.8
162	14.9	7.0	21.9
239	5.7	3.4	9.1

Table 6.2: The table presents raw cross sections, before acceptance corrections. $\sigma_{p=n}$ is the cross section for detecting n protons with LADS for pion absorption on ^{3}He. $\sigma_{p=2}$ and $\sigma_{p=3}$ combined with equations 4.13–4.15 and Table 4.8 are used to calculate the integrated cross sections. The last column is only for comparison purposes and is simply the sum of $\sigma_{p=2}$ and $\sigma_{p=3}$.

space mechanism to extrapolate over the experimentally unmeasured regions. However, the results reported here for the total cross section represent an extrapolation which is less than 15% of the total cross section at all three energies. This fact can be seen in Table 6.2 which reports the cross sections before corrections for acceptance. Essentially, LADS measures the total cross section by simply counting absorption events. The breakup into absorption events in which two or three protons were detected allows a more accurate extrapolation over the unmeasured regions.

In contrast, previous experiments in the Δ resonance region have measured the total by summing the 2NA and 3NA cross sections. The 2NA was extrapolated by fitting the differential cross section to a second order polynomial, though one experiment [28] claimed that a fourth order polynomial was indicated. The other experiment at the same energy (T_π = 165 MeV) [29] had insufficient statistics and angular coverage to determine whether a fourth order polynomial was necessary. If a fourth order polynomial fit was used for the experiment with the larger angular coverage [28], the 2NA and total absorption cross sections were lowered by 14%, and 9%, respectively. Presumably, the experiments with smaller angular coverage would be affected by a larger amount if a fourth order polynomial were necessary. Again because of LADS's large angular coverage, the total cross section was insensitive to changes in the coefficient of the fourth order polynomial in our Monte Carlo; changing this coefficient by a factor of two from what was given by the Ritchie parameterization of ^{2}H changed the total cross section by less than 1%. The 3NA was measured in the previous experiments with an acceptance of typically 0.14% in several different regions for a total solid angle coverage of about 1% [55]. It is difficult, if not impossible, to estimate how a non-isotropic angular distribution of the 3NA mechanism would have affected the previous measurements of the total cross section. However, LADS's acceptance for a 3NA phase space mechanism was ≈ 95%, and therefore it was insensitive to an anisotropic angular distribution of the 3NA mechanism.

The results reported here indicate a peaking of the total absorption cross section at a lower incident pion kinetic energy than previous measurements. This location of the peak is more in agreement with the data on ^{2}H and ^{4}He [8, 70, 71], as can be seen by the dotted line in Figure 6-4. This work's close agreement with the scaled ^{2}H cross section is intriguing. However, other than the obvious fact that absorption is dominated by a Δ intermediate state, little can be concluded about the agreement (or lack of agreement) in the shapes of the ^{2}H and ^{3}He absorption cross sections until there are a few more measurements on ^{3}He, especially at lower energies, that do not have large model-dependent extrapolations.

6.4 ^{3}He Two-Nucleon Absorption Cross Sections

The 2NA cross sections on ^{3}He are reported in Table 6.1 and shown in Figure 6-5. Again, the uncertainty in the LADS measurement is much smaller than in previous experiments. None of the results report an error associated with the model-dependent extrapolation. All of the experiments have in common the assumptions which Section 6.1 attempts to justify, namely that the two-nucleon absorption is dominated by a quasi-deuteron-like absorption mechanism and that the three-nucleon absorption is distributed like three-body phase space. A portion of the 3NA appears as background in the 2NA and must be subtracted out.

The LADS 2NA cross section is measured by using the information about the number of times LADS detects two protons or three protons for an absorption event. For a mathematical description, see Section 4.7.2. Hypothetically, if the spectator particle in 2NA had no Fermi momentum and was thus never detected, and all three protons in 3NA were always detected, the separation would be trivial. As this is not the case, the Monte Carlo provided a way to model the amount of 2NA for which three protons were detected, and the amount of 3NA for which LADS detected only two protons. Because of LADS's almost complete angular coverage, the results are primarily sensitive to the energy distribution of the least energetic proton in the laboratory frame. This dependence seems to be well modeled, as shown in Figure 6-2, and an uncertainty associated with the spectator momentum has been included in the uncertainty of the 2NA and 3NA cross sections measured with LADS.

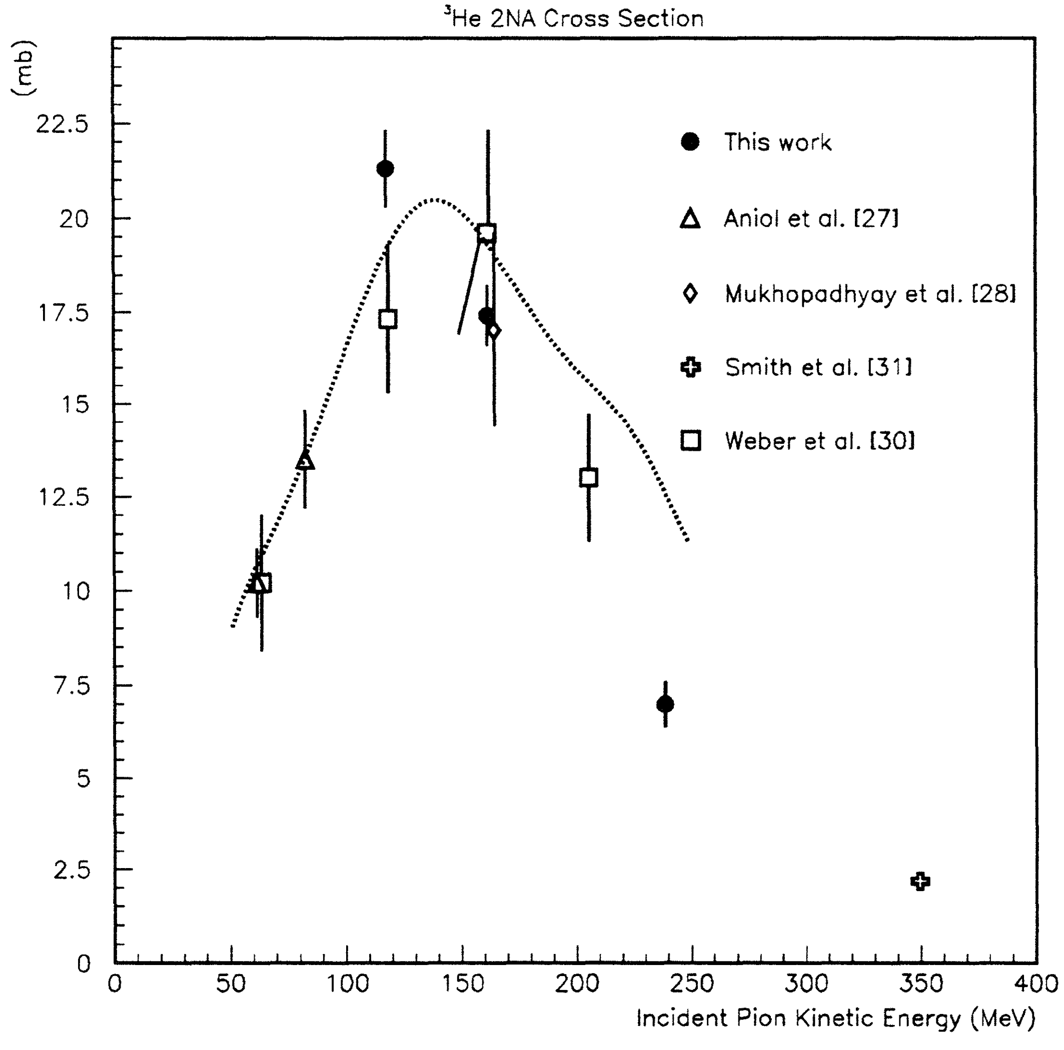

Figure 6-5: Pion absorption on two nucleons in ^{3}He around the Δ-resonance. The dotted line is a calculation by Ohta, Thies, and Lee [17, 72] with modifications described in the text.

As mentioned above, other experiments used the angular information $d\sigma/d\Omega$ to measure the 2NA cross section and were sensitive to assumptions about A_4. In addition, some of them were also sensitive to the momentum of the spectator proton. The experiments of Weber *et al.* [29] had a cut on the momentum of the spectator proton at 150 MeV/c to eliminate 3NA, and extrapolated further using a model of the spectator momentum based on $^3\text{He}(e,e'p)pn$ experiments. The acceptance of their detector system at any particular angle was also dependent on the spectator momentum, and the correction for this dependence was as high as 50%. The acceptance correction of Aniol *et al.* [27] was similarly affected. Mukhopadhyay *et al.* claim that in their experiment the acceptance correction due to the spectator momentum was only 1–2.5%, because one arm was a spectrometer having a very small acceptance and the other arm was a large array of scintillators.

Ohta, Thies, and Lee (OTL) [17] have attempted to model the 2NA mechanism. In their paper, they calculate 2NA using a $\pi NN \leftrightarrow N\Delta \leftrightarrow NN$ transition matrix, a Faddeev wavefunction for ^{3}He and the impulse approximation. The transition matrix is derived from the phenomenological Hamiltonian of Betz and Lee [73], which was constructed to describe NN scattering phase-shifts up to 1 GeV. This model is applied to the $^2\text{H}(\pi^+,pp)$ reaction, and it overestimates the cross section and peaks at too high an incident pion energy. To correct the theory before comparison to differential data on ^{3}He, OTL multiply by R:

$$R = \left[\left(\frac{d\sigma}{d\Omega}\right)_{exp} \Big/ \left(\frac{d\sigma}{d\Omega}\right)_{calc}\right]_{\pi d \to pp} . \tag{6.2}$$

For a comparison to the integrated ^{3}He 2NA cross section, an extension of this method has been used. We have multiplied the OTL calculation by R, where R is now defined as:

$$R = [\sigma_{exp} \;/\; \sigma_{calc}]_{\pi d \to pp} . \tag{6.3}$$

This correction implicitly takes into account some of the π–d distortion and deficiency of the Betz-Lee model. The correction's effect is to move the peaking to lower energies, thus increasing the cross section below 130 MeV, and decreasing the cross section above this energy. A relativistic correction, denoted by C, is also needed since Ohta *et al.* use the nonrelativistic form for the final NN phase space [72]:

$$C = \frac{\rho_{rel}}{\rho_{non-rel}} = \frac{E(q)}{m_p} 4E(q)^2 = (T_\pi + m_\pi + 2m_p)^2 - \left((T_\pi + m_\pi)^2 - m_\pi^2\right) . \tag{6.4}$$

The effect of the relativistic correction is to increase the cross section by 10–20%. The dotted line in Figure 6-5 has both R and C included. This calculation, as in the case of ^{2}H(π^+, pp), overestimates the data for $T_\pi > 150$ MeV, even after being corrected for this effect in ^{2}H.

Since LADS also measured pion absorption on ^{2}H, the ratios of 2NA cross section to the deuterium cross section at each energy are possibly more accurate than the absolute values reported, as some systematic errors could cancel. The ratios that LADS reports are 1.86 ± 0.10, 1.60 ± 0.09, and 1.63 ± 0.15 at 118, 162, and 239 MeV respectively. In calculating these ratios, more significant digits have been kept than is reported in Table 6.1. The uncertainties reported do not assume any cancellation of systematic errors.

There has been some discussion about the ratio of the 2NA cross section to the deuterium cross section, and the fact that it is close to 1.5 has sometimes been interpreted as evidence that the cross section scales simply with the number of $T = 0$ "deuteron-like" pairs in ^{3}He. While it is true that the number of $T = 0$ pairs in ^{3}He is an important effect, expecting the ratio to be exactly 1.5 neglects a number of other effects that are also likely to be important. These other effects that may be important are: the higher density of ^{3}He, the differences in binding energy, absorption on pairs with other quantum numbers, and the existence of competing reaction channels.

The OTL model, which includes the density effect and uses a realistic ^{3}He wavefunction, predicts an enhancement of 15% over this ratio of 1.5 at energies below 150 MeV, but the enhancement of the ratio in the OTL model rises quickly to 100% at $T_\pi = 230$ MeV. This effect is clearly not seen in the LADS data. Instead, the enhancement is found to be smaller at pion kinetic energies of 162 and 239 MeV than at 118 MeV. This fact, along with the increasing importance of the 3NA cross section at higher energies, suggests that competing reaction channels are important and reduce the enhancement seen in the 2NA cross section. Thus the closeness of the 2NA cross section to 1.5 times the ^{2}H cross section is more likely due to the cancellation of competing effects than to the adequacy of the naive model.

6.5 ^{3}He Three-Nucleon Absorption Cross Sections

The 3NA cross section is shown in Figure 6-6 and represents the first measurement of this process that did not involve large extrapolations over unmeasured regions. The 3NA cross section seems to peak at a higher energy than the total and 2NA cross sections. As Figure 6-7 shows, the percentage of 3NA in the cross section increases with increasing incident pion kinetic energy in the region shown.

The peaking of the 3NA cross section near the Δ-resonance region suggests that a Δ is involved in an intermediate state. The fact that the peaking is at a higher T_π than observed in the total and 2NA cross sections may be indicative of a two-step process. Any two-step process in which the first interaction reduces the energy available for the formation of the Δ in the next step would tend to peak at a higher energy than the total cross section. Since pion-nucleus interactions in this energy region are dominated by Δ formation, it is natural to assume that the initial step also involves the formation of a Δ. Thus sequential formation of more than one Δ is a possible explanation of this behavior. An initial state interaction mechanism is one such sequential two-step process that has received much attention [74, 75, 76, 22]. In the classical limit of this process, where an on shell pion is the intermediate particle between the initial scattering and the Δ formed in the second step, a kinematic signature should be detectable in some of the differential measurements. Whether this signature is seen is a subject of Section 6.6.

The peaking of the 3NA at a higher energy than the 2NA does not give support to all two-step processes, but only to processes in which the final step involves the formation of a Δ. For example, one would not tend to expect this behavior from FSI. Since the proton-proton cross sections are decreasing or flat in this energy range, any FSI component in the 3NA would cause it to peak at a lower energy or at the same energy as the 2NA cross section.

The fact that the 3NA cross section is growing in importance with increasing incident pion kinetic energy might be the natural explanation for the decrease of the ratio of the 2NA cross section to ^{2}H absorption cross section. The 3NA cross section could be taking strength from the 2NA cross section through competition with the 2NA channel for the incident pion.

6.6 Differential Measurements of Three-Nucleon Absorption on ^{3}He

In this section we want to gain a qualitative understanding of the 3NA mechanism. To simplify this task, some further restrictions are placed on the absorption data which has been filtered out using the method described in Chapter 4.

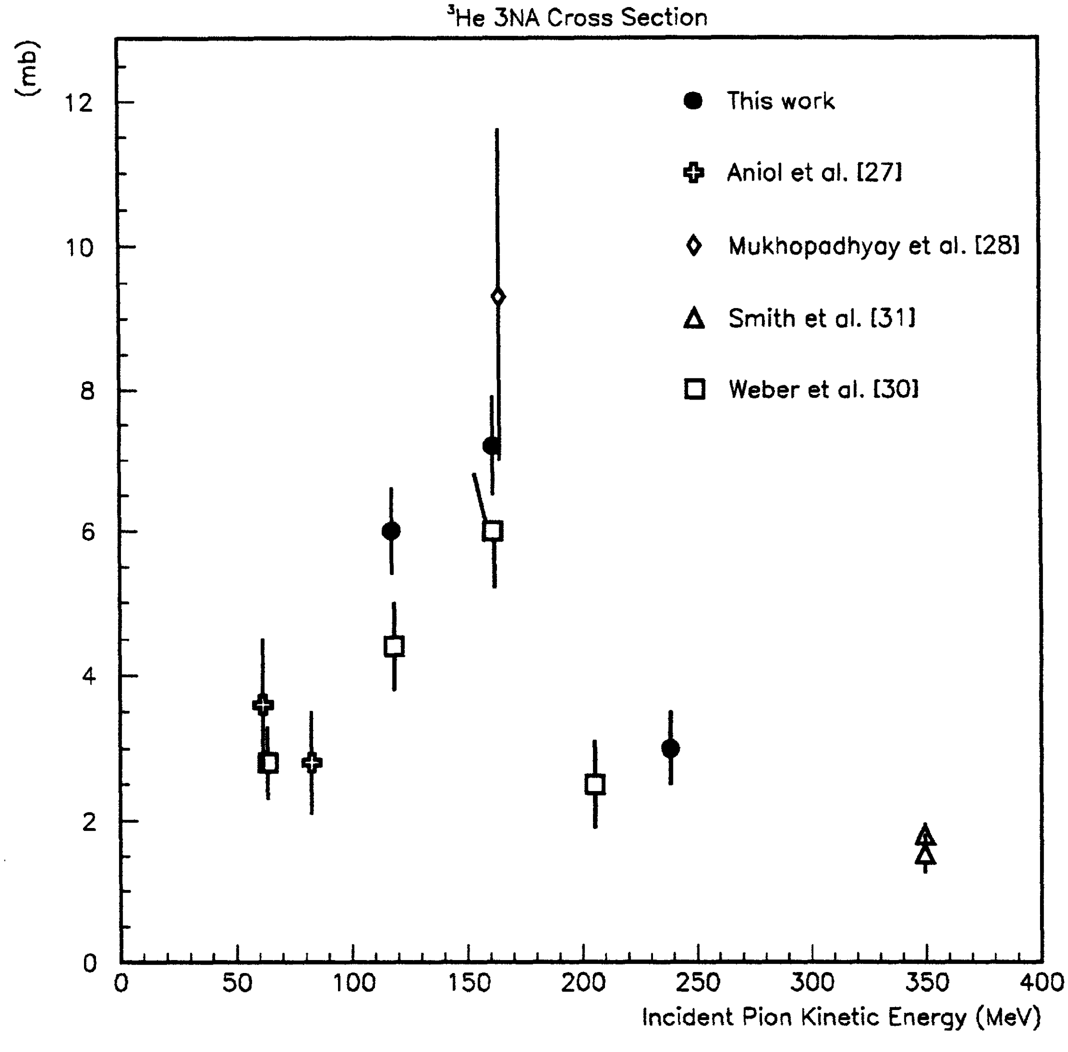

Figure 6-6: Three-nucleon pion absorption on ^{3}He. Two points are reported for Smith *et al.* The lower point assumes isotropic three-body phase space, while the other point comes from a fit of a fifth order Legendre polynomial to θ_{Lab}.

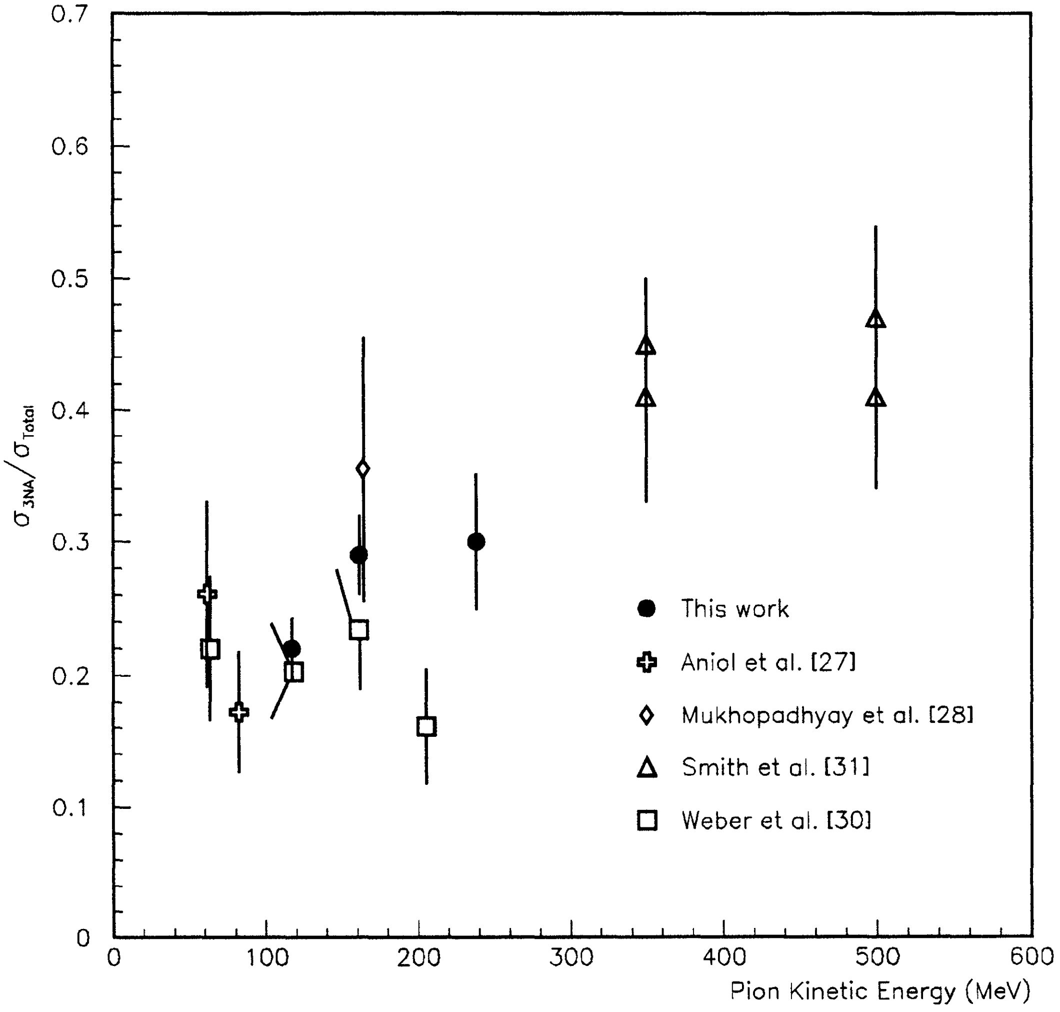

Figure 6-7: The ratio of the 3NA cross section to the total pion absorption cross section on ^{3}He.

To examine the 3NA mechanism, in this section we restrict ourselves to the three charged particle (3C) event types and include the requirement that LADS must have detected three protons, each with an energy above 30 MeV. On one hand, this requirement reduces the acceptance of LADS, for 3NA events distributed like an isotropic three-body phase space, to 58%, 64%, and 72% for T_π = 118, 162, and 239 MeV, respectively; on the other hand, the acceptance for 2NA events is reduced to $1.7 \pm .9\%$, $2.6 \pm .9\%$, and $6.5 \pm 2.7\%$, respectively. The 2NA acceptance has been calculated assuming a momentum distribution of $N_{p,T=0}(p)$ for the spectator; the error bars represent the deviation in the acceptance if a $N_{pd}(p)$ momentum distribution is used. From the acceptance for the two processes and the relative size of the cross sections, the amount of 2NA contamination expected is $9.3 \pm 5.0\%$, $8.9 \pm 3.0\%$, and $17.4 \pm 7.3\%$ at T_π = 118, 162, and 239 MeV, respectively, the error being completely dominated by the uncertainty of the spectator momentum distribution. This amount of contamination and the uncertainty associated with it are large enough that it will need to be kept in mind, but we will see that it is not large enough to prevent qualitative conclusions. To eliminate the need for an empty target subtraction, a radius cut was placed on the vertices of the events, which required the events to be within 1.5 cm of the beam axis. Events in which one or more protons reacted in the scintillator were eliminated from the data with a cut on the summed kinetic energy of the three protons, removing events that were missing more than $\approx$ 20 MeV. The removal of these events prevented the distribution from being distorted by events with reactions appearing in the wrong place; however, it did not remove the distortions which were due to different final state energy distributions with different probabilities of having reactions in the scintillator. This effect on the shape of the distributions is estimated to be about 15% in the absolute worst case[‡]. This amount of distortion is large enough to cause concern, particularly with respect to energy distributions, but if it is kept in mind qualitative conclusions may still be drawn. No attempt was made to correct for those events that were lost due to the target cut or the missing energy cut, as there was no intention of doing an absolute normalization. However, since the MWPC inefficiencies were likely to affect the angular distributions substantially, corrections to the distributions were made for these MWPC inefficiencies using the information about the number of protons in the event which hit the endcap combined with Table 4.5.

[‡] The worst case was calculated for $T_\pi = 239MeV$, a final state with protons with kinetic energies in the laboratory frame of 300, 50, and 30 MeV respectively, compared with a final state with protons each with a kinetic energy 126 MeV. Using the tables in the *TRIUMF Kinematic Handbook*, the probability of a reaction for the former distribution is $(1-.50)(1-.045)(1-.02) = .47$ and for the latter is $(1-.185)^3 = .54$. The relevant quantity is the ratio $.54/.47 = 1.15$. The worst case is somewhat irrelevant due to the very small part of phase space it occupies. A more realistic worst case would consist of a distribution of energies of 250, 100 and 30 MeV for the final state protons; its reaction probability is .49, which gives a ratio of 1.10.

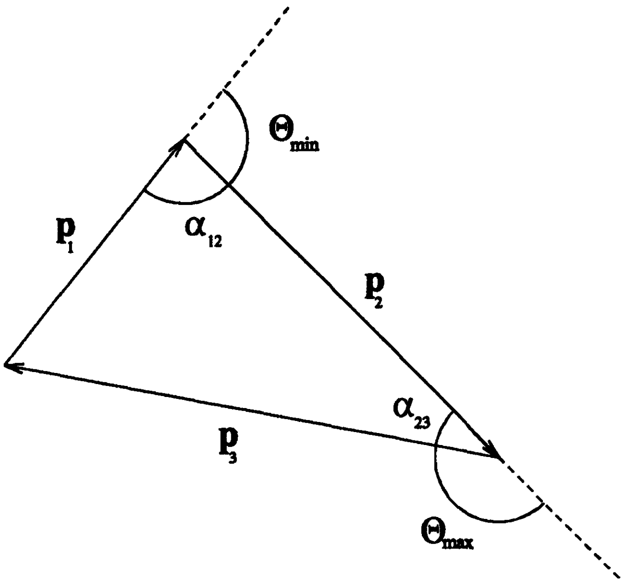

Figure 6-8: In the π–^{3}He center of mass frame, the three outgoing proton momenta form a triangle by momentum conservation, $\vec{p}_1+\vec{p}_2+\vec{p}_3 = 0$. In combination with energy conservation, the shape and size of the triangle is completely fixed if either two sides or two opening angles are specified. Because we have ordered the protons by energy, Θ_{min} and Θ_{max} are the complements of angles α_{12} and α_{23} respectively.

The natural frame in which to study the 3NA process is the π–^{3}He center of mass frame with the incident pion beam defining the z coordinate axis. It is convenient to label the protons in an event as "1," "2," or "3," ordering according to increasing kinetic energy in the center of mass system, with proton "1" being the least energetic proton in the event. The final state is given by the momenta of the three protons, $\vec{p}_i$. The three momenta have nine components, but energy and momentum conservation reduce the number of independent variables to five. The choice of which five variables to use in describing the final state is not unique, though some choices may seem more natural than others.

In the center of mass system, $\vec{p}_1 + \vec{p}_2 + \vec{p}_3 = 0$. Adding the three momentum vectors together forms a triangle, with sides of length $|\vec{p}_i|$. See Figure 6-8. The interior angle between sides 1 and 2, $\alpha_{1,2} = \alpha_{2,1}$, is equal to 180° minus the opening angle, Θ_{min}, between the momentum vectors $\vec{p}_1$ and $\vec{p}_2$, *i.e.* $\alpha_{1,2} = 180° - \Theta_{min}$. The size and shape of the triangle formed by the momentum vectors can be specified with two variables: the triangle's shape can be specified by two angles, the size of the triangle is then given by energy conservation,

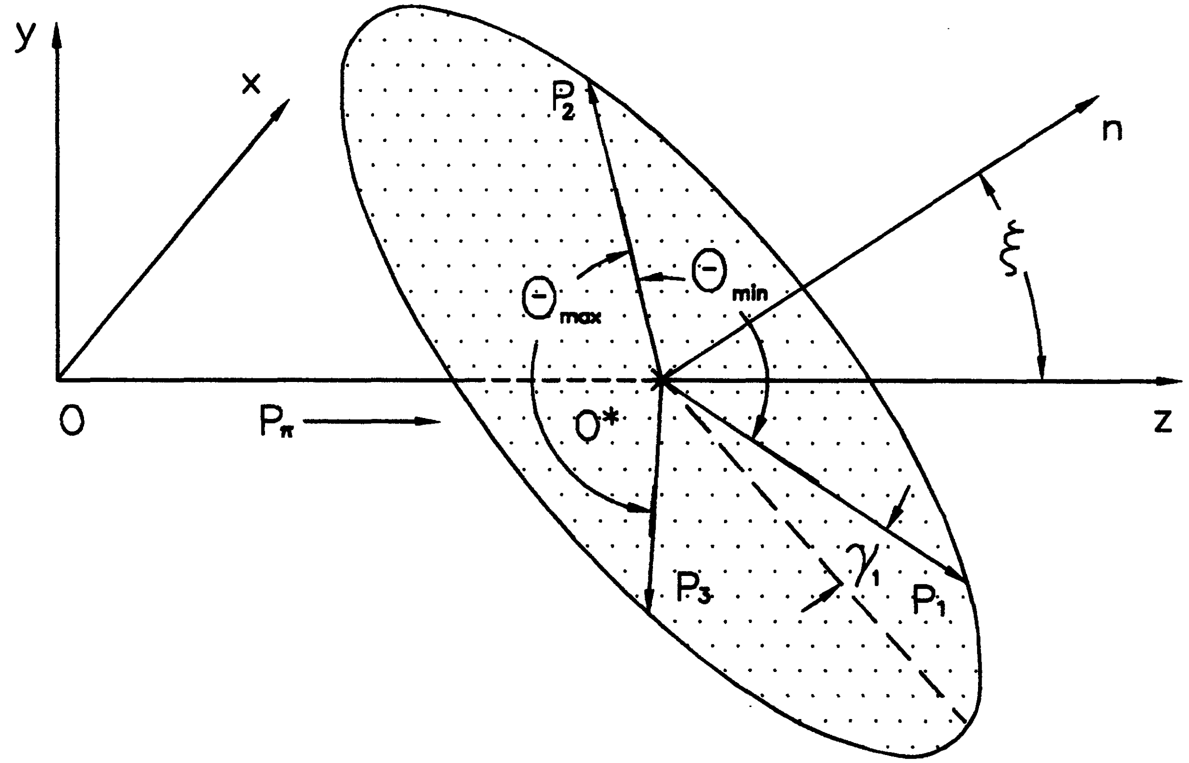

Figure 6-9: Illustration of the definitions of the angles Θ_{min}, Θ_{max}, ξ, and γ_1. The O and O* coordinate systems represent the laboratory and center-of-mass frames, respectively. The vectors P_i represent unit momentum vectors of the final state protons; n is the unit normal to the plane. The dashed line is the projection of the z-axis on the reaction plane.

$\sum_{i=1}^{3} \sqrt{|\vec{p}_i|^2 + m_p^2} = E_{init}^2$. Alternatively, if the lengths of two sides of the triangle are specified (using either $|\vec{p}|$ or T for two of the final state protons), then energy conservation specifies the length of the third side, and again the size and shape of the triangle are uniquely determined. Thus, two of the five independent variables are necessary to specify the momentum vectors of the outgoing protons. Two possible choices for these two variables are $(\Theta_{min}, \Theta_{max})$ or (T_1, T_3).

The remaining three independent variables are used to specify the orientations of the momentum vectors in space with respect to the beam axis. The momentum vectors lie in a plane and the reaction plane's orientation can be described by the normal to the plane, $\hat{n} = (\vec{p}_1 \times \vec{p}_2)/|\vec{p}_1 \times \vec{p}_2|$. The vector $\hat{n}$ in a three-body final state is analogous to the relative momentum in a two-body final state [77, 64]; it contains the information about the total angular momentum of the system. The angles β and ξ are the azimuthal and polar angles respectively, between $\hat{n}$ and the beam axis. Since the target is unpolarized, no reference point from which to measure β can be specified, and thus the experiment integrates over all β's. Therefore all information about β is lost.

Finally, it is necessary to specify the orientation of the three proton momenta within the reaction plane. The angle γ_i is the azimuthal angle of the i^{th} proton with respect to $\hat{n}$. Zero degrees is at the projection of the incident pion beam onto the plane, *i.e.* the right handed coordinate system is defined as $z' = \hat{n}$ and $x' = (\hat{n} \times \vec{p}_\pi) \times \hat{n}$, with γ_i the azimuthal angle of $\vec{p}_i$ measured around z' from x'. The γ_i angles serve to specify the orientation of the final state protons in the plane. Because the relative orientation of the momentum vectors were specified by $(\Theta_{min}, \Theta_{max})$, or equivalently (T_1, T_3), only one γ_i angle is necessary to determine the final state completely. Because the concept of a "spectator" frequently comes up, focusing on γ_1, the angle measured to the least energetic proton, seems most natural.

Thus, two equivalent choices of five independent variables which completely specify the final state are $(T_1, T_3, \beta, \xi, \gamma_1)$ and $(\Theta_{min}, \Theta_{max}, \beta, \xi, \gamma_1)$. Since the experiment contains no information about β, we will ignore it in the rest of the discussion.

We have already looked at the energy of the least energetic proton in the laboratory frame in Section 6.1, and it was found to be well described if we assume that the 3NA process has an energy distribution consistent with three body phase space. This result is in agreement with previous experiments [27, 29, 28, 31]. In Figure 6-10 we see the kinetic energy distributions in the center of mass frame for the least and most energetic protons in this frame. In general, these distributions follow three body phase space fairly closely. At T_π = 118 and 162 MeV, there are some small features, and there is perhaps a bump in T_3 at the higher energies, but

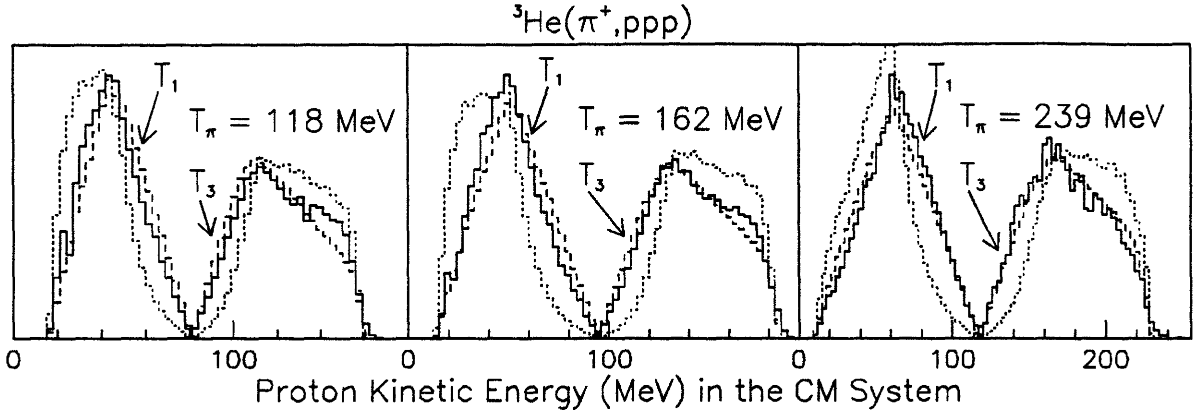

Figure 6-10: Pion absorption on ^{3}He with all three protons above 30 MeV in the lab frame. Shown are $T_1 = T_{min}$ and $T_3 = T_{max}$ in the π–^{3}He center of mass frame. The data is the solid line; isotropic 3-body phase space is the dashed line, and quasi-deuteron model with a spectator proton is the dotted line. The y-axis is counts in arbitrary units and the spectra are normalized to equal area. The expected contamination of 2NA in the data is $9.3 \pm 5.0\%$, $8.9 \pm 3.0\%$, and $17.4 \pm 7.3\%$ at $T_\pi = 118$, 162, and 239 MeV, respectively.

by themselves these features are not large enough to be able to attribute them confidently to something other than experimental uncertainty. At $T_\pi = 239$, the expected 2NA contamination would make the phase space fit visibly worse, and there are places where there appears to be excess strength – but these graphs are particularly vulnerable to the distortions from reactions that were discussed above, and the expected effect of these reactions would be to produce excess strength at low T_3 and high T_1. Since the opening angles (Figure 6-11 are equivalent to T_1 and T_3, it is not surprising that these angles show the same general features.

LADS is the first pion absorption experiment on ^{3}He which has the ability to look at the plane angle ξ. The plane angle does not look like isotropic three-body phase space, but instead is well fit by the QDM Monte Carlo. That the shape of the QDM agrees so well with the data for ξ at all three energies seems to be indicating a similarity between the QDM mechanism and the 3NA mechanism. As has been stated before, the plane angle contains information about the angular momentum of the system. It has been shown that for a "one-step" process, the relative angular momentum between the incident pion and the ^{3}He nucleus determines the distribution

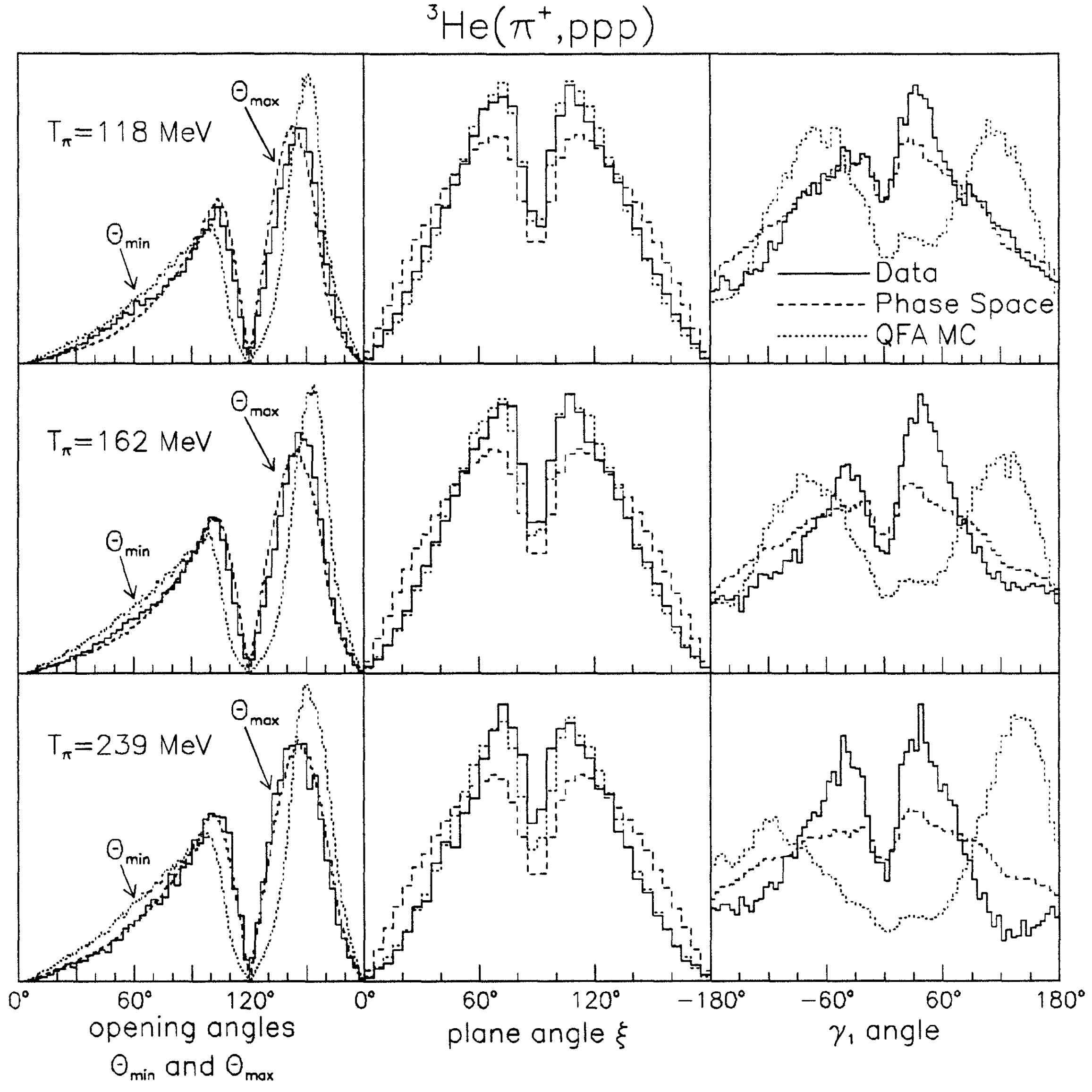

Figure 6-11: Center of mass angles for pion absorption on ^{3}He with all three protons above 30 MeV in the lab. Each row is for a different incident pion energy and each column is for a different independent kinematic variable. The data is the solid line; isotropic 3-body phase space is the dashed line; and the quasi-deuteron model with a spectator proton above threshold is the dotted line. The y-axis is in arbitrary units and the spectra are normalized to equal area. The expected contamination of 2NA in the data is $9.3 \pm 5.0\%$, $8.9 \pm 3.0\%$, and $17.4 \pm 7.3\%$ at T_π = 118, 162, and 239 MeV, respectively.

of the plane angle [66, 64]. In particular,

$$\frac{d\sigma}{d\beta d\cos\xi} = \sum_{n=0}^{l_\pi} A_{2n} P_{2n}(\cos\xi) \ , \tag{6.5}$$

where l_π is the relative angular momentum between the pion and the ^{3}He nucleus. We can thus determine that a minimum l_π is required to contribute to the reaction by noting how many Legendre polynomial terms are necessary to describe the distribution. In Figure 6-12 the $d\sigma/d\xi$ for $^3\mathrm{He}(\pi^+, ppp)$ is divided by isotropic three-body phase space to remove the acceptance effects of the detector and the $\sin\xi$ phase space dependence. The remainder can then be fit with a Legendre polynomial. Only the zeroth and second order Legendre terms were needed. If a fourth order term is necessary, it is limited to being relatively unimportant. Therefore, 3NA cannot be described by the absorption of only $l_\pi = 0$ pions. Classical arguments suggest that the reaction will be dominated by low l_π. Along with the lack of a large fourth order term, this suggests that $l_\pi = 0$ and $l_\pi = 1$ are the dominant contributions to the reaction. The relative importance of $l_\pi = 0$ and $l_\pi = 1$ unfortunately cannot be determined from the plane angle, since absorption from an $l_\pi = 1$ state has both A_0 and A_2 terms depending on whether the coupling to the spin of the ^{3}He nucleus is $J = 1/2$ or $J = 3/2$. Nevertheless, the fact that the distribution is well fit by the QDM Monte Carlo strongly suggests that the initial coupling of the pion to the nucleus is the same in 2NA and 3NA. When combined with the energy dependence of the cross section, the experimental evidence indicates that the 3NA mechanism has a $\pi N \to \Delta$ as the initial coupling of the pion to the ^{3}He nucleus.

The orientation of proton 1 in the reaction plane, γ_1, is also shown in Figure 6-11 for all three energies. Without allowing for the detector's acceptance, three-body phase space predicts a flat distribution for γ_1; thus the dip in the phase space Monte Carlo at 0° and the decreased strength near ±180° are related to the acceptance of the detector. It is important to note that γ_1 is independent of ξ. Therefore if ξ, in a modification to a three-body phase space Monte Carlo, were weighted by the observed A_2/A_0 ratio, γ_1 would still be flat if there were no acceptance corrections. To check that the detected γ_1 was not coupled to ξ in combination with the detector's acceptance, a three-body phase space Monte Carlo weighted with the observed A_2/A_0 ratio at $T_\pi = 239$ MeV was made. The calculation reproduced within statistical variation the distribution in γ_1 shown in Figure 6-11 for an unmodified phase space Monte Carlo.

Clear deviations in γ_1 from three-body phase space are apparent at all three incident pion energies. While it is not clear how reactions occurring preferentially in certain final state energy distributions could effect γ_1, it is clear that they are much too small to explain these deviations

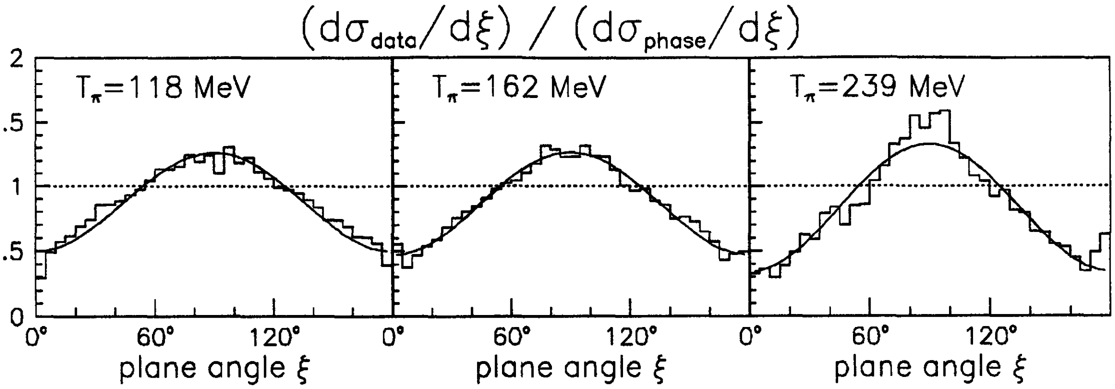

Figure 6-12: After subtraction of the expected 2NA contamination, the distribution in ξ in Figure 6-11 has been divided by the three–body phase space Monte Carlo shown in the same figure and renormalized so that $A_0 = 1$. The fit is with zeroth and second order Legendre polynomials and produces an A_2/A_0 of -0.5, -0.5, and -0.7 at $T_\pi = 118$, 162, and 239 MeV, respectively. The dotted line is an isotropic three-body phase space distribution.

from three-body phase space. Subtracting the expected 2NA contamination from the data would make the deviations from three-body phase space even more pronounced. The observed asymmetry in the 2NA model is a consequence of the most energetic proton usually going forward in the π–^{3}He center of mass frame[§] and the least energetic proton having an isotropic distribution in the laboratory frame.

In the data there is a peaking of γ_1 near 50° and a corresponding lack of strength at $-140°$ at all three incident pion energies, and at the two higher energies a somewhat smaller peak at $-50°$ becomes apparent along with a dip at 120°. These features indicate that the least energetic proton tends to be forward peaked in the π–^{3}He center of mass frame, which is different from both phase space and the QDM. This kinematic variable, γ_1, shows the largest and most striking variations from three-body phase space of any of the five independent kinematic variables we have used to describe the final state. These variations clearly demonstrates that the matrix element describing the 3NA process cannot be just a constant. Presumably, these variations can discriminate between the different possible 3NA mechanisms.

It is possible to reexamine this and previous integrated cross sections for 3NA in light of this new information about the angular variation from an isotropic three-body phase space

---

[§] In the QDM, the two protons have equal energy in the π–d CM system, therefore in the π–^{3}He CM system, the most energetic proton is in the direction of the incident pion.

distribution, and consider how the angular variations would modify the results. For the LADS results, it is unlikely to have much of an effect since most of the angular range is covered. The extrapolation over unmeasured angles is only a few percent and the break-up of the total into 2NA and 3NA is dominated by the energy sharing between the protons, which does not show convincing deviations from isotropic three-body phase space. To check this, a Monte Carlo was made that weighted events with a modified phase space that correctly reproduced the measured ξ. If this Monte Carlo was used for the acceptance, the 3NA cross section would be 5.5% larger at the highest energy, with smaller changes at the lower two energies and insignificant changes to the 2NA and total cross sections. It is difficult to properly model γ_1, but by examining the effect that the LADS acceptance has on the γ_1 distribution of the phase space Monte Carlo, it appears not unreasonable to expect an uncertainty of approximately 5% in the integrated 3NA cross section at the highest T_π.

The prior experiments were primarily in-plane ($\xi \approx 90°$), and from Figure 6-12 it can be immediately seen that in-plane experiments should have a tendency to overestimate the amount of 3NA by about 25% at T_π = 118 and 162 MeV, and by about 35% at T_π = 239 MeV. This is due to the contribution of $l_\pi = 1$ to the absorption reaction which causes ξ to peak at 90°. The effect of the total angular momentum of the system is ignored when the 3NA cross section is assumed to be distributed like an isotropic three-body phase space. While this amount of overestimation of the 3NA cross section is roughly consistent with the result of Mukhopadhyay *et al.*, it is inconsistent with the results of Weber *et al.* whose 3NA measurement are low with respect to the LADS measurements. Of course, the deviations in the orientation within the reaction plane, γ_1, would also effect all previous measurements, since these experiments covered only selected angles in the plane. However, at T_π = 119 MeV the deviations in γ_1 are small and Weber *et al.* measured the 3NA cross section at seven different points which would have further minimized deviations due to γ_1, so the lower value of 3NA they report is puzzling. But the 2NA measurements reported here at T_π = 118 MeV are also higher than the measurement of Weber *et al.* at this energy, which indicates that the disagreement is not only because LADS measured the 3NA over the entire range of ξ.

At incident pion energies above T_π = 239 MeV, such as those used by Smith *et al.*, it appears that large systematic errors of the order of $\geq$ 35% can be introduced by the measurements being in the plane of the pion beam, if the experimenter assumes an isotropic phase space distribution. Smith *et al.* saw from their measurements that three-body phase space was a poor assumption for the angular distribution, but their experiment was primarily in the reaction plane and thus only sensitive to variations in γ_1. Thus their fit of θ_{lab} to a fifth order Legendre polynomial is equivalent to attempting to correct for the variations in γ_1 from phase space. This Legendre polynomial fit would not be able to correct their cross sections for the variations we report in ξ.

No in-plane experiment at energies $T_\pi \geq 118$ MeV can measure the 3NA cross section without a systematic error of $\geq 25\%$ if it uses an assumption that 3NA follows an isotropic three-body phase space distribution, or some other assumption that neglects out-of-plane variation. All previous experiments on ^{3}He have made this assumption to extract a 3NA cross section. The error from this assumption tends to increase as T_π increases, consistent with the greater probability of the pion having an orbital angular momentum greater than zero.

No qualitative look at 3NA would be complete without some discussion of two semi-classical models of 3NA that have received much attention – Initial and Final State Interactions (ISI and FSI). In an ISI model the incident pion scatters off of one proton and then absorbs on the other two nucleons. In the classical picture, the initial scattering and subsequent absorption is sequential and incoherent, with the pion on its mass shell in the intermediate state. Appendix A describes a event generators for this process, which included the Fermi momentum of the nucleons and was based on the differential π–p elastic cross section and the ^{2}H(π^+, pp) differential cross section. In a FSI model the pion absorbs on a pn pair and then one of the outgoing protons has a "hard" scattering with a spectator proton, giving the spectator proton a substantial amount of energy. A FSI model was made which included the Fermi momentum of the initial nucleons and uses the ^{2}H(π^+, pp) and the free p–p differential cross section; it is also described in Appendix A.

The results of these two Monte Carlo calculations with respect to a set of four independent variables are informative. There is no evidence for any FSI, but the ISI model can explain the general features that are evident in γ_1. A combination of three-body phase space and ISI would not perfectly match the distribution in γ_1, but it would show the correct features and be a much better fit to γ_1 than phase space alone. However, the amount of ISI added to phase space to fit γ_1 would make the fits to Θ_{max} and Θ_{min} visibly worse: the data do not show enough strength, compared to phase space, at high Θ_{max} or low Θ_{min}. Because (Θ_{min},Θ_{max}) is equivalent to (T_{min}, T_{max}), we must remember that these graphs are most sensitive to distortions due to reactions. Nevertheless, that effect is probably not large enough to allow for all of the distortion to (T_{min}, T_{max}) that our classical ISI model predicts. This failure could be due to the classical nature of the ISI model and a quantum mechanical calculation might lack these sharp features in energy.

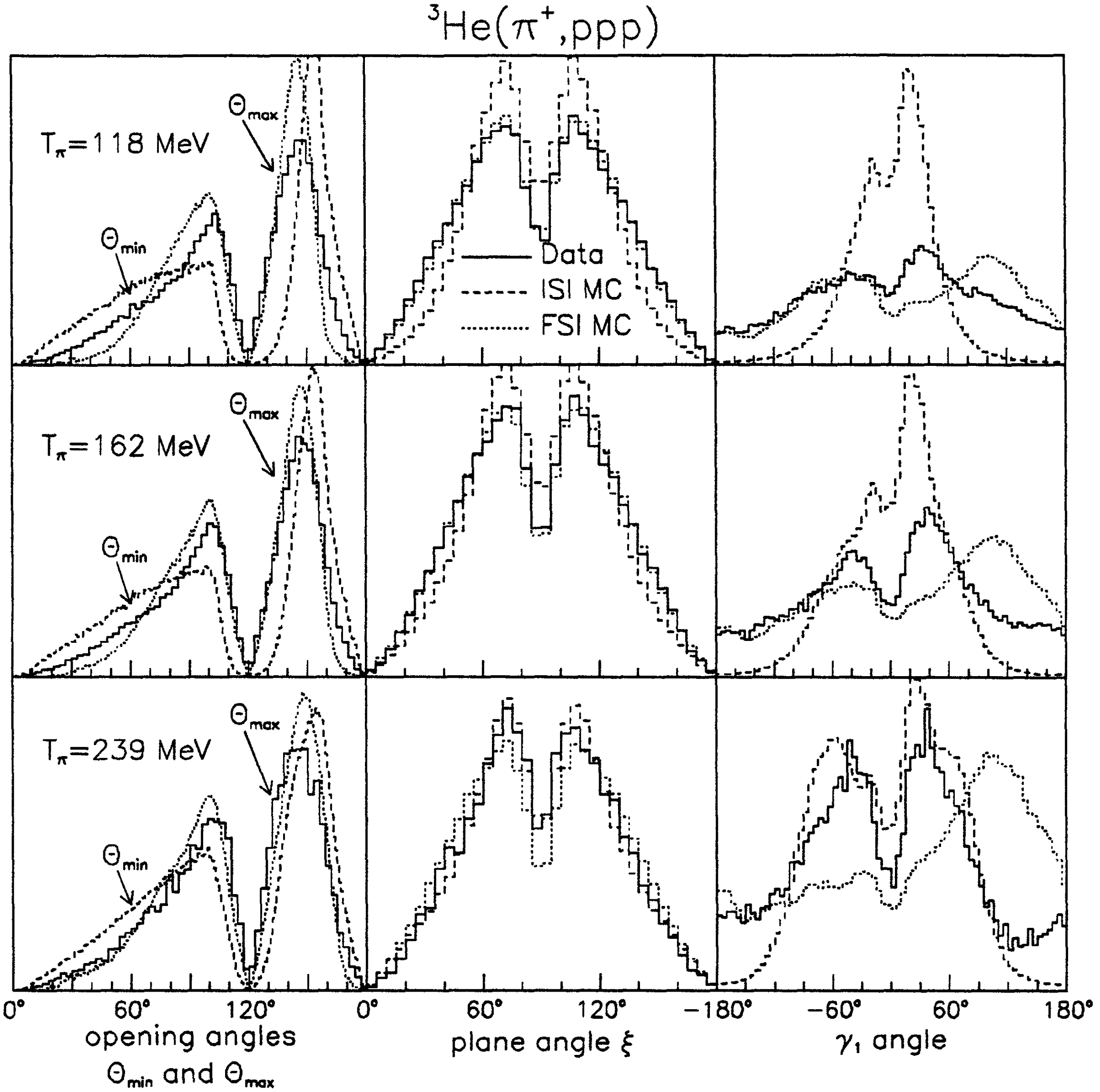

Figure 6-13: Pion absorption on ^{3}He with all three protons above 30 MeV in the lab. Each row is for a different incident pion energy and each column is for a different independent kinematic variable. The data is the solid line; the ISI Monte Carlo is the dashed line; and the FSI Monte Carlo is the dotted line. The y-axis is counts in arbitrary units and the spectra are normalized to equal area. See Figure 6-11 for a comparison to three–body phase space.

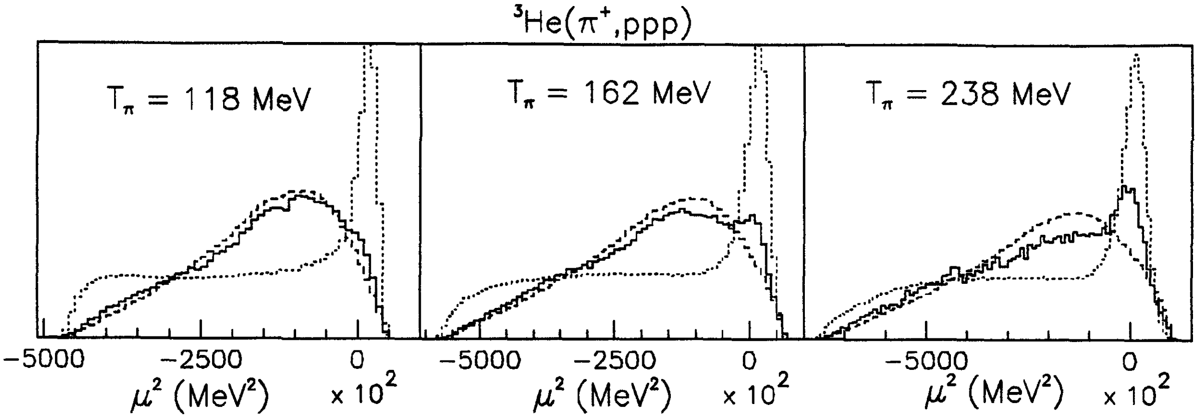

Figure 6-14: The "pseudo-invariant mass squared" at three different incident pion energies. The solid line is the data; the dashed line is three-body phase space; and the dotted line is the ISI Monte Carlo. The y-axis is counts in arbitrary units.

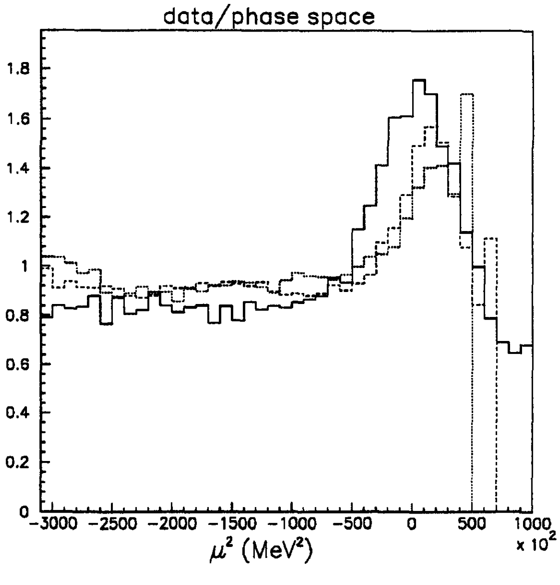

Figure 6-15: The "pseudo-invariant mass squared" with the ^{3}He(π^+, ppp) data divided by phase space. The solid line is T_π = 239 MeV; the dashed line is T_π = 162 MeV; and the dotted line is T_π = 118 MeV. The spikes in the last channel of the distribution for each energy are due to the Monte Carlo's perfect energy resolution in comparison to the detector's energy resolution and are inconsequential as can be seen from Figure 6-14.

Another test for ISI has been suggested by Salcedo *et al.*: signatures may appear in the distribution of a kinematic quantity termed the "pseudo-invariant mass squared" [76], μ_{ij}^2. This quantity is defined in the laboratory frame as;

$$\mu_{ij}^2 = (T_i + T_j)^2 - (\vec{p}_i + \vec{p}_j)^2 \,. \tag{6.6}$$

Thus for each event there are three μ_{ij}^2's. Hypothetically, if there were no Fermi momentum and the pion was on shell after the initial scattering, one of the three μ_{ij}^2s would be equal to the pion's rest mass squared since for the absorbing pair

$$T_i + T_j = T_\pi + m_\pi = E_\pi \tag{6.7}$$

$$\vec{p}_i + \vec{p}_j = \vec{p}_\pi \tag{6.8}$$

$$E_\pi^2 - \vec{p}_\pi^2 = m_\pi^2 \,. \tag{6.9}$$

The Fermi momentum of the nucleons is expected to smear out this peak, but as the Monte Carlo of ISI shows in Figure 6-14, the peak is not completely washed out. The data also shows a peak in μ_{ij}^2 over three-body phase space at the energy predicted by the ISI Monte Carlo which can be most clearly seen in Figure 6-15. The peak increases in size with increasing pion kinetic energy, but is present even at the lowest incident pion energy. Neither the QDM nor FSI Monte Carlo can reproduce the peak in the pseudo-invariant mass.

6.7 Summary of Results

Results have been reported from the first measurement of the total absorption cross section on ^{3}He that do not depend on large extrapolations over unmeasured regions (see Table 6.1). These measurements at T_π = 118, 162, and 239 MeV, while roughly consistent with previous measurements, are considerably more accurate and indicate that the peaking of the total cross section occurs at a lower incident pion energy than previously reported. This is more in agreement with the total cross sections observed in ^{2}H and ^{4}He.

The absorption cross section has also been divided into its 2NA and 3NA components. The 2NA cross section reported is more accurate than previous measurements and less sensitive than the previous smaller acceptance experiments to the magnitude of the A_4 term in the Legendre polynomial fit of $d\sigma_{2NA}/d\Omega$. The A_4 term contributes to $d\sigma_{2NA}/d\Omega$ in ^{2}H and Mukhopadhyay *et al.* [28] found evidence that suggested that the fourth order term may also contribute to the 2NA cross section in ^{3}He. The 2NA cross section reported by LADS peaks at a lower T_π than the results reported by previous experiments.

The ratio of ^{3}He 2NA to the ^{2}H cross section is 1.86±0.10, 1.60±0.09, and 1.63±0.15 at T_π = 118, 162, and 239 MeV, respectively. These ratios differ in magnitude and energy dependence from both the naive isospin scaling model and the more sophisticated 2NA calculation of Ohta, Thies and Lee [17, 72].

The 3NA cross section was measured more accurately than before and for the first time without large extrapolations over unmeasured regions of phase space – particularly important since all previous experiments were primarily in-plane measurements. The 3NA cross section seems to peak at a slightly higher T_π than the total or the 2NA cross section. The 3NA contribution to the total cross section was measured to be 22%, 29% and 30% at T_π = 118, 162, and 239 MeV, respectively. While the size of the 3NA cross section is roughly consistent with the in-plane measurements, particularly those of Mukhopadhyay *et al.* [28], they tend to be slightly higher than those reported by Weber *et al.* [30].

In the center of mass frame, the three final state protons can be labeled by increasing kinetic energy and completely described by five independent variables, $(\Theta_{min}, \Theta_{max}, \beta, \xi, \gamma_1)$ (or alternatively $(T_{min}, T_{max}, \beta, \xi, \gamma_1)$). β and ξ are the azimuthal and polar angles with respect to the pion beam of the vector $\hat{n} = \vec{p}_1 \times \vec{p}_2 / |\vec{p}_1 \times \vec{p}_2|$ and γ_1 is the azimuthal angle with respect to $\hat{n}$ of $\vec{p}_1$. Distributions of these variables can then be used to examine the characteristics of the 3NA mechanism. It is shown in Figure 6-11 that the ^{3}He(π^+, ppp) results show substantial deviations from isotropic three-body phase space, unobserved by earlier experiments [30]. There are clear deviations from isotropic three-body phase space evident in ξ and γ_1 at all three energies that LADS measured.

The peaking of ξ at 90° observed by LADS means that in-plane experiments have systematic inaccuracies of 25-35% in their measured 3NA cross sections, at least for those experiments with $T_\pi \geq 118$ MeV. In general, the systematic error introduced from an experiment measuring the cross section only in-plane was shown to increase with increasing T_π.

The angle ξ was well fit by the zeroth and second order terms of a Legendre polynomial, with a ratio of the coefficients $A_2/A_0 = -0.5$, -0.5 and -0.7 for T_π = 118, 162, and 239 MeV, respectively. The fact that the second order term is necessary to fit ξ shows that the there is contribution from $l_\pi = 1$ coupling of the pion to the nucleus in the 3NA process.

The γ_1 deviations from phase space show features indicative of an ISI-type of process; this conclusion is strengthened by the peak in the pseudo-invariant mass squared. (Shown in Figure 6-15). The contribution of a classical ISI-like process seems to increase with T_π, but at its largest it can only account for perhaps 30% of the 3NA cross section. However, the strictly classical model of ISI that we have employed here is not the solution; while it is the only model that has the right features in several of the distributions, it does not seem to reproduce the correct energy sharing between the final state protons. While an ISI-like mechanism seems to be an important component of the 3NA mechanism in ^{3}He, the lack of evidence for a "hard" FSI mechanism in the many kinematic variables examined indicates that FSI does not contribute significantly to the 3NA mechanism at these energies.

Quantum mechanical calculations of possible 3NA mechanisms are clearly necessary, and there is now a much more complete set of experimental distributions to compare to such calculations.

Appendix A

The ISI and FSI Event Generators

The ^{3}He ISI and FSI event generators perform relativistic, classical calculations. They model the 3NA mechanism as an incoherent two-step process and use parameterizations of cross sections measured outside of the nuclear medium. The Fermi momenta of the initial nucleons are included. The *pn* pair that absorbs the pion is considered to be off-shell, with the remaining nucleon treated as being on-shell. The absorption process is characterized by the Ritchie parameterization [8] of ^{2}H(π^+,*pp*) ; the off-shell nature of the absorbing pair affects the cross section via the E term in that parameterization which is the invariant mass of the π-d system. The CERN library routines LOREN4 [78] and RAN3D [79] were used extensively. LOREN4 transforms the pion and proton four-vectors into the proper frames needed for the parameterization of the various reactions and RAN3D is used to choose random directions for the particles in momentum space.

The ISI event generator assumes that the pion initially scatters off the proton which is not involved in the two-nucleon absorption, the pion is on-shell after the initial scattering and absorbs on the *pn* pair. The steps performed in the ISI event generator are as follows:

1) The Fermi momentum of one of the protons is generated by assigning it a random direction with a momentum between 0 and 400 MeV/c. The event is then assigned a weight of $p^2 N_{p,T=0}(p)$ [26, 60] (see Section 5.6.4.2), which represents the probability of the proton having this Fermi momentum. The proton is assumed to be on-shell and the four vector of the *pn* pair is calculated using energy and momentum conservation of the initial state.

2) The incident pion is transformed to the rest frame of the proton which has the Fermi momentum above to determine the kinetic energy of the pion in that frame, which is needed for the calculation of π-p scattering cross section. A scattering angle in the π-p center of mass frame for the outgoing proton is randomly assigned to be between 5° and 180°. The angle and energy are then used by SCATPI [61] to calculate $d\sigma/d\Omega$. The weight of the event is multiplied by this $d\sigma/d\Omega$.

3) The scattered pion is transformed to the rest frame of the *pn* to determine the T_π at which the absorption takes place. An outgoing proton direction is randomly chosen in the π-pn center of mass frame. The weight of the event is then multiplied by $d\sigma/d\Omega$ calculated from the Ritchie parameterization using the the kinetic energy of the pion, the angle of the outgoing proton, and the total energy of the π-pn system.

4) The three protons' outgoing momenta are transformed into the laboratory frame and also into the π-^{3}He center of mass frame so that various kinematical quantities can be calculated.

The FSI event generator assumes that the pion absorbs on a *pn* pair and then that one of the outgoing protons has a "hard" scattering with the proton that was not involved in the absorption process. A "hard" scattering was defined as a momentum transfer between these two protons of at least 150 MeV/c in their center of mass. This was desirable because it prevented problems in the model which arose from the very large coulomb cross sections for protons that have small momentum transfers. The steps performed in the event generator are as follows:

1) The Fermi momentum of the spectator proton is generated in the same manner as in the ISI event generator.

2) The incident pion is transformed to the frame where the *pn* pair is at rest to find the appropriate kinetic energy for the absorption parameterization. An outgoing proton direction is randomly chosen in the π-pn center of mass. The weight of the event is then multiplied by $d\sigma/d\Omega$ calculated from the Ritchie parameterization using the kinetic energy of the pion, the angle of the outgoing proton, and the total energy of the system.

3) One of the outgoing protons from the absorption event is randomly chosen to undergo a p-p scattering with the spectator proton. It is transformed into the frame where the spectator proton is at rest to find the appropriate T_p energy for the scattering. The scattering angle for the protons is then randomly chosen in the p-p center of mass frame. The momentum transfer between the two protons is then checked to make sure that it is

greater than 150 MeV/c. If the momentum transfer is too small another scattering angle is chosen and if after five choices of scattering angles the momentum transfer is still not large enough, the event is aborted (this happened much less than 1% of the time). If the momentum transfer is large enough, then the weight of the event is multiplied by $d\sigma/d\Omega$ as calculated by SAID [80] using T_p and the scattering angle.

4) The three protons' outgoing momenta are transformed into the laboratory frame and also into the π-^{3}He center of mass frame so that various kinematical quantities can be calculated.

Bibliography

[1] G. Backenstoss et al. "Proposal to Study Multi-Particle Final States in Pion-Nuclear Reactions with a Large Acceptance Detector (LADS)," *SIN proposal R 87-13.1* (1987).

[2] H. Yukawa. "On the Interaction of Elementary Particles," *Proc. Phys. Math. Soc. Japan*, **17**, 48 (1946).

[3] C. M. G. Lattes et al. "Processes Involving Charged Mesons," *Nature*, **159**, 694 (1947).

[4] Particle Properties Data Group. *Particle Properties Data Booklet*, pages 114–115. North Holland, Amsterdam, 1992. Produced by American Institute of Physics, available from Berkeley and CERN.

[5] K. H. R. Machleidt and C. Elster. "The Bonn Meson-Exchange Model for Nucleon-Nucleon Interaction," *Physics Reports*, **149, No. 1**, 1–89 (1987).

[6] M. Rho and D. H. Wilkinson, editors. *Mesons in Nuclei*, chapter 4. North-Holland Publishing Company, 1979.

[7] M. Rho, A. Goldhaber, and G. Brown. "Topological Soliton Bag Model for Baryons," *Physical Review Letters*, **51**, 747 (1983).

[8] B. Ritchie. "Parameterization of the total and differential cross sections for $\pi d \rightarrow pp$ below 1 GeV," *Physical Review*, **C49**, 533–536 (1991).

[9] D. Ashery et al. "True Absorption and scattering of pions on nuclei," *Physical Review*, **C23**, 2173–2185 (1981).

[10] F. Binon et al. "Scattering of Negative Pions on Helium," *Nuclear Physics*, **A298**, 499–529 (1978).

[11] M. Y. D. Wang. *Inclusive Pion Single Charge Exchange ^4He in the Δ-Resonance Region.* PhD thesis, Massachusetts Institute of Technology, September 1994.

[12] M. Steinacher et al. "Pion absorption in flight on ^{4}He," *Nuclear Physics*, **A517**, 413 (1990). This paper has similiar experimental setup, target and beam normalization as the work done by the same group on ^{3}He, reported in Nucl. Phys. **A501**(1989)765.

[13] M. E. Yuly. *Inclusive Measurements of Pion Double Charge Exchange and Inelastic Scattering on ^{3}He.* PhD thesis, Massachusetts Institute of Technology, June 1993.

[14] E. Pedroni et al. "A Study of Charge Independence and Symmetry from $^+\pi$ and $^-\pi$ Total Cross Sections on Hydrogen and Deuterium Near the 3, 3 Resonance.," *Nuclear Physics*, **A300**, 321–347 (1978).

[15] D. Ashery et al. "Isospin Dependence of Pion Absorption on a Pair of Nucleons," *Physical Review Letters*, **47**, 895–898 (1981).

[16] G. Backenstoss et al. "Isospin Dependence of Pion Absorption on Nucleon Pairs in ^{3}He," *Physics Letters*, **137B**, 329–333 (1984).

[17] K. Ohta, M. Thies, and T.-S. Lee. "Study of the Two–Nucleon Mechanism of Pion Absorption in Nuclei," *Annals of Physics*, **163**, 420–472 (1985).

[18] R. McKeown et al. "How Many Nucleons are Involved are Involved in Pion Absorption in Nuclei?," *Physical Review Letters*, **44**, 1033–1036 (1980).

[19] W. J. Burger et al. "Reaction ^{58}Ni$(\pi^+, 2p)$ at 160 MeV," *Physical Review Letters*, **57**, 58–61 (1986).

[20] W. J. Burger et al. "Reaction ^{58}Ni(π^+, pp) at $T_{\pi^+} = 160$ MeV," *Physical Review*, **C41**, 2215–2228 (1990).

[21] S. Hyman et al. "^{16}O$(\pi^+, 2p)$ reaction at 165 MeV," *Physical Review*, **C41**, R409–413 (1990).

[22] J. Silk. "Signatures of initial- and final-state interactions in pion absorption," *Physical Review*, **C37**, 891 (1988).

[23] A. Stadler et al. "Faddeev Equations with Three-Nucleon Force in Momentum Space," *Physics Review*, **C44**, 2319–2327 (1991).

[24] M. Hirata, F. Lenz, and M. Thies. "Delta-nucleon and pion-nucleus interactions," *Physical Review*, **C28**, 785–810 (1983).

[25] E. J. Moniz. Pion-Nucleus Scattering in the Isobar Formalism. In *Theoretical Methods In Medium-Energy and Heavy-Ion Physics*, pages 603–666. Plenum Press, New York, 1978.

[26] Y. Wu, S. Ishikawa, and T. Sasakawa. "Three-Nucleon Bound States: Detailed Calculations of ^{3}H and ^{3}He," *Few Body Systems*, **15**, 145–188 (1994).

[27] K. Aniol et al. "Pion absorption on ^{3}He at $T_\pi = 62.5$ and 82.8 MeV," *Physical Review*, **C33**, 1714 (1986). An error has been found which lowers the cross sections reported in this publication. Reference *Phys. Rev.* **C43**, 957–972, (1991), reports the correct cross sections for this work in Tables II and III.

[28] S. Mukhopadhyay et al. "Pion absorption by ^{3}He at the Δ-resonance energy," *Physical Review*, **C43**, 957–972 (1991).

[29] P. Weber et al. "Two-Nucleon Absorption of π^+ and π^- on ^{3}He Across the Δ–Resonance Region," *Nuclear Physics*, **A501**, 765 (1989).

[30] P. Weber et al. "Three-Nucleon Processes and the Total Pion Absorption Cross Section in ^{3}He," *Nuclear Physics*, **A534**, 541 (1991).

[31] L. C. Smith et al. "Reaction ^{3}He(π^+, pp)p at $T_\pi = 350$ and 500 MeV," *Physical Review*, **C40**, 1347–1362 (1989).

[32] C. H. Q. Ingram. "Pion-Nucleus Interactions," *Nuclear Physics*, **A374**, 319c–357 (1982).

[33] H. J. Weyer. "Pion absorption in light nuclei," *Physics Reports*, **195**, 295 (1990).

[34] D. Ashery and J. Schiffer. "Pion Absorption in Nuclei," *Ann. Rev. Nucl. Part. Sci.*, **36**, 207–252 (1986).

[35] R. P. Redwine. "Pion-Induced Nuclear Reactions," *Invited talk presented at INS International Symposium on Nuclear Physics at Intermediate Energy, Tokyo, November 15-17* (1988).

[36] C. H. Q. Ingram. "Pion absorption in nuclei," *Nuclear Physics*, **A553**, 573c–584c (1993).

[37] T. Alteholz et al. "A Large Solid Angle Study of Pion Absorption in ^{3}He," *Physical Review Letters*, **73**, 1336–1339 (1994).

[38] Dornier Ltd., P.O. Box 1420, D-88039 Friedrichshafen, Germany.

[39] N. Gregory. Pion Single Charge Exchange on the Deuteron. Master's thesis, M.I.T. Figure taken from his thesis, which is in progress.

[40] Bicron Corporation, 12345 Kinsman Road, Newbury, Ohio 44065, USA.

[41] M. Wildi. *Untersuchungen zur π^+ Absorption im Fluge an ^{3}He mit dem "Large Acceptance Detector System" (LADS).* PhD thesis, Universitat Basel, 1993.

[42] Hamamatsu Corporation, 360 Foothill Road, P.O. Box 6910, Bridgewater, New Jersey 08807, USA.

[43] G. Backenstoss et al. "LADS – Large Acceptance Detector System for Pion-Nucleus Reactions," *Nuclear Instrumentation and Methods in Physics Research*, **A310**, 518 (1991).

[44] Dow Corning Corp., Box 0994, Midland, Michigan 48686, USA. The main component of the silicone epoxy was Silicone Elastomer 184.

[45] Paul Scherrer Institute, Villigen, Switzerland. *FDMT 100.* Available at the electronics shop.

[46] J. Bialkowski, W. Schoeps, and M. Kotsch. "Constant Fraction Discriminator with Automatic Adjustment of Optimal Triggering Level and Automatic Suppression of AC and DC Input Interference Signals," *Nuclear Instruments and Methods in Physics Research*, **228**, 110–117 (1984).

[47] J. Albanese et al. "The SIN High Resolution Pion Channel and Spectrometer," *Nuclear Intruments and Methods*, **158**, 363–370 (1979).

[48] Swiss Institute of Nuclear Science. *SIN Users Handbook*, 1981.

[49] R. Madey et al. "The Response of NE–228A, NE–228, NE–224 and NE–102 Scintillators to Protons from 2.43 to 19.55 MeV," *Nuclear Instrumentation and Methods*, **151**, 445–450 (1978).

[50] R. Cecil et al. "Improved Predictions of Neutron Detection Efficiency for Hydrocarbon Scintillators from 1 MeV to about 300 MeV," *Nuclear Instrumentation and Methods*, **161**, 439–447 (1979).

[51] A. Lehmann, A. Mateos, and R. Trezeciak. Private communication.

[52] TRIUMF Kinematics Handbook, 2nd edition, September 1987.

[53] D. C. Carey, K. L. Brown, and C. Iselin. DECAY TURTLE (Trace Unlimited Rays Through Lumped Elements) A Computer Program for Simulating Charged Particle Beam Transport. Technical Report SLAC-246 UC-28, Stanford Linear Accelerator, 1982.

[54] L'Air liquide (Firm). *Encyclopedie des Gaz*, pages 6–7, 799–800, 992 and 999. Elsevier, Amsterdam and New York, 1976.

[55] G. Backenstoss et al. "Evidence for a Direct Three-Nucleon Pion-Absorption Process," *Physical Review Letters*, **55**, 2782 (1985).

[56] P. Weber et al. "Multi-nucleon pion absorption in the ^{4}He($\pi^+, ppp)n$ reaction," *Physical Review*, **C43**, 1553 (1991).

[57] L.G.Greeniaus. LOSSPROG is available from TRIUMF. Help in locating it should be provided by GREE@erich.triumf.ca or system@erich.triumf.ca. A brief desciption is in TRIUMF Kinematics Handbook, 2nd Edition VII–19.

[58] C. Tschalär. "Straggling Distributions of Extremely Large Energy Losses," *Nuclear Intruments and Methods*, **64**, 237–243 (1968).

[59] F. James. "Monte Carlo Phase Space," *Cern Yellow Reports 68-15* (1968).

[60] S. Ishikawa and Y. Wu. Private communication.

[61] J. B. Walter and G. A. Rebka, Jr. *SCATPI - A Subroutine for Calculating* πN *Cross Sections and Polarizations for Incident Pion Kinetic Energies Between 90 and 300 MeV.* Technical Report LA-7731-MS, Los Alamos National Laboratory, 1979.

[62] E. Jans et al. "Quasifree $(e, e'p)$ Reaction on ^{3}He," *Physical Review Letters*, **49**, 974 (1982).

[63] C. Marchand et al. "High Proton Momenta and Nucleon-Nucleon Correlations in the Reaction ^{3}He$(e, e'p)$," *Physical Review Letters*, **60**, 1703–1706 (1988).

[64] A. M. Baldin et al. *Kinematika Jadrenih Reakcii.* Atomizdat, Moscow, 1968. In Russian.

[65] J. Werle. *Relativistic Theory of Reactions.* PWN-Polish Scientific Publishers, Warszawa, 1966.

[66] A. Mateos and N. Šimičević. Private communication. Manuscript in progress.

[67] C. Richard-Serre et al. "A Study of the Reaction $\pi^+ + \mathrm{d} \rightarrow \mathrm{p} + \mathrm{p}$ for Pion Energies Between 142 and 262 MeV," *Nuclear Physics*, **B20**, 413–440 (1970).

[68] B. Ritchie. "Reaction $\pi^+ + \mathrm{d} \rightarrow \mathrm{p} + \mathrm{p}$ at 65 to 140 MeV," *Physical Review*, **C27**, 1685–1692 (1983).

[69] J. Hoftiezer et al. "Energy Dependence of the $\mathrm{pp} \rightarrow \pi^+\mathrm{d}$ Differential Cross Section Between 500 and 600 MeV," *Physics Letters*, **100B**, 462 (1981).

[70] Y. Budagov et al. "Interaction Between 153-MeV Negative Pions and Helium," *Soviet Physics JETP*, **15**, 824 (1962).

[71] M. Baumgartner et al. "Inclusive π ^{4}He Scattering and the πN Interaction in the Nuclear Medium," *Nuclear Physics*, **A399**, 451–477 (1983).

[72] T.-S. H. Lee. Private communication.

[73] M. Betz and T.-S. H. Lee. "Phenomenological Hamiltonian for pions, nucleons, and Δ isobars: Apllications to the pion-deuteron system," *Physical Review*, **C23**, 375 (1981).

[74] R. Tacik et al. "Measurement of Three Protons in Coincidence Following Absorption of 228 MeV π^+ in Carbon," *Physical Review*, **C32**, 1335 (1985).

[75] H. Yokota et al. "Direct Observation of Multiple-Scattering Processes in Pion Absorption," *Physical Review Letters*, **58**, 191–194 (1987).

[76] L.L.Salcedo, E. Oset, and D. Strottman. "Experimental test of three-body pion absorption," *Physics Letters*, **B208**, 339 (1988).

[77] K. Gottfried and J. D. Jackson. "On the Connection between Production Mechanism and Decay of Resonances at High Energies," *Nuovo Cimento*, **33**, 3589 (1964).

[78] J. Zoll. *Lorentz Transformation.* CERN Computer Centre Program Library, U101.

[79] F. James. *Random Three-Dimensional Vectors.* CERN Computer Centre Program Library, V130.

[80] R. A. Arndt et al. "Pion-Nucleon Partial-Wave Analysis to 1100 MeV," *Physical Review*, **D32**, 1085 (1985).

4004-26